TECHNISCHE UNIVERSITÄT WIEN

GEO

Diplomarbeit

Monitoring of Alpine Snow Conditions Using C-Band SAR

zur Erlangung des akademischen Grades

Diplom-Ingenieur

im Rahmen des Studiums

066 421 Geodäsie und Geoinformation

eingereicht von

Claudio Navacchi
Matrikelnummer 01326246

ausgeführt am Department für Geodäsie und Geoinformation
der Fakultät für Mathematik und Geoinformation

Betreuung:
Betreuer: Univ.Prof. Dipl.-Ing. Dr.techn. Wolfgang Wagner
Mitwirkung: Univ.Ass. Dipl.-Ing. Dr.techn. Bernhard Bauer-Marschallinger

Wien, 14.12.2018

(Unterschrift Verfasser) (Unterschrift Betreuer)

Declaration

I declare that I have written this thesis under the auspices of the Department of Geodesy and Geoinformation by myself without any help or assistance of others. External literature, which was used to clarify the content, or provided data sources for research are clearly cited and attributed. This work has not been presented to any other testing authority before.

Date: 14.12.2018 Signature: _____

Abstract

The cryosphere is an essential part of the Earth's climate system, even more in the light of climate change actively impacting the extent of polar ice caps, glaciers and snow. Regions in interaction with these parts of the cryosphere must adapt to challenging conditions, as slight changes in temperature can have irreversible consequences. Informations about the state of a snow pack and ongoing processes within can be a valuable aid, e.g. for avalanche risk management, hydrological run-off models and tourism development.

This thesis focuses on revealing connections between various snow parameters, e.g. grain size, snow height or snow wetness, and high-resolution C-band SAR backscatter from ESA's Sentinel missions. Water has a very significant effect in the C-band for different states of aggregation (e.g., solid, liquid) offering a profound physical basis for investigating these relationships in alpine areas with a vast variety of snow conditions. For this case study, an alpine region covering parts of North and South Tyrol, was chosen. Data was acquired for a timespan of over two years, from summer 2015 to autumn 2017.

Well-known states of C-band backscatter like sigma naught, which can be related to backscatter from a unit area on ground, hinder a comparison with in-situ snow data due to the influence of different observation geometries. To overcome this, alternative representations of backscatter, like normalised backscatter, either being normalised by incidence angle or by performing a radiometric (terrain flattening) normalisation, are presented in this work. In the former case, linear regression and a novel approach, the piecewise linear percentile slope method, which takes the backscatter distribution of each orbit into account, were used. C-band backscatter was not only analysed as a single band, but also by including cross-polarisation ratios and change detection benefiting from a new method for an automatic, pixel-based reference image selection.

Overall, normalised backscatter by means of linear regression and VH polarisation appeared as the best setup, when correlating these data with in-situ snow measurements. Results were enhanced by spatial and temporal filtering of backscatter data leading to a partial increase in correlation by nearly 0.2. The most meaningful and consistent correlation of -0.64 was found with respect to maximum snow wetness, followed by air temperature (-0.59). Snow height was characterised by the highest correlation (0.67), but its significance is questionable. Concerning snow wetness, change detection performed best, when taking pixels at coldest conditions as reference values into account. Derived maps indicating wet and dry snow could offer useful information for run-off models and for determining fragile snow packs.

Zusammenfassung

Die Kryosphäre ist ein essenzieller Teil des Klimasystems der Erde und gewinnt an Bedeutung, da der Klimawandel die Existenz der Polkappen, Gletscher und einer anhaltenden Schneebedeckung bedroht. Regionen, welche sich mit der Kryosphäre in Interaktion befinden, müssen sich an die herausfordernden Gegebenheiten anpassen, da kleinste Änderungen der Temperatur unumkehrbare Folgen haben können. Informationen über den Zustand einer Schneedecke und die darin ablaufenden Prozesse können für Lawinenwarndienste, hydrologische Abflussmodelle und Tourismusentwicklung als Unterstützung dienen.

Diese Arbeit konzentriert sich darauf, Beziehungen zwischen Schneeparametern, wie z.B. Korngröße, Schneehöhe oder Schneenässe, mit einer hochaufgelösten C-Band SAR Rückstreuung von ESA's Sentinel Missionen zu untersuchen. Der signifikante Einfluss von Wasser in verschiedenen Aggregatzuständen (z.B. flüssig, fest) auf Rückstreuung im C-Band stellt eine fundierte, physikalische Grundlage für die Erforschung dieser Beziehungen dar. Alpine Gebiete ermöglichen eine solche Analyse aufgrund einer Vielzahl von Schneebedingungen . Im Rahmen dieser Arbeit erstreckt sich das ausgewählte Testgebiet hauptsächlich über die alpine Region Nord- und Südtirol. Die Zeitspanne der Datenverfügbarkeit beträgt zwei Jahre, vom Sommer 2015 bis zum Herbst 2017.

C-Band Rückstreuung bezogen auf Sigma Null, das sich auf die Rückstreuung von einer Einheitsfläche über Grund bezieht, erschwert den Vergleich mit In-situ Schneedaten, da es von Gelände- und Aufnahmevariationen beeinflusst wird. Um dieser Einschränkung entgegenzuwirken, kann auf andere Darstellungen der Rückstreuung übergegangen werden, z.B. normalisierte Rückstreuung, welche einerseits bezüglich des Einfallswinkels normalisiert werden kann, oder auch durch eine radiometrische Normalisierung durch Geländeeinebnung. Für den ersten Fall wurde lineare Regression und ein neuer Ansatz, die stückweise lineare Perzentil Methode, welche die Rückstreuungsverteilung eines jeden Orbits in Betracht zieht, verwendet. C-Band Rückstreuung wurde zudem nicht nur in Einzelaufnahmen analysiert, sondern auch als Kreuz-Polarisationsverhältnis und mithilfe von Veränderungsdetektion, die von einer neuartigen Methodik der automatisierten, pixelbasierten Referenzbildsuche profitiert.

Die höchsten Korrelationen mit Messungen von Schneeparametern konnten in Bezug auf die normalisierte Rückstreuung basierend auf linearer Regression und VH Polarisation gefunden werden. Zudem konnten unerwünschte Einflüsse in den Rückstreuungsdaten durch räumliche und zeitliche Filterung gedämpft werden, was zu einer um bis zu 0.2 verbesserten Korrelation führte. Die maximale Schneenässe zeichnete sich durch die fundierteste Korrelation (-0.64) aus, gefolgt von Lufttemperatur (-0.59). Schneehöhe

hatte die höchste Korrelation (0.67), welche aber aufgrund ihrer Signifikanz in Frage zu stellen ist. Die Veränderungsdetektion lieferte die besten Ergebnisse bezüglich nasser Schneekartierung, indem Rückstreuung bei den kältesten Bedingungen als Referenz in Betracht gezogen wurde. Abgeleitete Darstellungen, die auf nassen oder trockenen Schnee hinweisen, bieten hilfreiche Informationen für Abflussmodelle und für die Detektion brüchiger Schneedecken.

Acknowledgment

This work concludes my master studies at TU Wien, which have been pleasureful, but also challenging years. In addition to exciting insights in the subject of microwave remote sensing, which I have gained within the Remote Sensing research group at the Department of Geodesy and Geoinformation, I was able to broaden my scientific knowledge in terms of other fields of remote sensing during my studies abroad at University College London. I want to take this opportunity to express my gratitude to the people, who accompanied me on this path. My family always supported me in what I did, be it financially or having a friendly ear for my problems. Without their encouragement, I would not have come so far. I am also very happy, that new friendships evolved throughout the years. Thank you, Lukas Winiwarter, Jakob Thummerer and Manuel Schmitzer for very productive group works and most important, entertaining and amusing meetings off-campus. May this friendship continue beyond our college days! Moreover, I want to devote special thanks and my appreciation to my best friend, Bertram Tschiderer, who offers me a welcome change in my daily routine and shares my passion for climbing and metal. Raise your horns, brother!

I would like to thank Bernhard Bauer-Marschallinger for his supervision, Raphael Quast and Wolfgang Wagner for their scientific advice and finally the proofreaders of my thesis, Silke Scheiber, Philip Wack and Lukas Winiwarter.

Symbols

β	radar brightness
β^0	beta nought, backscatter from a unit area in slant range
σ^0	sigma nought, backscatter from a unit area on ground
γ^0	gamma nought, backscatter from a unit area on ground, but projected into a plane perpendicular to slant range
γ^0_{rtf}	radiometrically adjusted γ^0 by means of terrain flattening
θ	incidence angle, i.e. the projected local incidence angle
θ_{ref}	reference incidence angle for normalisation
σ^0_{norm}	normalised sigma nought
σ^{40}_{LR}	sigma nought normalised by means of linear regression at $\theta_{ref} = 40°$
σ^{40}_{PLPS}	sigma nought normalised with the piecewise linear percentile slope method at $\theta_{ref} = 40°$
κ_s	scattering coefficient
κ_e	extinction coefficient
ω	single scattering albedo
τ	optical depth
Θ	scattering angle
t	directional scattering parameter for the Henyey–Greenstein function
n_{BRDF}	normalisation factor of the BRDF
SD	snow height/depth
LA	number of layers
AT	air temperature
$\overline{GS}$	mean grain size
$\overline{SW}$	mean snow wetness
$\overline{SH}$	mean snow hardness
$\widehat{GS}$	maximum grain size
$\widehat{SW}$	maximum snow wetness
$\widehat{SH}$	maximum snow hardness

List of Figures

2.1 Interaction of radiation with a multi-layered snow pack. The first order intensity sums up as the direct backscattered intensity from the volume I_v and surface I_s, and the indirect backscattered intensity originating from surface-volume I_{sv} and volume-surface I_{vs} scattering. 16

3.1 Region of interest shown in an equirectangular grid (WGS 84). The Equi7 Grid at level T1 (100 km × 100 km) is shown on top. The tile *"E048N015T1"* used in this case study is highlighted in bold red. The text overlay illustrates the five meteorological weather stations within the tile (©Google Earth, Landsat/Copernicus). 24

3.2 Precipitation and maximum temperature data measured by the station *"Flughafen Innsbruck"* from July 1st, 2015 to October 1st, 2017 (data source: https://www.wetteronline.at). 26

3.3 Snowprofile "Ballunspitze" containing data, which was compiled at 11:50 LT on December 17th, 2015. The marked numbers refer to different sections of the snowprofile and are described in more detail in Section 3.2.2. 30

3.4 Locations of all snow profile measurements taken in the period July 2015 - September 2017, where each colour is related to a month. The extent is related to the tile *"E048N015T1"* in the Equi7 Grid system (basemap: ©Google Earth, Landsat/Copernicus). 32

3.5 Grain size related to snow temperature for a selection of grain types: depth hoar (red), rounded grains (blue), melt-freeze crust (yellow) and others (grey). 33

3.6 Snow wetness classes (1 (dry) to 5 (very wet)) compared to relative snow height (a) (0 stands for the bottom of the snow pack, 1 for the top) and to snow temperature (b). 34

3.7 Distribution of relative snow height (a) and snow temperature (b) shown for three different grain types: melt forms, decomposed snow and fresh snow. 34

3.8 Distribution of air temperature shown for three different grain types located at the top snow layer: melt forms, decomposed snow and fresh snow. . . . 35

3.9 Distribution of six classes related to snow hardness (cf. Subsec. 3.2.2) shown for three different grain types: melt forms, decomposed snow and fresh snow. 35

3.10 Relationship between snow hardness and snow density (blue dots) approximated with a linear model (black line). The distribution of snow densities for each snow hardness value is delineated by a boxplot. 36

4.1 Overview map to show the picked points representing each land cover type, rocky areas (black dots) and alpine meadows (green dots). The meteorological measurement station *"Obergurgl"* is marked as a red dot (basemap: Orthofoto Tirol WMS, accessed on Oct. 19th, 2018, URL: https://gis.tirol.gv.at/arcgis/services/Service_Public/orthofoto/MapServer/WMSServer?request= GetCapabilities&service=WMS). 39
4.2 Mean backscatter for rocky areas and alpine meadows in comparison to measured precipitation data at station *"Obergurgl"*. 40
4.3 Simulated backscatter σ^0 for observed snow profile data at $\theta = 40°$ compared to four different snow parameters: snow density (a), snow height (b), snow temperature (c) and grain size (d). The RGB colour refers to the fraction of the scattered intensity from the surface I_{surf} (red), volume I_{vol} (green) and interaction I_{int} (blue) to the total intensity. Since surface scattering is clearly dominating and for visualisation purposes, I_{vol} and I_{int} were scaled by a factor of two. 42

5.1 Normalisation areas related to the different backscatter representations β^0, σ^0 and γ^0. θ is the incidence angle, A_β the reference area in slant range, A_σ the reference area on ground and A_γ the reference area perpendicular to the looking direction. The extents of these areas are defined by means of the range resolution δ_r, azimuth resolution δ_a, ground range resolution δ_g and projected ground range resolution δ_p (Redrawn from Small (2011), from Fig. 2). 44
5.2 Overview of the necessary steps needed for normalising backscatter with the PLPS method. Measurements are shown in yellow, blue and red (relative S-1 orbit numbers 15, 117 and 168). For each orbit, the 5$^{\text{th}}$, 10$^{\text{th}}$, 25$^{\text{th}}$, 50$^{\text{th}}$, 75$^{\text{th}}$, 90$^{\text{th}}$ and 95$^{\text{th}}$ percentile (✚) are computed and connected to form a line covering the whole range of incidence angles. The slope of the 50$^{\text{th}}$ percentile defines extrapolated lines, which are depicted as dashed lines. Vertical cuts intersect the lines at the reference incidence angle and at the measurement (•) to retrieve representative backscatter values to normalise backscatter in a final step. 47
5.3 Sketch of the IDW method to interpolate precipitation data at a location of interest (yellow dot). Data from five stations (*"Zugspitze"* (S_1), *"Flughafen Innsbruck"* (S_2), *"Patscherkofel"* (S_3), *"Reschenpass"* (S_4) and *"Idalpe"* (S_5)) are taken into account. Two precipitation time series are compared, one acquired at station *"Reschenpass"* and one interpolated by using all data. 49

5.4 Comparison of σ^0_{norm} for two backscatter normalisation methods, LR (a) and PLPS (b). All parameters are estimated for the whole time series of σ^0 for one pixel (x=4803458 m, y=1587908 m in Equi7 Grid coordinates). . 51
5.5 Comparison of σ^0 to both normalised backscatter representations, σ^{40}_{PLPS} and σ^{40}_{LR} (VV polarisation). The depicted time series refers to one pixel and ranges from October 15th, 2015 to September 30th, 2015 (x=4803458 m, y=1587908 m in Equi7 Grid coordinates). 52
5.6 Comparison of σ^0, γ^0_{rtf}, σ^{40}_{LR} and σ^{40}_{PLPS} in VV polarisation over mountainous terrain for an acquisition on June 27th, 2017. γ^0_{rtf} masks areas characterised by radar shadow, whereas σ^{40}_{LR} and σ^{40}_{PLPS} exclude pixels with an unfavourable orbit distribution. The spatial extent of the depicted region is shown in (a). The red outer box represents the boundaries of the Equi7 tile *"E048N015T1"* and the red inner box depicts the extent shown in the figures above. 53
5.7 Comparison of all residuals after difference formation σ^{40}_{LR}, σ^{40}_{PLPS} and γ^0_{rtf} with each other. The depicted residuals result after shifting the distribution with respect to the mean. The images in VV polarisation show an acquisition on May 27th, 2016 for a subregion marked in (a). 55
5.8 Comparison of the interpolated weather data for all three different synthetic reference image selection methods (relative S-1 orbit number 117). Coordinates are given in the Equi7 Grid system. 58

6.1 Pearson's correlation coefficient $r_{Pearson}$ resulting from relating backscatter data to snow parameter data. Visual guidance is given through a colourisation of $r_{Pearson}$, where negative correlation is coloured as red and positive as blue. 60
6.2 $r_{Pearson}$ in dependency on the neighbourhood (in pixel units) taken into account for averaging. Different curves are plotted for a subset of snow parameters. 63
6.3 Correlations of cross-polarised backscatter data and various snow parameters expressed as $r_{Pearson}$ (three neighbours included). 64
6.4 Correlation matrices containing $r_{Pearson}$ for each backscattering difference and snow parameter combination, except (a), which focuses on backscattering coefficients. All $r_{Pearson}$ are based on three neighbours. For each method, only the best result fulfilling the specific criteria was taken as a synthetic reference image. 66
6.5 Backscattering differences for $\tilde{\sigma}^0_{VH}$, different reference images and filtering methods covering the region around the *"Zugspitze"*. All $\tilde{\sigma}^0_{VH}$ values above zero are masked. The spatial extent of the depicted region is shown in (a). The red outer box represents the boundaries of the Equi7 tile *"E048N015T1"* and the red inner box depicts the extent shown in the figures above. 68

6.6 Time series for all backscattering coefficients at VH polarisation (top), cross-polarisation ratios (center) and backscattering differences at VH polarisation by using the "coldest" synthetic reference image (bottom) (including three neighbours). Following the same order, AT, SD together with $\overline{GS}$, and $\widehat{SW}$ are plotted in relation to the backscatter curves. 70
6.7 Comparison of $\tilde{\gamma}^0_{rtf,VH}$ with a Landsat 8 OLI false colour image[1]. The RGB composite consists of the SWIR-band (R), NIR-band (G) and Red-band (B). The spatial extent of the depicted region is shown in (a). The red outer box represents the boundaries of the Equi7 tile *"E048N015T1"* and the red inner box depicts the extent shown in the figures above. 71
6.8 Comparison of $\tilde{\sigma}^0_{VH}$ and $\sigma^{40}_{LR,CR}$ with Landsat 8 OLI false colour images[2]. The RGB composite consists of the SWIR-band (R), NIR-band (G) and Red-band (B). The area covers glaciers and the highest peaks in the chosen region of interest (e.g. *"Wildspitze"*). The spatial extent of the depicted region is shown in (a). The red outer box represents the boundaries of the Equi7 tile *"E048N015T1"* and the red inner box depicts the extent shown in the figures above. 73

B.1 Distribution of σ^0 and σ^0_{norm} for a pixel located at a glacier (*"Rettenbachferner"*). Strong snowmelt is clearly visible as low backscatter values, i.e. the 5th and 10th percentile. 87
B.2 Unfavourable conditions for normalising backscatter at a pixel located in the *"Inntal"* valley: only two orbits are available and they are very close to each other. 87
C.1 Relation between the height a.s.l. of the stations and their measured temperature values on December 15$^{\text{th}}$, 2016 (red), April 1$^{\text{st}}$, 2017 (green) and August 15$^{\text{th}}$, 2016 (blue). 87
D.1 Comparison of σ^0 and γ^0_{rtf} backscatter curves fitted to backscatter measurements at selected locations belonging to rocky areas. In each plot, measurements from two different dates, June 6th, 2017 and May 24th, 2017, are set into relation. 88

List of Tables

3.1 *Corine Land Cover* types within the area of the Equi7 tile *"E048N015T1"*. 23

5.1 Maximum temperature statistics (in °C) from July 1st, 2015 to September 30th, 2017 56

5.2 Precipitation statistics (in mm) from July 1st, 2015 to September 30th, 2017 56

Contents

1 Introduction **10**
- 1.1 Motivation . . . 10
- 1.2 Aim . . . 11
- 1.3 Outline . . . 11

2 State of the Art **13**
- 2.1 C-Band SAR . . . 13
  - 2.1.1 History . . . 13
  - 2.1.2 Sentinel-1 . . . 14
  - 2.1.3 Concepts and Characteristics . . . 14
- 2.2 Theoretical Models . . . 15
  - 2.2.1 Conventional RT (CRT) . . . 16
  - 2.2.2 Dense Media RT (DMRT) . . . 17
- 2.3 Snow Parameter Retrieval . . . 18
- 2.4 Backscatter Normalisation . . . 20

3 Region of Interest and Data Sets **22**
- 3.1 Region of Interest . . . 22
  - 3.1.1 Study Area . . . 22
  - 3.1.2 Weather Conditions . . . 23
- 3.2 Data Set Descriptions . . . 26
  - 3.2.1 Sentinel-1 Data and Pre-Processing . . . 26
  - 3.2.2 Snow Profile Data . . . 28
  - 3.2.3 Meteorological Data . . . 31
- 3.3 Snow Parameter Analysis . . . 31

4 Sensitivity Analysis **37**
- 4.1 Methodology . . . 37
  - 4.1.1 Theoretical Model . . . 37
  - 4.1.2 Semi-empirical Model . . . 38
- 4.2 Estimated Backscatter Sensitivity to Dry Snow Parameters . . . 41

5 C-Band SAR Method Advancements **43**
5.1 Methodology . . . 43
5.1.1 Radiometric Terrain Flattening . . . 43
5.1.2 Piecewise Linear Percentile Slope (PLPS) . . . 45
5.1.3 Synthetic Reference Image Selection for Change Detection . . . 48
5.2 Method Benchmarking . . . 50
5.2.1 Backscatter Representation . . . 50
5.2.2 Feasibility of Reference Image Synthesis . . . 56

6 Results and Discussion **59**
6.1 Correlations of C-Band SAR Backscatter and Snow Parameters . . . 59
6.2 Impact of Spatial Behaviour on C-Band Backscatter and Snow Parameter Correlations . . . 63
6.3 Correlations between Cross-Polarisation Ratios and Snow Parameters . . . 64
6.4 Correlations between Backscatter Changes and Snow Parameters . . . 65
6.5 Snow Parameter and C-Band SAR Backscatter Time Series Comparison . . . 69
6.6 Comparison to Optical Imagery . . . 71

7 Summary and Conclusion **74**

8 Outlook **77**

Bibliography **79**

Appendices **84**
A DMRT Parameters . . . 84
B PLPS Examples . . . 86
C Temperature Interpolation . . . 87
D C-Band SAR Backscatter Sensitivity to Wet Snow . . . 88

Chapter 1

Introduction

1.1 Motivation

Aperture synthesis in radar imaging has allowed the acquisition of high-resolution earth observation data. This data is commonly referred to as synthetic aperture radar (SAR) imagery (Moreira et al., 2013). Due to its high sensitivity to water, C-band SAR is an indispensable way of monitoring land and water surfaces from space. This enables a broad range of applications, such as monitoring soil moisture (e.g., Bauer-Marschallinger, Freeman, et al., 2018), crop fields (e.g., Nicolas Baghdadi et al., 2017), floodings (e.g., Twele et al., 2016), marine oil slicks (e.g., Najoui et al., 2018), sea-ice (e.g., Moen et al., 2015) and, being the focus of this thesis, snow mapping (e.g., Nagler, Rott, et al., 2016). Recent satellite missions were funded in cooperation of the European Commission (EC) and the European Space Agency (ESA), contractually residing within the Copernicus programme. Within the framework of this Earth observation programme, the radar mission Sentinel-1 was initiated to provide high-resolution C-band SAR data along with an unprecedented temporal repeatability.

Accordingly, these satellite data offer a suitable basis for monitoring snow parameters with a high temporal variability, as it is the case for water movements inside a snow pack (Singh et al., 1997) or grain variations dependent on the type of snow metamorphism (Sommerfeld and LaChapelle, 1970). Meteorological measurement stations, which observe air temperature, surface temperature and precipitation (rain- and snowfall) do not suffice to fully describe ongoing processes and states of the snow pack. Therefore, it is necessary to consider a more precise description of a snow pack, e.g. by means of snow profile measurements. Due to the efforts of various avalanche warning services, e.g. *Lawinenwarndienst Tirol (LAWIS Tirol)*, historic snow profile data is available for the recent past and data acquisition will continue in future. Surveyors measure relevant snow parameters, such as snow wetness, grain size, snow temperature and snow hardness, primarily with a focus on avalanche risk studies. This data is also extremely valuable when

set into relation with C-band SAR backscatter data. To the knowledge of the author, no recent studies have taken place to compare field measurements with C-band SAR data, which should offer additional and valuable insights due to a higher spatial resolution compared to older studies (e.g., Nagler and Rott, 2000; Longepe et al., 2009). Quantifying these insights in terms of mathematical and physical relations, extensive snow parameters derived from C-band SAR should enable the possibility to support run-off models, avalanche warning services and climate change studies.

1.2 Aim

Past studies have shown that it is possible to map snow parameters with C-band SAR, but either under certain limitations or with the aid of other SAR data, e.g. other frequency bands or fully polarised SAR data. These studies emphasised defining semi-empirical models to derive a certain snow parameter, be it snow wetness (Shi and Dozier, 1995) or grain size (Shi and Dozier, 2000b). However, Sentinel-1 SAR data is clearly limited in terms of applying such models, as Sentinel-1 only operates at C-band and fully-polarised data is commonly not available. Therefore, this study relies on a data-based approach, without focusing specifically on a physical model. Light should be shed on relations between snow parameters, which are represented by the measured snow profile data of *LAWIS Tirol*, and C-band backscatter data given by Sentinel-1A/B. Results should then indicate, which relations are worth to be investigated further concerning snow parameter retrieval. In summary, the key research question that this thesis seeks to address, is the following: Is there an interdependency between certain snow parameters and C-band SAR backscatter? If so, how can these insights be applied or be helpful for monitoring alpine snow conditions?

1.3 Outline

This thesis starts with a brief revision of relevant literature to present the current state of the art in this research area and the aforementioned topics, i.e. C-band SAR backscatter and satellite missions (Sec. 2.1), theoretical models to describe backscatter from snow (Sec. 2.2), existing snow parameter retrieval algorithms (Sec. 2.3) and backscatter normalisation methods (Sec. 2.4). The region of interest and data characteristics are described in Chapter 3 for both backscatter and snow profile measurements. Backscattering behaviour in terms of different snow parameters is exploited on a semi-empirical basis via a sensitivity analysis in Chapter 4. Then, C-band SAR backscatter method advancements are introduced in Chapter 5 reducing the incidence angle dependency of backscatter with the assistance of a novel backscatter normalisation method or by radiometric terrain flattening as proposed in Small (2011). Additionally, an improved, profound reference image selection process, given its fundamental importance for change detection,

is suggested. The outcome of all backscatter enhancement methods is brought together, related to snow profile data and discussed in Chapter 6. Finally, Chapter 7 summarises and concludes the results of this work, followed by an outlook to draw attention to future research questions (Ch. 8).

Chapter 2

State of the Art

Understanding the theory of C-band SAR interactions with a snow pack is essential and shall therefore be reviewed in this chapter. Relevant literature should clarify the current status of research regarding this relationship, beginning with an explanation of C-band SAR (Sec. 2.1), subsequently introducing theoretical models (Sec. 2.2) as well as snow parameter retrieval (Sec. 2.3) and finally presenting different methods to normalise backscatter (Sec. 2.4).

2.1 C-Band SAR

2.1.1 History

Further to the groundbreaking achievements by Carl A. Wiley (Wiley, 1985), the inventor of the Synthetic Aperture Radar (SAR), the age of spaceborne SAR missions began with the launch of the first operational L-band SAR satellite, Seasat, in 1978. C-band spaceborne SAR was initiated by the first remote sensing satellites from ESA, the European Remote Sensing Satellites (ERS-1 and ERS-2, 30 m spatial resolution) launched in 1991 and 1995, respectively. Both exceeded their operational lifetime by many years, supplying users with valuable information about changes at land and sea. The orbit constellation made it possible to monitor terrain variations through interferometric SAR (InSAR). ENVISAT/ASAR (2002-2012) was another milestone in the history of C-band SAR with a novel antenna technology allowing a flexible steering of the beam. Other long-lasting and very successful C-band SAR satellite missions were RADARSAT-1 and RADARSAT-2, with the latter one still ongoing (Moreira et al., 2013). Within the frame of the Copernicus programme (European Commission, 2017), essential services have been defined (e.g., atmosphere and land monitoring). This has led to the design of the Sentinel satellite missions using both optical and radar instruments. Focusing on C-band SAR radars, Sentinel-1A and Sentinel-1B launched in April 2014 and April 2016 and circuit the Earth in a near-polar, sun-synchronous orbit (ESA, 2018). In near future, a

RADARSAT follow-on mission, the RADARSAT Constellation Mission (RCM), is scheduled to lift-off in 2019 with the aim of successfully continuing the history of C-band SAR (Canadian Space Agency, 2018).

2.1.2 Sentinel-1

Since the launch of both Sentinel-1 satellites, a vast amount of data (1 TB/day) has been collected offering a significant potential for maritime security, sea-ice mapping, flood mapping, applications concerning forestry, agriculture and water management, land-surface monitoring (i.e. surface motion) and research. The C-band antennas of the Sentinel-1 satellites operate at 5.405 GHz and offer dual polarmetric SAR (VV, VH, HV, HH), which is of great relevance for agricultural purposes. Both twin satellites are 180° apart from each other in their orbital plane resulting in a revisit time of six days at the equator and one to three days in mid-latitudes (e.g. European Alps). Different imaging modes (Stripmap (SM), Interferometric Wide swath (IW), Extra-Wide swath (EW) and Wave mode (WV)) are available and allow the aquisition of data with a spatial resolution up to 5 m × 5 m (SM mode). Swath widths can range from 80 km (SM mode) to 400 km (EW mode) (European Space Agency, 2018).

The IW mode is the most common used mode over land surfaces and utilises the Terrain Observation with Progressive Scans SAR (TOPSAR) technique (De Zan and Guarnieri, 2006). Here, the swath is split into three sub-swaths and the beam is steered in range and azimuth (backward to forward) to achieve a homogeneous image quality (uniform Signal-to-Noise ratio) at an expense of a lower spatial resolution in azimuthal direction. In a next step, SAR data is detected, multi-looked and projected to ground range (GRD). However, in contrast to a single look complex image (SLC), no phase information is available in the GRD data. GRD data is available in full (FR), medium (MR) and high resolution (HR). The spatial resolution of a GRD product is dependent on the chosen mode leading to a pixel spacing of 10 m when operating in IW mode.

2.1.3 Concepts and Characteristics

The C-band is a part of the electromagnetic spectrum (∼4 GHz to 8 GHz) used for WiFi devices, satellite communication systems and weather radar systems (ITU, 2018). Due to its day, night and all-weather applicability, it is also a favourable frequency range in Earth observation. Electromagnetic waves in the optical domain do not penetrate clouds and are therefore restricted in areas with frequent cloud cover, like mountainous regions. In addition, C-band is most sensitive to water, because it covers the maximum dielectric loss within the relaxation spectrum of water, i.e. the resonance frequency of the H_20 molecule. Advantageously, dry snow and ice behave inversely, with ice having a very low complex part of the dielectric constant ($< 10^{-3}$) at C-band (Wagner and Quast, 2015). Thus the high dielectrical contrast between dry and wet snow underlines the possibility

of mapping wet snow with C-band SAR.

The concept of SAR is based on a side looking acquisition of a coherent radar mounted on air- or spaceborne platforms. Amplitude and phase information from continuously transmitted and received coherent pulses are stored and evaluated by means of the Doppler shift, which is also known as the Doppler beam sharpening method. In other words, the phase information of an object enables to construct a so called synthetic aperture, which is equal to the path length travelled by the satellite while the object was observed. This makes it possible to overcome drawbacks of a side looking radar regarding the resolution in azimuth, which is influenced by the orbit height and antenna length. Using SAR facilitates an azimuth resolution half of the antenna length, independent of the distance to the sensed object. For a more detailed description and an excellent tutorial on SAR, the interested reader is referred to Moreira et al. (2013).

2.2 Theoretical Models

The fundamental theory behind all models describing the interaction of electromagnetic (EM) waves with media is based on the radiative transfer equation (RTE). It states, that radiation passing a medium can lose energy due to absorption and scattering (both together forming the extinction part of the equation) or can gain energy due to emission. The broad applicability of this theory covers scientific disciplines such as atmospheric science (e.g., Smith, 1970), astrophyics (e.g., Rybicki and Lightman, 2008) and remote sensing (e.g., Quast and Wagner, 2016). Remote sensing uses RTE in a twofold way, namely either for the passive case with a focus in brightness temperature (Picard, Brucker, et al., 2012), or for the active case concentrating on backscatter (Picard, Sandells, and Löwe, 2018). Since Sentinel-1 gathers data through an active measurement principle, the latter form of the RTE in conjunction with other theories (e.g. Quasi-crystalline approximation with coherent potential (QCA-CP)) will be presented here.

An exemplary drawing of an EM wave impinging on a multi-layered snow pack is given in Fig. 5.2. Scattering occurs at the air-snow interface, which is commonly neglected during modelling (small term for dry snow), within the snow pack and at the snow-ground interface.

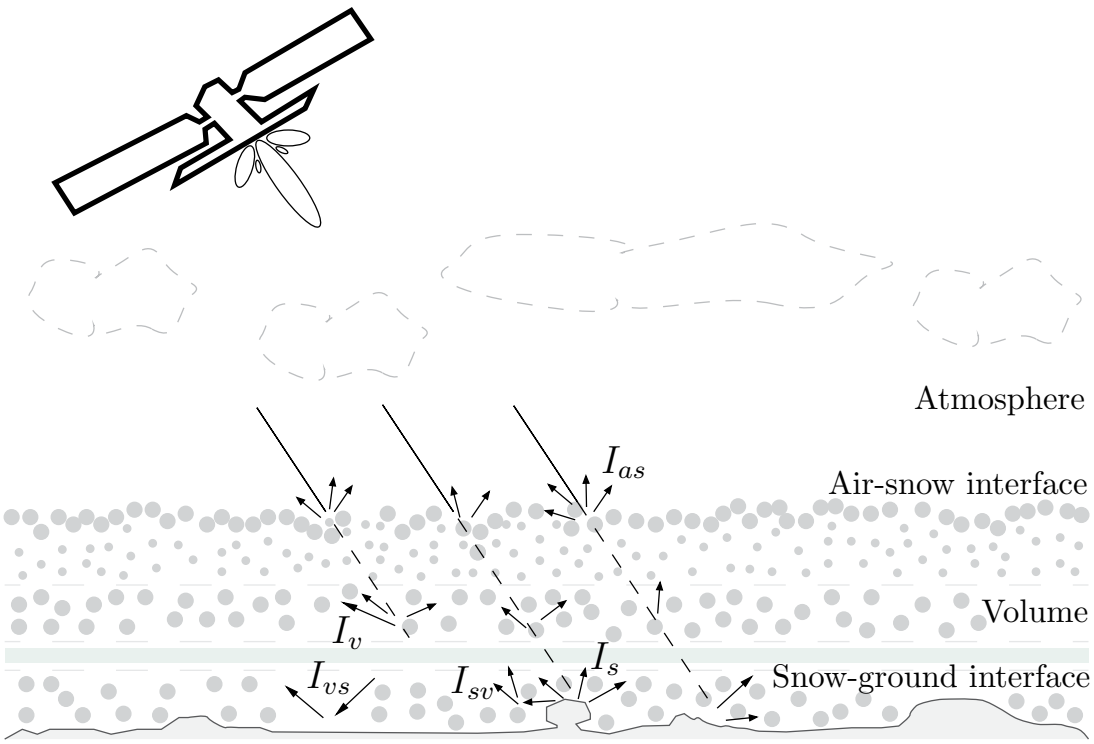

Figure 2.1: Interaction of radiation with a multi-layered snow pack. The first order intensity sums up as the direct backscattered intensity from the volume I_v and surface I_s, and the indirect backscattered intensity originating from surface-volume I_{sv} and volume-surface I_{vs} scattering.

2.2.1 Conventional RT (CRT)

The conventional radiative transfer equation reads as below (cf., Quast and Wagner, 2016; Shih et al., 1997):

$$\cos(\theta)\frac{\partial \overline{I}(z,\phi,\theta)}{\partial z} = -\kappa_e \overline{I}(z,\phi,\theta) + \kappa_e\,\omega \int_0^{2\pi} \mathrm{d}\phi' \int_0^{\pi} \mathrm{d}\theta' \sin(\theta') P(\phi',\theta',\phi,\theta)\,\overline{I}(z,\phi',\theta') \tag{2.1}$$

In general, Eq. 2.1 is formulated as a matrix equation, where $\overline{I}$ is the 4×1 stokes vector fully describing the polarimetric properties of the specific intensity and P the phase matrix, which defines the relation of the incident (azimuth angle ϕ' and zenith angle θ') and scattered radiation (ϕ and θ). For small particles (relative to the sensor wavelength), P is given by the Rayleigh Phase matrix. ω is the single-scattering albedo and is the ratio between the scattering coefficient κ_s and extinction coefficient κ_e. Consequently, ω states how much loss of energy is due to scattering and and how much due to absorption ($\omega \in [0, 1]$).

To solve the differential-integral Eq. 2.1 for $\overline{I}$ by approximation, numerical methods are applied. In Shih et al. (1997), Eq. 2.1 is transformed into a system of first-order differential equations and is then solved using an eigenanalysis. Some approaches, also known as Matrix Doubling methods, go further and reformulate the problem as a superposition of infinite layers, each characterised by an infinitesimal optical depth $\Delta\tau$, albedo ω and a single scatter phase matrix P (cf. Fung and Eom, 1981). An analytical solution of Eq. 2.1 does not exist, but Quast and Wagner (2016) present a first-order approximation by neglecting higher terms of a series expansion in κ_s. This is only valid under the assumption of a weakly scattering medium ($\kappa_s \ll 1$).

2.2.2 Dense Media RT (DMRT)

In case of a dense medium, where multiple scattering and a higher dielectric contrast between the dense and the background medium is present, one has to find a different formulation of radiative transfer parameters. Tsang, Ding, and Wen (1992) define these parameters for a dense medium consisting of particles with different sizes and permittivities. Under these circumstances, coherent scattering has to be taken into account, which is commonly described by the Quasi-crystalline approximation with coherent potential (QCA-CP) model. It is a conjunction of scattering equations linked through a coherent potential and states that it is more suitable to describe the background medium using an effective propagation constant K as the amount of particles increases. The relationship between different particles can be represented by a pair-distribution function, which defines the interaction capability. An analytical solution of the pair distribution function is given by the sticky particles model underlining the tendency that particles form clusters and bonds, thus acting as one scattering object (Tsang, Kong, et al., 2004).

The DMRT equation resembles the CRT equation very much and only discerns in terms ω and κ_s. In DMRT it is also assumed that grains are small, thus the application of the Rayleigh Phase matrix is legitimate (cf. Tsang and Kong, 2004). Moreover, the way of retrieving the backscattered intensities is also very similar, but often multiple layers with different properties are introduced. This snow pack stratification complicates a model inversion, since a coupled set of DMRT equations (one for each layer) linked via boundary conditions has to be solved (Shih et al., 1997). As for CRT theory, matrix doubling is a favourable way of resolving these equations as confirmed by Du, Shi, and Rott (2010). They show a remarkable difference of backscatter at VV and VH polarisation for both particle shapes and snow stratification, whereas the latter one is due to multiple scattering. In recent work, Picard, Sandells, and Löwe (2018) have summarised different variants of the DMRT theory and have undertaken a model benchmarking.

2.3 Snow Parameter Retrieval

Naturally, theoretical model simulations can agree with measurements in certain cases, but commonly both mismatch, since measurements vary with the spatial resolution of the sensor and are often prone to random and systematic errors, or theoretical models are not able to fully describe the ongoing processes. Additionally, very complex theoretical models would need representative and extensive data for all input parameters to be able to invert the model. Assumptions, parameter fixing (always use the same value for a parameter, e.g. the same surface type for a region), parameter aggregation (one parameter represents others) often help to overcome the problem of measured parameter availability and invertibility of the model. These issues and approaches also apply to snow parameter retrieval and mapping. Many studies set up semi-empirical models with the assistance of theoretical insights. In the following, methods for retrieving various kinds of snow parameters with a primary focus on C-band SAR are shown.

Shi and Dozier (2000a) and Shi and Dozier (2000b) presented a semi-empirical modelling strategy to estimate snow density (and ground properties) with SIR-C's L-band sensor and snow depth and particle size with SIR-C's X/C-band sensor. The former makes use of the relation between backscatter in VV and HH polarisation, since it is strongly governed by dielectric and roughness properties of the surface. Changes in incidence angles and wavelength shifts are related to dielectric properties of the snow pack, which therefore enable a retrieval of snow density. In their companion work (Shi and Dozier, 2000b), this methodology helps to fix unknown parameters (e.g. surface roughness and snow density). The therein introduced first-order, polarimetric model aims to describe the co-polarised, total backscatter as a sum of a air-volume, volume, volume-ground and ground backscattering term. Most terms were simulated by varying ground and snow properties and subsequently replaced by semi-empirical formulae, where the coefficients were found by a multivariate regression analysis. This physically-based model builds upon many simplifications and is surely affected by a significant error propagation, but seems to perform well for the measurement configuration of SIR-C.

Snow water equivalence (SWE) can be inferred from snow density and snow depth. A very simple approach to estimate SWE uses a linear model with airborne C-band SAR data from EMISAR as input, but is still dependent on ground-truth data (Arslan et al., 1999). Similarly, Bernier and Fortin (1998) show that SWE is linearly correlated with thermal resistance, which reflects the sensitivity of soil temperature to changes of the air temperature and is solely dependent on the snow density and snow depth via an empirical formula. However, the retrieval is limited to a shallow snow pack covering frozen soil in a flat area. Very recent studies exploit the possibilities of mapping SWE with C-band SAR data from Sentinel-1, based on the cross-polarisation ratio, i.e. the ratio between VH and VV polarised backscatter (De Lannoy et al., 2018).

How to derive snow wetness as a quantitative parameter, namely as snow liquid water content, with C-band SAR at VV and HH polarisation is explained in Shi, Dozier, and Rott (1993) and Shi and Dozier (1995). A simplified physical model describes the total backscatter returned by a wet snow covered area as a sum of volume backscattering and surface backscattering at the air-snow interface.

Further methods use the advantageous absorption properties of water at C-band frequencies and focus on change detection rather than explicitly estimating liquid water content. The foundation for this approach was laid by Nagler and Rott (2000) followed by their recent work (Nagler, Rott, et al., 2016). To do so, a reference image has to be selected first. Different approaches were followed in past publications: choosing a dry, snow-free backscatter image, a backscatter image sensed at very cold, freezing conditions, or an average of multiple reference images to reduce speckle (Nagler and Rott, 2000; Nagler, Rott, et al., 2016; Bernier and Fortin, 1998). The former two aim to extract wet snow, whereas the latter one focuses on describing a dry snow pack in terms of the SWE. In the next step regarding wet snow mapping, an image preferably sensed during a snowmelt period is then directly related to the selected reference image. Applying a threshold on the difference between both results in a wet snow map. The original idea of applying one threshold (e.g. -2 dB in Nagler and Rott, 2000 or -3 dB in Longepe et al., 2009), was enhanced by Magagi and Bernier (2003), defining a threshold per incidence angle range. The advantage of relying on a relative comparison is that surface scattering and effects due to terrain variations mainly cancel out. Surface scattering is assumed to be approximately constant, because the land cover buried under a snow pack is likely to have a steady behaviour (except run-off from snowmelt), i.e. no vegetation is involved. More advanced change detection algorithms to map wet snow were developed by Koskinen, Pulliainen, and Hallikainen (1997) and Nagler, Rott, et al. (2016). The former investigate forested areas covered by wet snow in terms of different tree types and two reference images (before and after the snowmelt season), whereas Nagler, Rott, et al. (2016) suggest a combination of VV and VH polarisation to increase the reliability of wet snow mapping.

2.4 Backscatter Normalisation

Backscatter normalisation is about the elimination of the dependency of backscatter on incidence angles. In literature, various approaches for this have been presented. For instance, one can apply Lambert's law of optics,

$$\sigma^0_{norm} = \sigma^0 \frac{1}{\cos^\beta(\theta)} \tag{2.2}$$

where σ^0 is the measurement at a given incidence angle θ, σ^0_{norm} the normalised backscatter (per unit area) and β the order of the cosine. However, this assumes that the backscatter distribution follows the cosine law and that the illuminated area can be characterised as a Lambertian surface (Lievens et al., 2011). For normalising σ^0 with respect to a given reference angle θ_{ref} one can use

$$\sigma^0_{norm} = \sigma^0 \frac{\cos^\beta(\theta_{ref})}{\cos^\beta(\theta)} \tag{2.3}$$

One can easily see that Eq. 2.3 is equal to Eq. 2.2 for $\theta_{ref} = 0\,^\circ$. For both, β has to be adjusted according to the polarisation and landcover type in different studies, including agricultural monitoring (Shimada, 2005), wetlands mapping (Baghdadi et al., 2001) and being very relevant for this thesis, snow mapping (Shi, Dozier, and Rott, 1994).

Diverse remote sensing satellite systems collecting multiangle data made it possible to apply data-driven normalisation techniques. Some of those techniques rely on a high temporal resolution (i.e. having enough data) or a special measurement configuration. A simplified, linear relation between θ and σ^0 serves as a basic assumption to normalise the backscatter via a known slope and intercept parameter. Scatterometers, such as ERS-SCAT or A-SCAT, allow for a direct (i.e. in one overpass) computation of these parameters, since the same area is measured three times in a for-, mid and aftbeam (Naeimi, Scipal, et al., 2009). For other sensors like ASAR on ENVISAT, data is used to estimate the slope and intercept based on a linear regression (LR). The slope parameter offers interesting insights on vegetation, land cover (Sabel et al., 2010) and changes with the phenological cycle (Wagner, Lemoine, et al., 1999). Regarding Sentinel-1, it is more difficult to estimate the slope due to a shorter time of operation and a smaller range of incidence angles covered by the measurements resulting from the chosen orbital configuration. Recent attempts were taken in the direction of resampling Sentinel-1 data to 500 m and to estimate the slope parameter through a multivariate linear regression model by taking the sensitivity of backscatter, which is expressed by the ratio of the 95^{th} and 5^{th} percentile, and mean backscatter into account (Bauer-Marschallinger, Freeman, et al., 2018). However, high-resolution backscatter normalisation (e.g. for Sentinel-1) is still an open research topic.

Beside backscatter normalisation with respect to θ, radiometric normalisation is also essential to ensure comparability. This can either be a calibration of the measured signal (e.g. using calibration constants) or a more complex procedure like radiometric terrain flattening. The latter one mainly aims to radiometrically adjust layover-affected areas, which is shown in Small (2011) and Frey et al. (2013), and will be discussed in more detail in Section 5.1.1.

Chapter 3

Region of Interest and Data Sets

All data have been gathered for a region in the Austrian Alps, which is described in more detail in Section 3.1. The following sections provide an overview for the used C-band SAR satellite data (Subsec. 3.2.1), snow profile data (Subsec. 3.2.2) and meteorological data (Subsec. 3.2.3). In addition the relationship of various snow parameters are analysed too (Sec. 3.3).

3.1 Region of Interest

Instead of broadening the geographic scope, it was found to be more feasible to consider two winter seasons instead of one. Based on the availability of snow profile and satellite data, the chosen time span ranges from July 2015 to September 2017. This time span could offer an interesting comparison of both winters, due to the fact that Sentinel-1B delivers data from September 2016 onwards and could demonstrate if the additional data adds valuable information. The same region of interest as in previous works (e.g. Nagler, Rott, et al., 2016; Nagler and Rott, 2000; Navacchi, 2016) was chosen for this thesis, which is justified in Section 3.1.1. To reveal trends and support any analysis later on, a brief overview of past weather conditions will be given in Section 3.1.2.

3.1.1 Study Area

The chosen region covers the western part of North Tyrol and a small northern part of South Tyrol and relates to the tile *"E048N015T1"* of the Equi7 Grid system (Bauer-Marschallinger, Sabel, and Wagner, 2014). It includes mountain massives such as the *"Lechtaler Alpen"*, *"Pitztaler Alpen"*, *"Ötztaler Alpen"*, *"Karwendel"* and *"Silvretta"*. The highest peak is the *"Wildspitze"* (3768 m a.s.l.), in the *"Ötztaler Alpen"*. Coniferous species are the main tree type governing the forests of this region. In contrast to mountainous and forested terrain, agricultural and pastoral areas and small villages seam most of the valleys. Industry is mainly located around the regional capital city of North Tyrol,

Innsbruck. The permanent settlement region is about 12% of the area covered by North Tyrol, being the lowest of all nine Austrian provinces (Wikipedia, 2018). According to the *Corine Land Cover* map[1], the distribution of the most important land cover types is set out in Table 3.1.

Table 3.1: *Corine Land Cover* types within the area of the Equi7 tile *"E048N015T1"*.

Type	**Percentage** [%]
Coniferous forest	30
Natural grasslands	18
Bare rocks	13
Sparsely vegetated areas	13
Moors and heathland	6
Pastures	6
Mixed forest	4
Glaciers and perpetual snow	2
Discontinuous urban fabric	2
Complex cultivation patterns	1
Fruit trees and berry plantations	1

As one can imagine from the above description, the whole area is highly attractive for winter and summer tourism. Tourism is a very important economic driver for the region, demanding investments and necessary maintenance of ski slopes, hiking trails and tourist accommodation, impacting on the natural landscape. Information about the state of snow packs can therefore be very useful to assist the former task. Given the land cover diversity in the table above, this region seems to be perfectly suitable for investigating the outlined relationship in Section 1.2.

3.1.2 Weather Conditions

At the beginning of the chosen time span in July and August 2015, a maximum in temperatures was reached with respect to climatologic history. This hot weather period was interrupted in mid-September by colder temperatures, intense precipitation and snowfall at 1000 m a.s.l. November and December 2015 exhibit high temperatures and precipitation of 50-100% below average. In higher altitudes, temperature was 7 °C above the mean and even the risk of forest fires was present.

[1] see https://land.copernicus.eu/pan-european/corine-land-cover

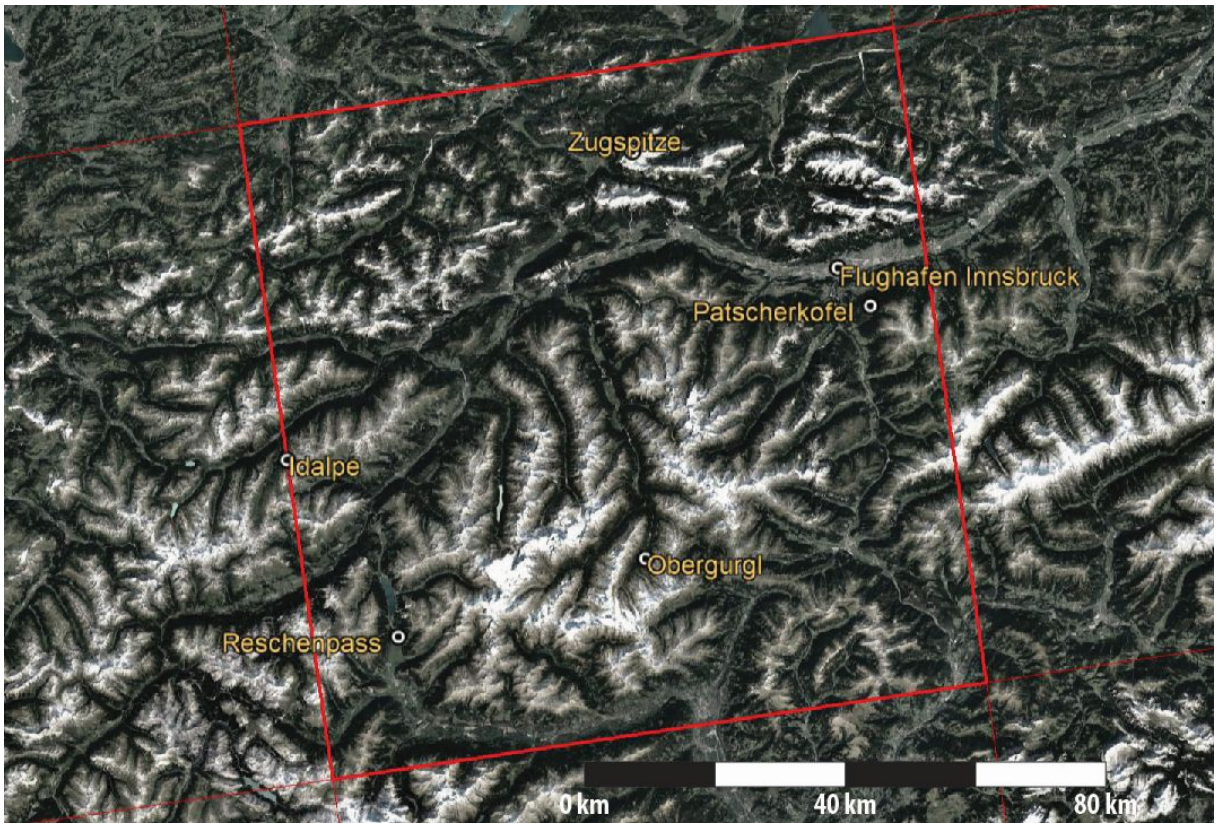

Figure 3.1: Region of interest shown in an equirectangular grid (WGS 84). The Equi7 Grid at level T1 (100 km × 100 km) is shown on top. The tile *"E048N015T1"* used in this case study is highlighted in bold red. The text overlay illustrates the five meteorological weather stations within the tile (©Google Earth, Landsat/Copernicus).

2016 started as 2015 had finished, but with a lot of snow on mountains due to more precipitation. Regions at lower elevations suffered still from the absence of a longer lasting snow pack. At the end of April 2016, cold temperatures and snowfall led to a second onset of winter creating issues in agricultural areas. A very wet and rainy May was followed by one of the hottest June in history, with a peak temperature of 35 °C in Innsbruck and 70% more precipitation than usual. Heavy rainfall and thunderstorms led to mudslides and flooded areas in July and August 2016. Less precipitation and cloudy weather characterised the subsequent months and a few colder days enforced snowfall in lower elevated regions. In November and December 2016 temperatures were above the mean and less snowfall prevented a longer lasting snow pack below $1000 - 1400$ m a.s.l.

2017 began with one of the coldest months, having temperatures of 3 °C below the average in mountainous regions above 1500 m a.s.l. The lowest temperature (−30 °C) was measured at the *"Pitztaler Gletscher"* (3440 m a.s.l.). In general, snow heights increased due to the accumulation of fresh snow being 25-50% above usual levels in January. Sunny conditions and a 4 °C higher temperature than the yearly mean marked the hottest March since the beginning of recordings. Despite an increase in precipitation, fresh snowfall was about 50% lower than usual. April 2017 brought cold weather with snowfall in the mountains at the end of the month. From June onwards, temperatures increased rapidly (3 °C above the mean) with hot and humid conditions in July and August 2017. Finally, September 2017 concludes the chosen time span with rainy, cloudy and cold weather, which led to snowfall above 1400 m a.s.l.

A visual overview of past weather conditions represented by the measured meteorological data of station *"Flughafen Innsbruck"* is given in Figure 3.2 showing some of the weather extremes mentioned above. Weather summary information was retrieved from the climate monitoring tool of *ZAMG*[2].

[2]see https://www.zamg.ac.at/cms/de/klima/klima-aktuell/klimamonitoring

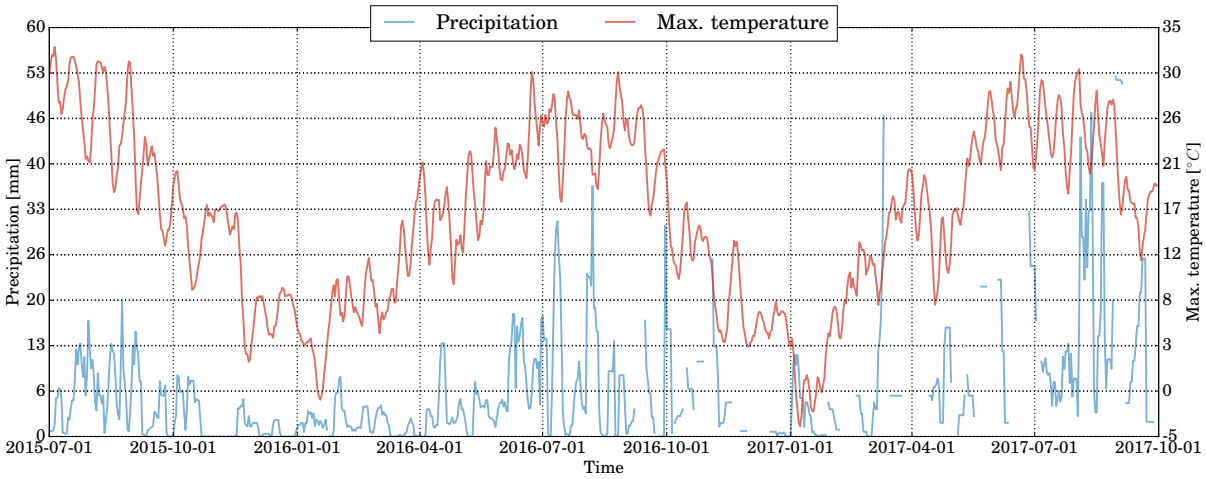

Figure 3.2: Precipitation and maximum temperature data measured by the station *"Flughafen Innsbruck"* from July 1st, 2015 to October 1st, 2017 (data source: https://www.wetteronline.at).

3.2 Data Set Descriptions

3.2.1 Sentinel-1 Data and Pre-Processing

The satellite data used in this thesis is Level-1 IW GRDH raw data from Sentinel-1A/B and is hosted by the *Earth Observation Data Centre for Water Resources Monitoring (EODC)*[3], which receives Sentinel-1, Sentinel-2 and Sentinel-3 data from ESA's data hubs. This data on the *EODC* storage is linked to the *Vienna Scientific Cluster 3 (VSC-3)*[4], a supercomputer capable of processing in parallel significant amounts of Earth observation data. The *SAR Geophysical Retrieval Toolbox (SGRT)* (Naeimi, Elefante, et al., 2016), which internally makes use of the *Sentinel Application Platform (SNAP)*[5], served as a primary tool for preprocessing the Level-1 IW GRDH raw data on the *VSC-3*. As a result, the following products were available:

- **Sigma naught σ^0:** All data concerning this type of backscatter representation were processed considering the following steps:

  1. If available, an update of the orbit state vectors in the metadata (only approximate orbit state vectors are included in the raw files) using precise orbit data was done (`Apply-Orbit-File`[6]).

[3] see https://www.eodc.eu
[4] see http://vsc.ac.at/systems/vsc-3
[5] see http://step.esa.int/main/toolboxes/snap
[6] terms written in this style are related to commands of the *Graphical Processing Tool (GPT)* of *SNAP*

2. Low backscatter from shallow or flat surfaces (e.g. lakes, rivers or streets) is often affected by a certain amount of additive noise. This is due to movements of electrons being dependent on temperature, also known as "Thermal Noise" (Park et al., 2018, p. 1556), which has been corrected for (`ThermalNoiseRemoval`).
3. Radiometric Calibration of digital pixel values (`Calibration`).
4. To reduce speckle, multi-looking was performed (`Multilooking`).
5. Geometric terrain correction and orthorectification based on the SRTM v.4.1[7] digital elevation model (DEM) (90 m spatial resolution) had been the final SAR processing step before all outputs were resampled to the Equi7 Grid.

However, this processing chain could not fully account for all errors in the data. Some σ^0_{VH} images had to be deleted, because of remaining scalloping artefacts, which could arise from an inaccurate doppler centroid mean frequency estimation (Elizavetin, 2018). This resulted in 705 σ^0_{VV} and 670 σ^0_{VH} images.

- **Projected local incidence angle θ:** θ images are auxiliary products and are used implicitly in the processing chain described above (e.g. backscatter coefficient transformations). θ is the local incidence angle (LIA), which is the angle between the surface normal and the incidence radiation, projected into the range plane (PLIA).
- **Terrain flattened gamma naught γ^0_{rtf}:** The processing chainline to produce γ^0_{rtf} differs from σ^0 in terms of an additionally radiometric terrain flattening step before geometric terrain correction is performed. After quality checks, the number of valid γ^0_{rtf} images resulted in 699 $\gamma^0_{rtf,VV}$ and 670 $\gamma^0_{rtf,VH}$ images, respectively.

A brief description about different backscatter representations and radiometric terrain flattening will be given in Section 5.1.1.

[7] data source used by *SNAP*: http://srtm.csi.cgiar.org/SELECTION/inputCoord.asp

3.2.2 Snow Profile Data

To be able to expand the research related to interactions of C-band SAR with snow, detailed data about the structure of a snow pack is indispensable. *LAWIS Tirol*[8] offers such data. Using a crowdsourcing approach, qualified users can measure certain snow properties and enter the data through a web interface into a database. However, due to data access restrictions, snow profiles were only available in *PNG* or *PDF* format. Therefore, every snow profile had to be digitised semi-automatically.

First, all data provided by a snow profile is explained. The following enumeration refers to Figure 3.3 and conveys the possibilities of working with these data.

1. The name/title of the snow profile
2. Information about the person who collected the data (*"Name"*, *"E-Mail"*) and the measurement timestamp (*"Aufnahmedatum"*)
3. The following fields constitute the sub-header of a snow profile: the location (*"Ort"*), subregion (*"Subregion"*), region (*"Region"*), country (*"Land"*), geographical coordinates (*"Lat./Long."*), elevation a.s.l. (*"Seehöhe"*), incline (*"Hangneigung"*), aspect (*"Exposition"*), wind speed (*"Windgeschw."*), wind direction (*"Windrichtung"*), air temperature (*"Lufttemperatur"*), precipitation (*"Niederschlag"*, i.e. snow, rain, ...), precipitation intensity (*"Intensität"*, i.e. weak, moderate, strong), sky condition (*"Bewölkung"*, i.e. cloudiness index from 0 to 8) and snow profile class (*"Schneeprofilklasse"*). These metadata fields provide detailed information about the surroundings of a snow profile and other properties
4. In this section of a snow profile, all symbols related to the grain structure of a snow layer are defined (e.g. fresh snow (*"Neuschnee"*), decomposed/fragmented grains (*"Filziger Schnee"*), rounded grains (*"Rundkörnig"*), ...). Approximately, 10-11 grain types have been defined by *LAWIS Tirol*
5. Two dials assisting the visual interpretation of (10), (14), (15) and (16) are shown in this part. The upper one represents air and snow temperature ranging from $-22\,^{\circ}\mathrm{C}$ to $0\,^{\circ}\mathrm{C}$ and the lower one snow hardness ranging from 0 to 1000 Newton (or above related to ice)
6. Snow height in cm
7. Snow wetness ranging from 1 (dry) to 5 (very wet)
8. First and second order grain type according to (4)
9. Grain size in mm

[8] see https://lawine.tirol.gv.at

10. Snow hardness ranging from 1 (fist, very soft) to 6 (ice, compacted)
11. Rivets represent the borderline condition. The more rivets, the more disadvantageous is the assessment of this layer
12. Stability tests offer information about the sliding conditions of a layer due to external pressure (skies, shovels, ...)
13. Additional notes
14. Air temperature
15. Visualisation of snow hardness in Newton (cf. (5))
16. Snow temperatures in °C (cf. (5))

Parameters/parts only being of interest for specific avalanche services or derived from others were neglected for further analysis: (11), (12), (13) and (15). For any additional information, the reader is redirected to the documentation of the snow profile web tool (LAWIS Tirol, 2016).

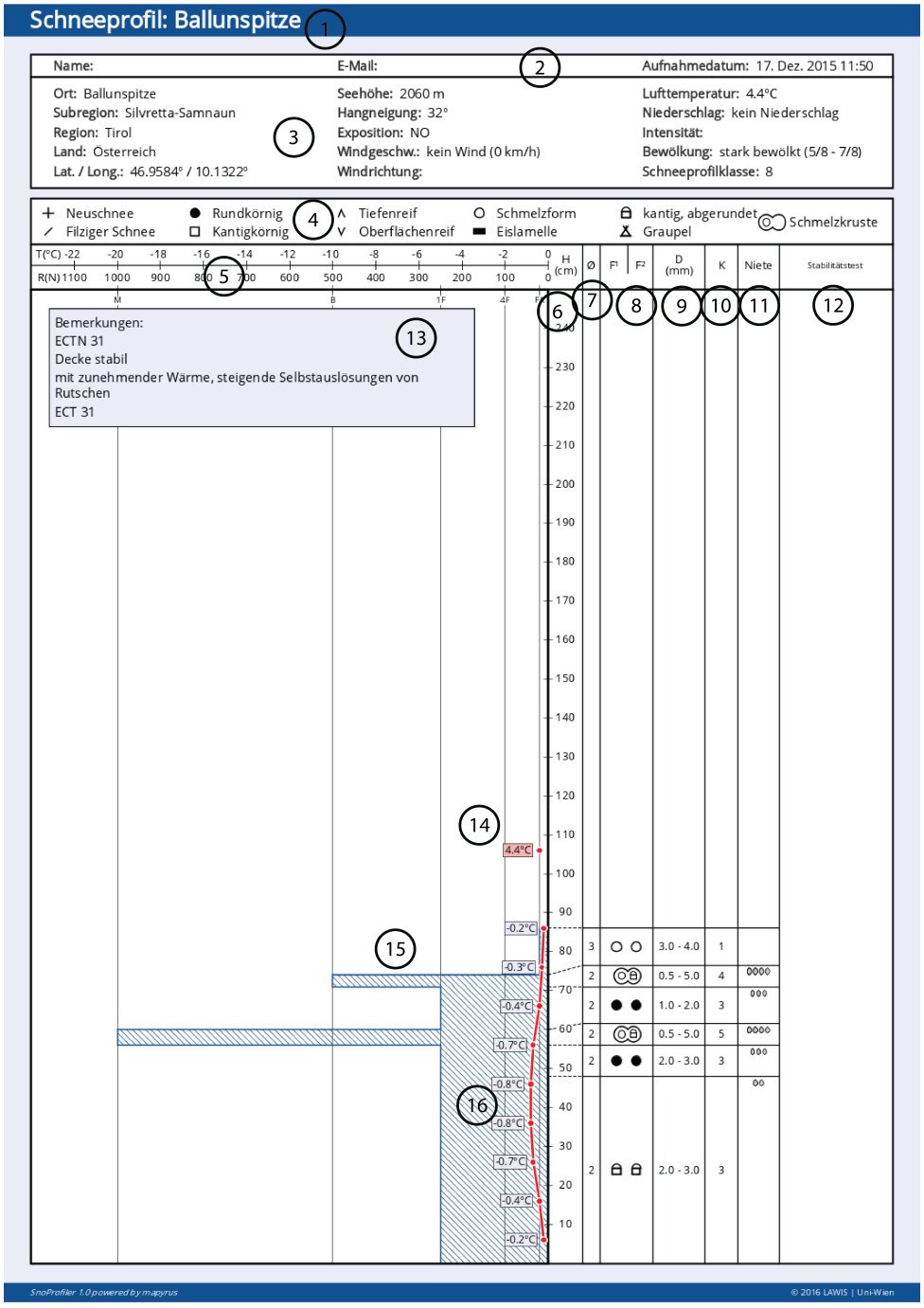

Figure 3.3: Snowprofile "Ballunspitze" containing data, which was compiled at 11:50 LT on December 17th, 2015. The marked numbers refer to different sections of the snowprofile and are described in more detail in Section 3.2.2.

3.2.3 Meteorological Data

Meteorological data (i.e. precipitation and maximum temperature) was needed to select an appropriate reference image (cf. Sec. 5.1.3) for change detection and to assist interpretations concerning the above mentioned data sets. Therefore, *WetterOnline*[9], a service distributing historic weather data of stations (*"Idalpe"*, *"Flughafen Innsbruck"*, *"Zugspitze"*, *"Patscherkofel"*, *"Obergurgl"* and *"Reschenpass"*), which are intersected by the region of interest, was found to provide suitable auxiliary data. Data availability from station *"Obergurgl"* is limited as there is no data for summer 2017. All stations are depicted in Figure 3.1.

3.3 Snow Parameter Analysis

This section focuses on analysing the different aspects of the snow profile data. First, an overview of the measurement locations is given in Figure 3.4. In total, 312 snow profiles are within the region of interest. It can be seen that most measurements were taken in winter and spring, also having a broad spatial distribution. Snow profiles registered in winter form clusters at places that can be easily reached, such as ski slopes and glaciers used for skiing (e.g. *"Pitztaler Gletscher"* and *"Obergurgl"*).

Next, relationships between various snow parameters and patterns in the data are being investigated. This analysis is accompanied by relevant literature to support interpretations and to see if gained insights agree with theory. One has to be careful when interpreting correlations, since spatial autocorrelations are evident (e.g. fewer measurements at higher elevations). Fig. 3.5 initiates this analysis with a comparison of grain size to snow temperature. Each data point is further colourised by the classified grain type, in this case the following three have been chosen: melt-freeze crust (*"Schmelzkruste"*), rounded grains (*"Rundkörnig"*) and depth hoar (*"Tiefenreif"*). It can be seen that an increase in snow temperature has a positive correlation with grain size. Furthermore, all grain types cover a broad range of snow temperatures, which is not thought to be primarily an issue of measurement accuracy, rather a subject to snow metamorphism. In this process, water vapour diffusion is caused by a present temperature gradient. Different types of snow metamorphism play an important role in bond formation and grain enlargement, e.g. firnification, equi-temperature or melt-freeze metamorphism. According to Fig. 3.5, the largest grains can be found, when depth hoar is present. This is a sign of an ongoing temperature-gradient metamorphism within an aged snow pack, resulting in large depth hoar crystals (Sommerfeld and LaChapelle, 1970; Giddings and LaChapelle, 1962). Other comparisons, such as relating the grain size at the top layer of the snow pack with air temperature, did not show any correlation.

[9] see https://www.wetteronline.at

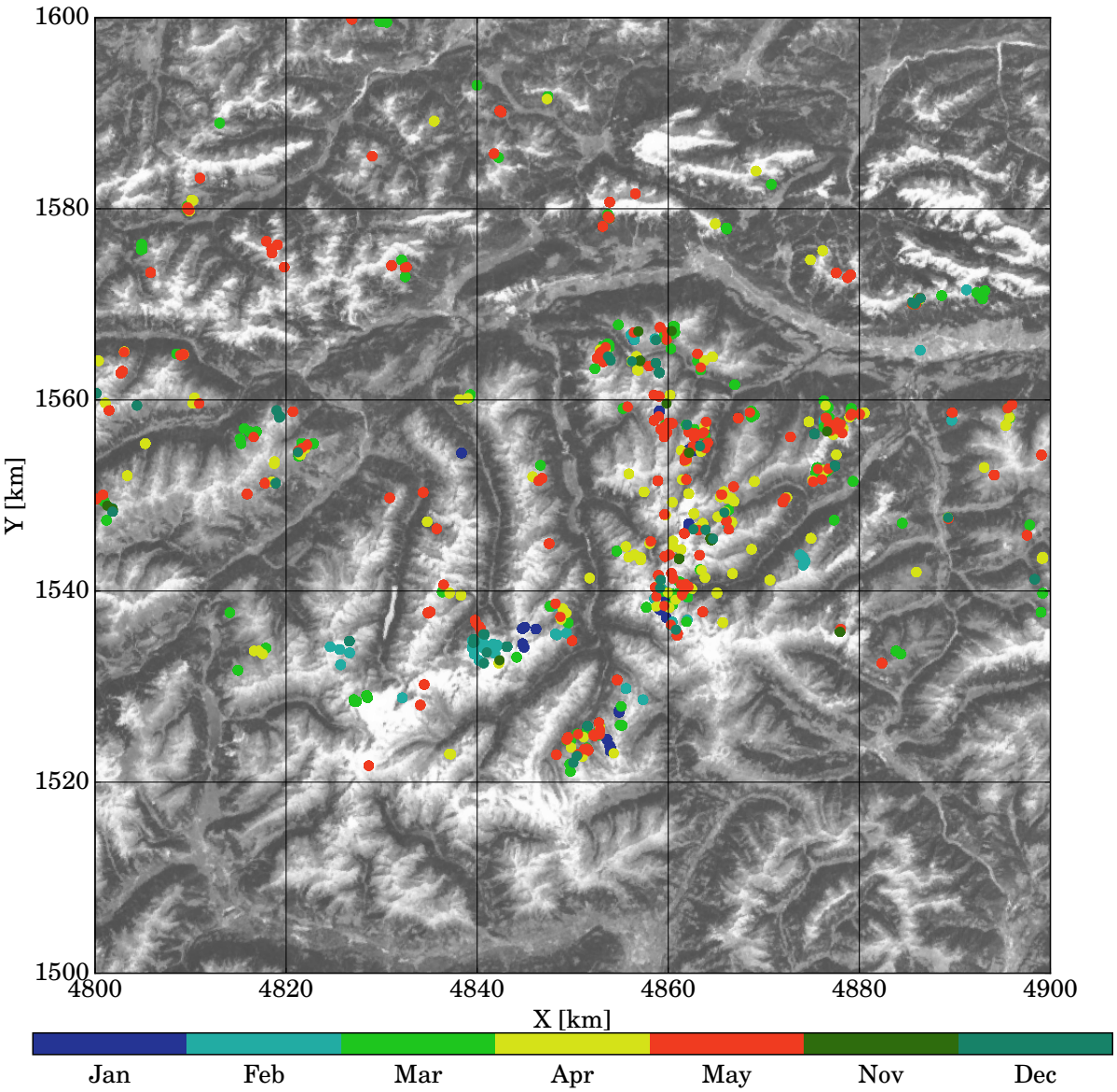

Figure 3.4: Locations of all snow profile measurements taken in the period July 2015 - September 2017, where each colour is related to a month. The extent is related to the tile *"E048N015T1"* in the Equi7 Grid system (basemap: ©Google Earth, Landsat/Copernicus).

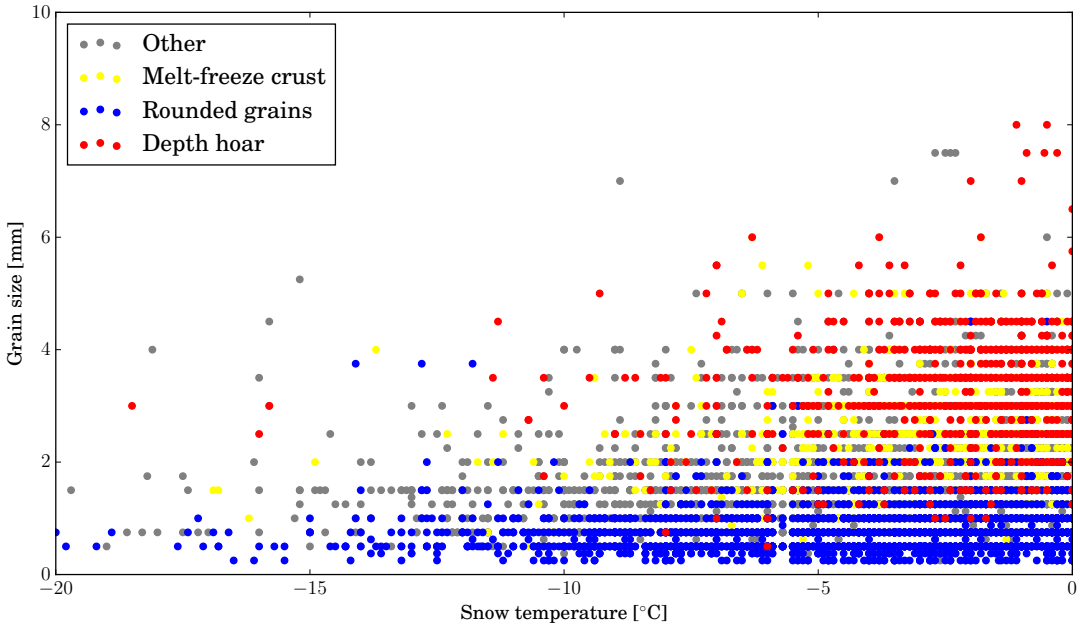

Figure 3.5: Grain size related to snow temperature for a selection of grain types: depth hoar (red), rounded grains (blue), melt-freeze crust (yellow) and others (grey).

C-band SAR backscatter is very sensitive to the next snow parameter being investigated, namely snow wetness. Field measurements only contain a discrete and subjective classification of snow wetness as mentioned in Section 3.2.2. Figure 3.6 depicts the driest, moistest and wettest condition of the snow pack in relation with the relative snow height (a) and snow temperature (b). One can see, that in Fig. 3.6 (a) dry snow (class 1) can be mainly found in the middle and upper part, moist snow (class 3) is dominant in the upper and lower part and very wet snow (class 5) has a higher probability of being in the upper part. The wetness in the upper part could be caused by rainfall or solar radiation (Jamieson, 2006). Yet, very wet snow only occurred 12 times in the data, whereas dry snow occurred 12,000 times, diminishing the reliability of class 5. Figure 3.6 (b) nicely shows that class 5 is only present at snow temperatures of around 0 °C, class 3 covers a broader range of temperatures, but also being centered at 0 °C and class 1 has a left-skewed distribution centered at ~ -1 °C.

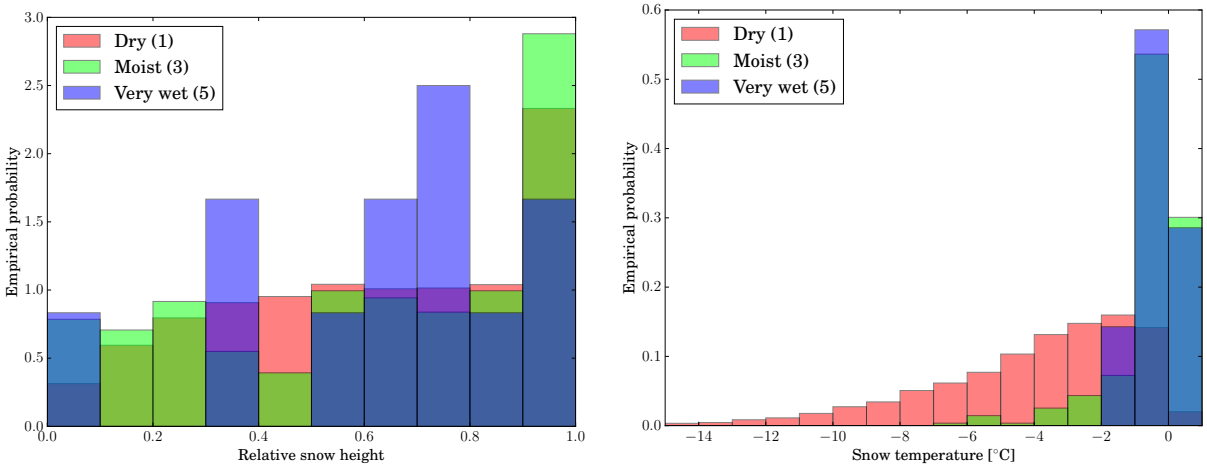

(a) (b)

Figure 3.6: Snow wetness classes (1 (dry) to 5 (very wet)) compared to relative snow height (a) (0 stands for the bottom of the snow pack, 1 for the top) and to snow temperature (b).

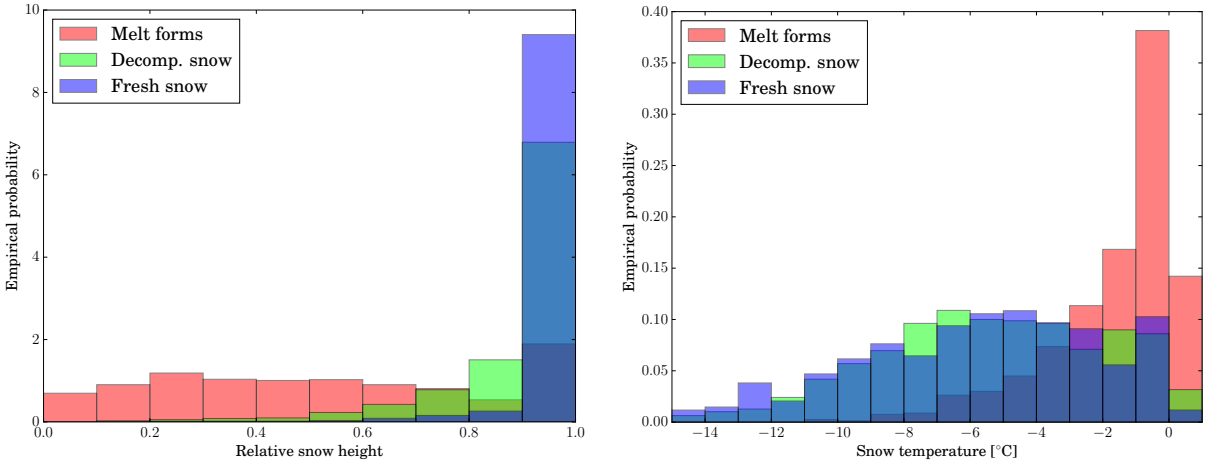

(a) (b)

Figure 3.7: Distribution of relative snow height (a) and snow temperature (b) shown for three different grain types: melt forms, decomposed snow and fresh snow.

Figure 3.7 (a) confirms that fresh snow is mainly located at the top of the snow pack, similar to decomposed snow also, with the latter having a larger deviation and reaching down to the middle part of the snow pack. Melt forms are present in the lower part, being buried under other snow types. These melt-freeze crusts or melt forms beneath layers of less dense snow increase the likelihood of avalanches (Jamieson, 2006). One can identify a strong relation between warmer snow temperatures and melt forms in Figure 3.7 (b), implying that this grain type mainly occurs around $-1\,°C/0\,°C$. Fresh and decomposed

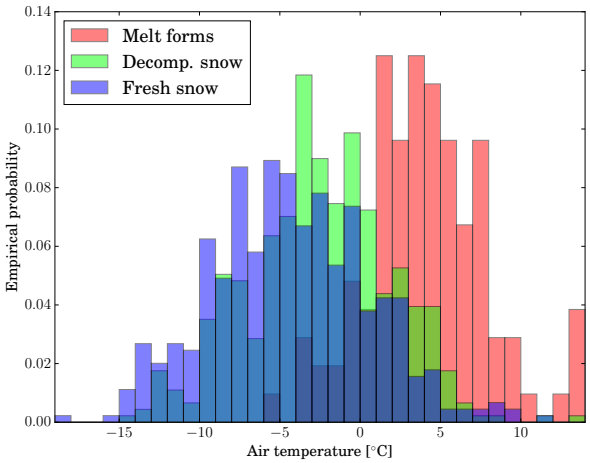

Figure 3.8: Distribution of air temperature shown for three different grain types located at the top snow layer: melt forms, decomposed snow and fresh snow.

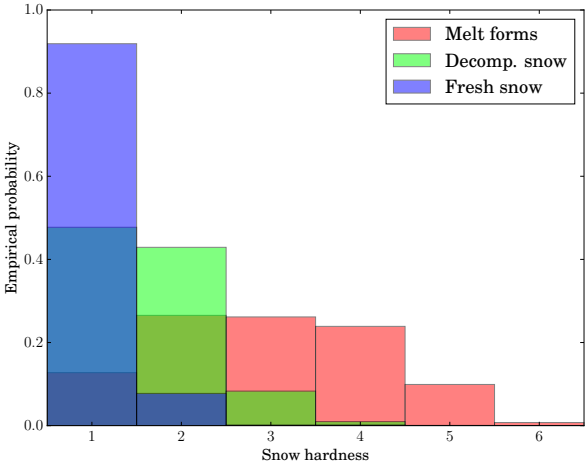

Figure 3.9: Distribution of six classes related to snow hardness (cf. Subsec. 3.2.2) shown for three different grain types: melt forms, decomposed snow and fresh snow.

snow overlap and can't be distinguished well, which could be explained by previous melt and freeze cycles causing snow to decompose.

Distributions of grain types at the top snow layer are more distinctive in Figure 3.8 than in Figure 3.7 (b), which includes all layers of the snow pack. Comparing both histograms in terms of their kurtosis, it can be concluded that temperature gradients are mainly influencing the structure of the grain. Another noteworthy parameter to investigate is snow hardness. The vertical distribution turns out to be very similar to Figure 3.7 and is strongly related to the grain type, which is shown in Figure 3.9. Fresh snow is very fluffy, thus easy to penetrate, followed by decomposed snow. Melt forms compose a harder medium, but are still characterised by a larger deviation and cover nearly all hardness categories.

Some of the parameters analysed before have the major disadvantage of not being objectively measured but instead being related to a subjective scala dependent on the surveyor. This drawback relates in particular to snow hardness and snow wetness. The former implies to be related to snow density, not only by its name, but also by the way its measured. Different objects, such as a fist, fingers, a pencil or a knife, are used to exert a force on the snow layer and to test its penetrability (LAWIS Tirol, 2016). Some additional notes (cf. (13) in Subsec. 3.2.2) contain valuable information about snow density measurements at different snow depths, which enables to correlate snow hardness and snow density. Figure 3.10 shows a linear relation between the two. A vague trend of larger uncertainties or larger deviations with respect to the fitted line is present at lower snow hardness values. This could imply, that snow hardness measurement methods like a fist or fingers are more dependent on the surveyor than for instance a pencil or a knife. Additionally, it could be the case, that the former are not suitable to relate lower snow hardness with snow density.

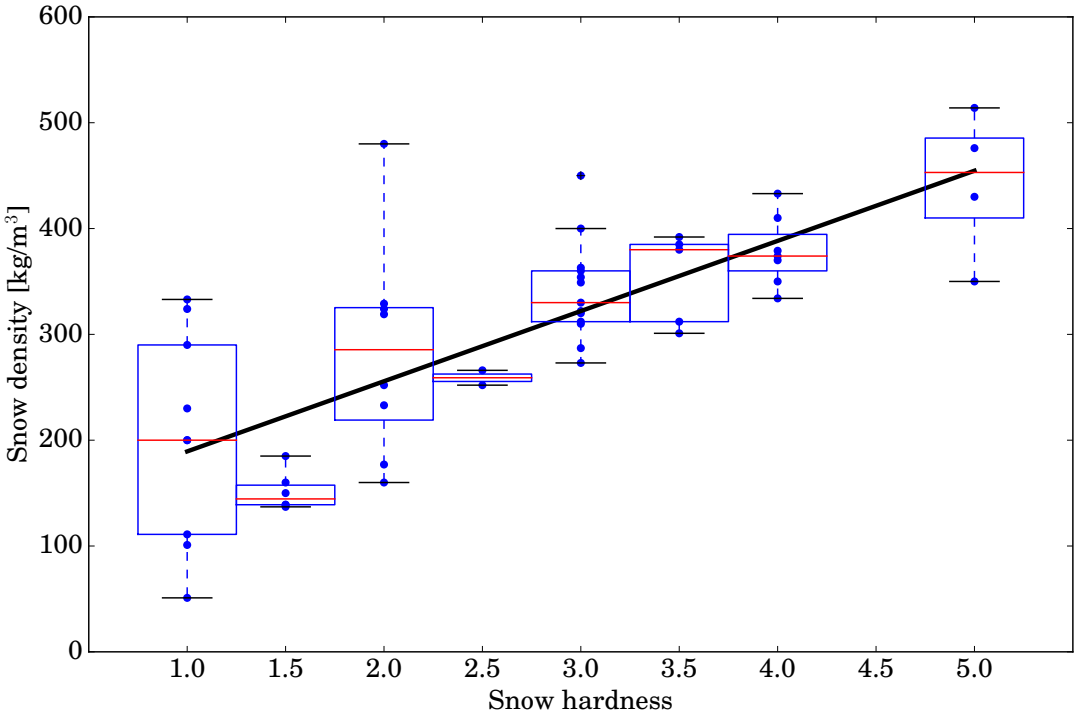

Figure 3.10: Relationship between snow hardness and snow density (blue dots) approximated with a linear model (black line). The distribution of snow densities for each snow hardness value is delineated by a boxplot.

Chapter 4

Sensitivity Analysis

The focus of this chapter is a sensitivity analysis to estimate the impact of snow parameters on C-band SAR backscatter. The setup of a simplified first-order radiative transfer model, in terms of describing the scattered radiation from a single-layer snow pack covering rough terrain, will be introduced in Section 4.1. Then, the model is fed with available snow profile measurements to show which snow parameters are of significant influence (Sec. 4.2).

4.1 Methodology

4.1.1 Theoretical Model

A first-order solution for bistatic radiative transfer problems has been presented in recent work (Quast and Wagner, 2016). It aims to model the total radar scattering and its contributions (volume, surface and interaction term) from a one-layered medium above a certain ground surface. Regarding the measurement configuration of Sentinel-1, only the monostatic case, i.e. backscattering into the same direction, is relevant. It is a non-polarimetric model, thus relations between different polarisations can't be analysed. Moreover, the model is provided as a user-friendly *Python* package named *RT1*[1], which enables an analysis of scattering by combining different surface and volume scatterers. The scattering properties of volumes and surfaces are defined via a series expansion in $\cos(\Theta)^n$, where n is the order and Θ the scattering angle. Within the mathematical representation of Θ, three weighting factors can be used to simulate scattering being dependent on the orientation of the incoming and outgoing beam in azimuth. This is referred to as anisotropic scattering. The expansion serves as an approximation of the volume phase function and Bidirectional Reflectance Distribution Function (BRDF) allowed by a few analytical functions (e.g., Rayleigh Phase function, Henyey–Greenstein phase function, cosine lobe function). These functions define specific scattering characteristics like directional scattering (i.e., scattering in a preferred direction), which is introduced as an

[1] see https://github.com/TUW-GEO/rt1

asymmetric factor t for the Henyey–Greenstein function, or the structure of the scattering lobe by using a cosine lobe model at a given order. In *RT1*, it is also possible to formulate scattering as a linear combination of different surface or volume scattering functions.

As already mentioned in Section 2.2, two additional parameters are needed to define the propagation of radiation through a volume, namely the optical depth τ and single-scattering albedo ω. Both can be related to snow conditions (e.g. snow depth, grain size, ...) using DMRT and other model formulations. More detailed instructions of how to compute τ and ω can be found in Appendix A.

4.1.2 Semi-empirical Model

To test the sensitivity of C-band backscatter with respect to changing snow parameters, surface backscatter has to be decoupled from volume backscatter over time. An example of a major impact on surface backscatter is a melting snow pack, which increases the liquid water content of the surface. Surface roughness is another important parameter and both are primarily governing the radar response from ground. An empirical model presented in Oh, Sarabandi, and Ulaby (1992) suggests that an increase of soil moisture or surface roughness leads to a higher backscatter. If one of both is dominant, it decreases the sensitivity of the second one. This fact can be used to define surface parameters being approximately time-invariant.

With a focus on a smaller alpine subregion near the meteorological station *"Obergurgl"*, surrounding points of the same land cover type were carefully picked with the visual aid of an RGB orthophoto (cf. Fig. 4.1). Two land cover types are dominant in the vicinity of Obergurgl, namely alpine meadows and rocky areas. For both of the classes about 30 points were selected while ensuring that the points cover a broad range of incidence angles. The result of the selection is visualised in Figure 4.1.

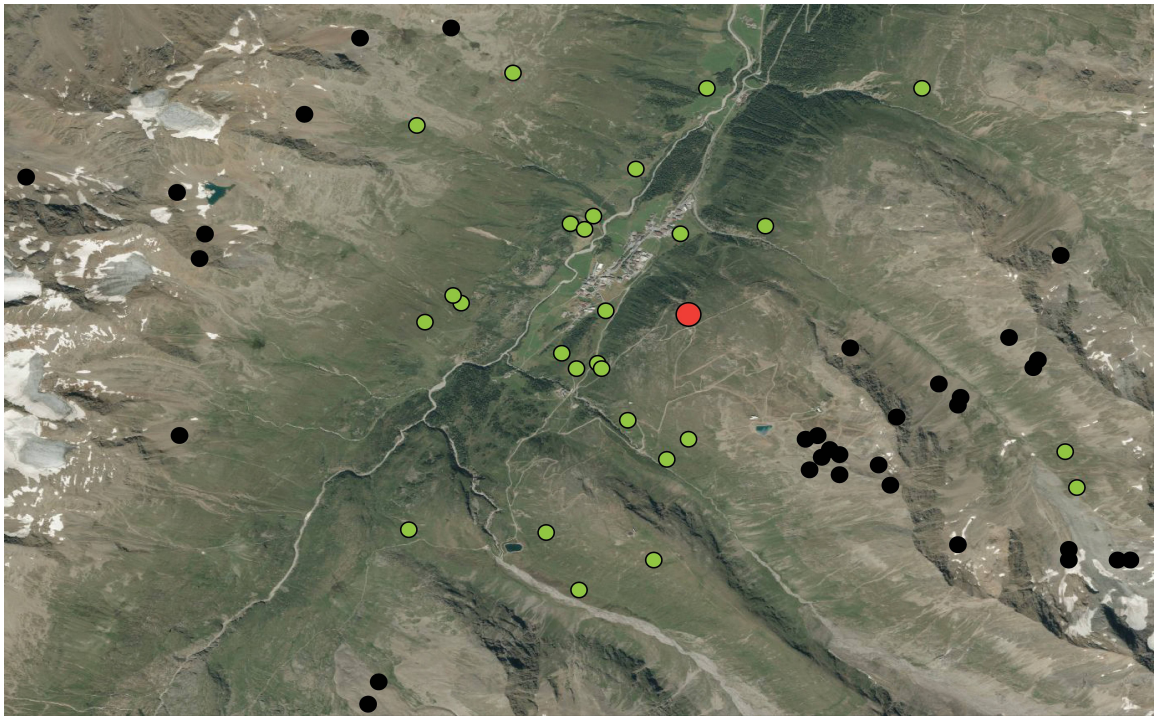

Figure 4.1: Overview map to show the picked points representing each land cover type, rocky areas (black dots) and alpine meadows (green dots). The meteorological measurement station *"Obergurgl"* is marked as a red dot (basemap: Orthofoto Tirol WMS, accessed on Oct. 19^{th}, 2018, URL: https://gis.tirol.gv.at/arcgis/services/Service_Public/orthofoto/MapServer/WMSServer?request=GetCapabilities&service=WMS).

The mean backscatter along with the precipitation data in Figure 4.2 delineate the variability of backscatter for both land cover types. Data was taken from the summer months July, August and September in 2016, which are assumed to be mostly snow-free. Backscatter from rocky areas is very stable over time, since it is less influenced by vegetation, precipitation and azimuthal looking directions (ascending or descending orbits) than over alpine meadows. A higher soil moisture resulting from previous precipitation events and senescence of vegetation could be a reasonable explanation for the behaviour of backscatter from alpine meadows. At the beginning of the chosen period, rocky areas seem to be still covered by wet snow due to the low backscatter value. Therefore, σ^0 data of the selected rocky area points from mid-July until the end of September was taken as a reference dataset to describe stable surface backscatter being less influenced by exterior impacts like a wet snow pack or rain.

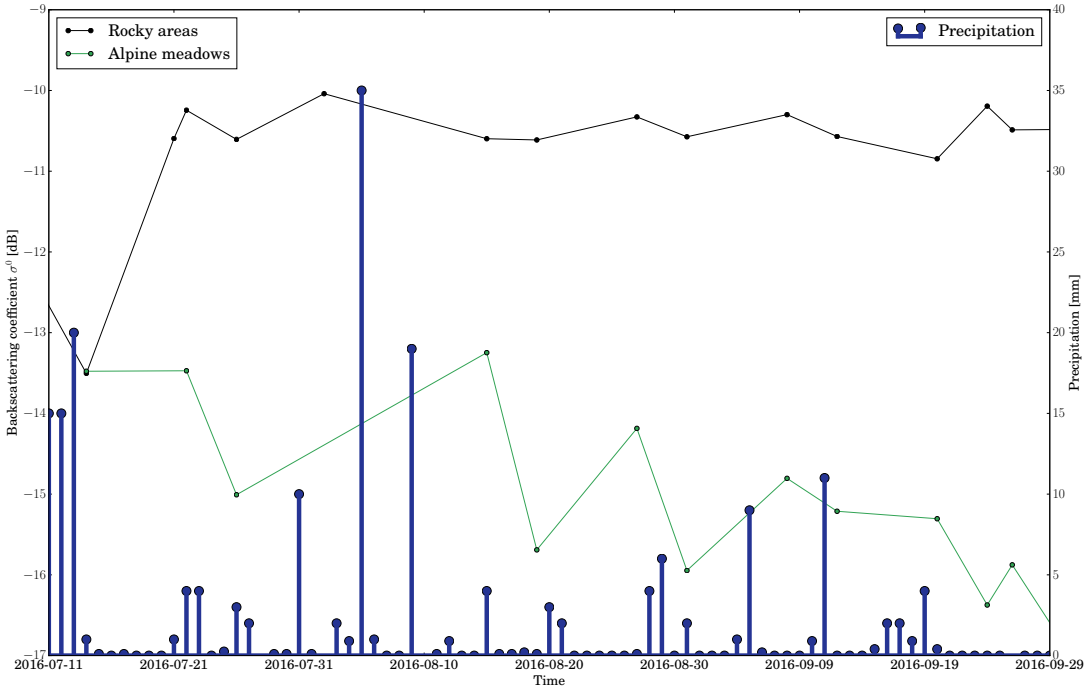

Figure 4.2: Mean backscatter for rocky areas and alpine meadows in comparison to measured precipitation data at station *"Obergurgl"*.

In a next step, the theoretical model *RT1* model was fitted to these measurements. This model was defined without a volume contribution (very low τ) and a Henyey-Greenstein function as a surface scatterer. Hence, the fit, i.e. the least squares adjustment, was performed on the directional parameter t and the normalisation factor n_{BRDF} of the BRDF. Averaging the fitted parameters over time resulted in $t = 0.2$ and $n_{\mathrm{BRDF}} = 0.08$, which corresponds to a high backscatter level (low n_{BRDF}) and a slight forward scattering (low

and positive t).

This semi-empirical, surface scattering model can now assist a sensitivity analysis for different snow packs above a rocky surface. The *RT1* model is extended by a volume scatterer based on a Rayleigh phase function, τ and ω. As already stated in previous sections, *RT1* is a first-order scattering model based on the assumption of a low scattering coefficient κ_s and it is not feasible to be used for describing a wet snow pack, since completely different scattering mechanisms are involved (cf. Sec. 2.3). To ensure that neither principle is violated, the selection of snow profiles is limited to dry snow packs (all wetness classes are 1). In addition, the stickiness is ignored, because it is a parameter which can hardly be derived from snow profile measurements (Picard, Sandells, and Löwe, 2018). An estimation of the fractional volume f_{vol} is possible according to the linear relation with snow hardness r_{snow} in Fig. 3.10:

$$f_{\text{vol}} = \frac{450}{5 \cdot 917} r_{\text{snow}} \tag{4.1}$$

where $917\,\text{kg/m}^3$ is the density of pure ice. Finally, an "ice-air" dielectric model is used for the micro-structure of the dry snow layer, where the dielectric constant of the snow grains and the background are set to $\epsilon_p = \epsilon_{\text{ice}}$ and $\epsilon_b = \epsilon_{\text{air}}$, respectively.

4.2 Estimated Backscatter Sensitivity to Dry Snow Parameters

By plugging the snow profile data into the model following the aforementioned restrictions, simulated backscatter was related to four snow pack parameters: snow height, grain size, snow temperature and snow density (derived from snow hardness) (Fig. 4.3). The backscatter was simulated for $\theta = 40°$, since it will serve as the reference angle for backscatter normalisation later on. According to this model, simulated backscatter shows no relation to snow height, snow temperature and snow density at all. The only snow parameter having an approximate second order correlation with backscatter is grain size (Fig. 4.3 (d)). The RGB colouring conveys the obvious fact, that the higher the total backscatter, the higher the contribution from volume scattering as surface scattering remains constant. Despite the positive correlation with grain size, all possible backscatter values are within the range of approximately 2 dB, which is governed by a changing snow pack. However, changes in surface conditions are completely neglected. This implies, that it will be very demanding or even impossible to find a correlation by simply comparing such snow parameters to backscatter. Approaches such as change detection or a cross polarisation ratio could offer a more reliable way to find a profound relation. However, one has to keep in mind, that coherent scattering is neglected in the herein first-order model simulations, which is thought to have a non-negligible impact on backscatter, when larger grains and wet snow are present. Therefore, it would be necessary to solve it by taking

all aspects of DMRT theory into account (Du, Shi, and Rott, 2010). Focusing on Figure 4.3, an increase in stickiness (e.g. to 0.2) would elevate the highest possible backscatter level from -6 dB to -2 dB.

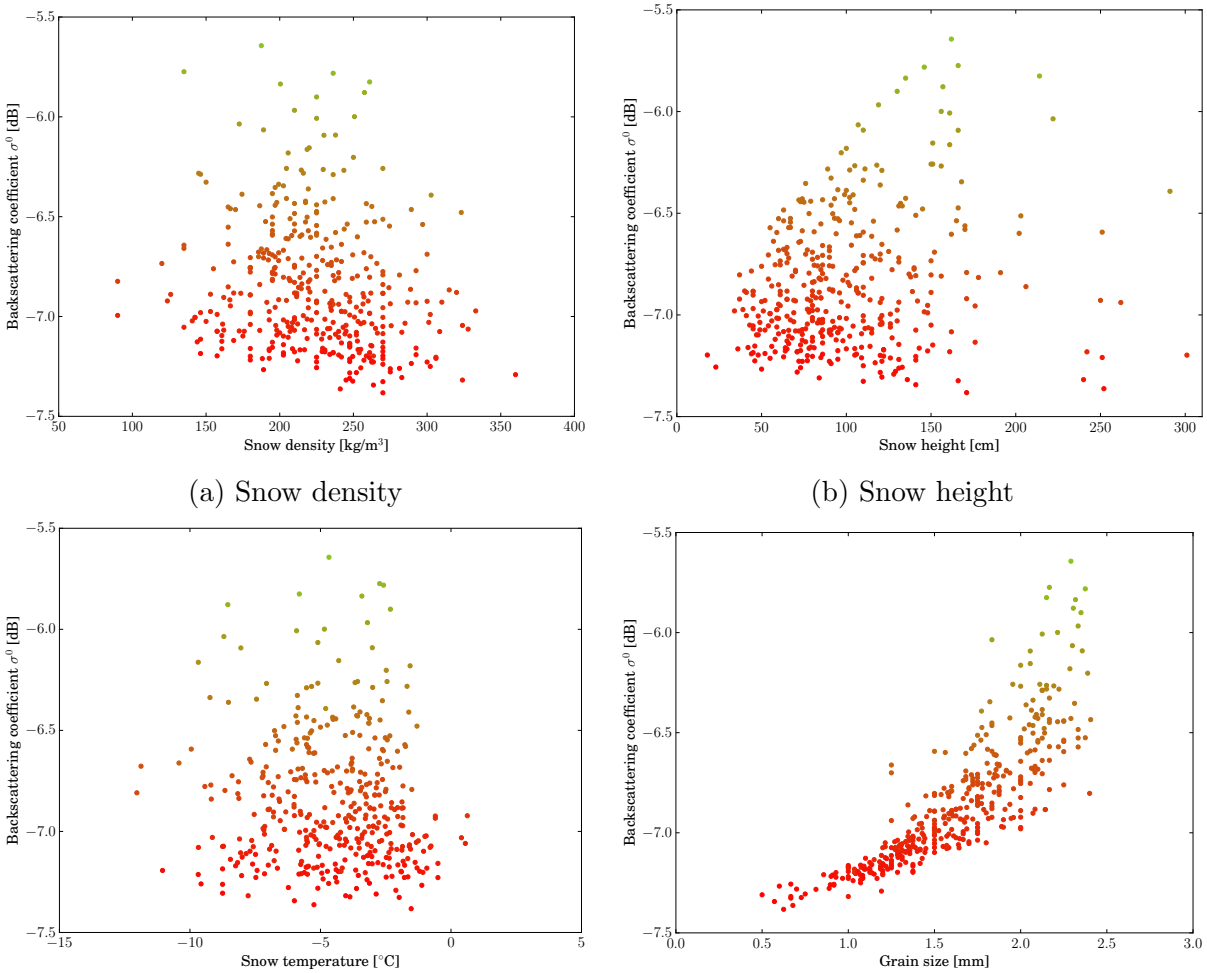

(a) Snow density

(b) Snow height

(c) Snow temperature

(d) Grain size

Figure 4.3: Simulated backscatter σ^0 for observed snow profile data at $\theta = 40°$ compared to four different snow parameters: snow density (a), snow height (b), snow temperature (c) and grain size (d). The RGB colour refers to the fraction of the scattered intensity from the surface I_{surf} (red), volume I_{vol} (green) and interaction I_{int} (blue) to the total intensity. Since surface scattering is clearly dominating and for visualisation purposes, I_{vol} and I_{int} were scaled by a factor of two.

Chapter 5

C-Band SAR Method Advancements

This chapter focuses on enhancing existing approaches to normalise backscatter (Subsec. 5.1.1, and 5.1.2) and reliably selecting reference images based on meteorological data in an automatised way. A benchmarking between the herein presented methods is performed in Section 5.2. This is necessary to assess the feasibility of the suggested advancements to relate them to snow parameter data later on.

5.1 Methodology

5.1.1 Radiometric Terrain Flattening

Radiometric terrain flattening is a relatively new approach to represent backscatter as γ^0, but additionally correcting for terrain, i.e. regions affected by layover and foreshortening (Small, 2011). Although Small (2011) includes detailed instructions of this methodology, essential steps and insights are summarised here, since the very method is available within *SNAP* and was used to process the data for this study.

Figure 5.1 illustrates the different reference unit areas used for normalising the observed radar backscatter β, the radar brightness. Beta nought can be normalised by using:

$$\beta^0 = \frac{\beta}{A_\beta} \tag{5.1}$$

However, β^0 is expressed in the slant range geometry, which is not a useful representation of backscatter, since it is not bound to an Earth model. An ellipsoid model or, better yet, a DEM can add spatial information to transform beta nought into a georeferenced quantity, for instance sigma nought σ^0 and gamma nought γ^0.

$$\sigma^0 = \beta^0 \frac{A_\beta}{A_\sigma} = \beta^0 \sin\theta \tag{5.2}$$

$$\gamma^0 = \beta^0 \frac{A_\beta}{A_\gamma} = \beta^0 \tan\theta \tag{5.3}$$

Hereby, θ might be the incidence angle derived from an ellipsoid model or from a DEM, which is then referred to as the local incidence angle, because the computation is based on the local neighbourhood.

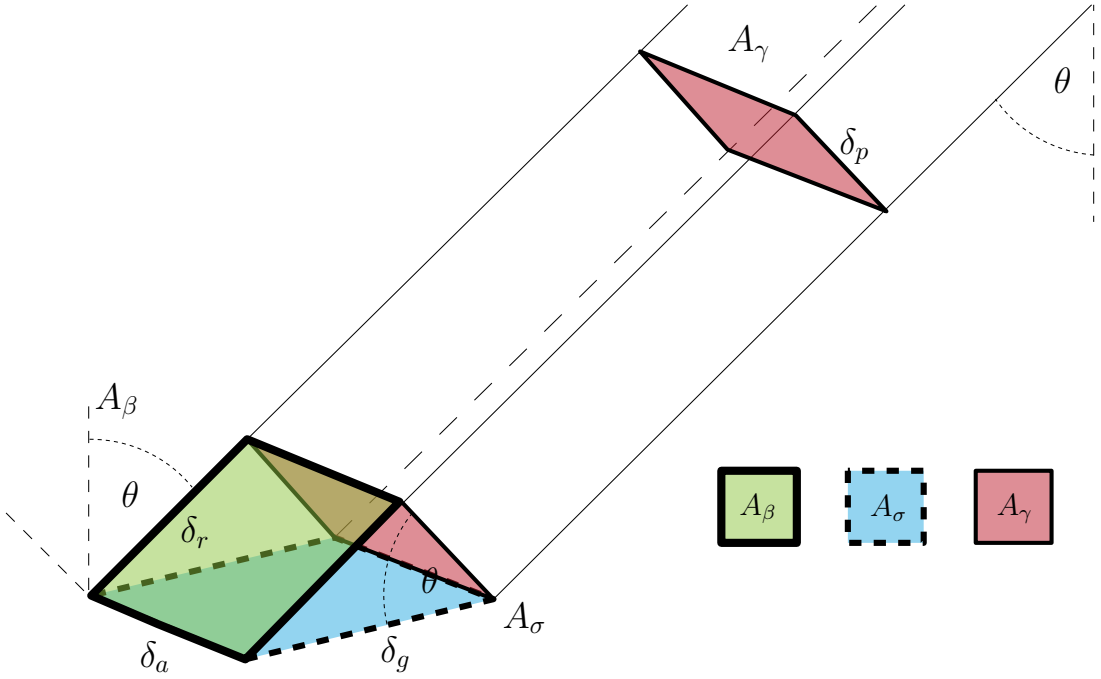

Figure 5.1: Normalisation areas related to the different backscatter representations β^0, σ^0 and γ^0. θ is the incidence angle, A_β the reference area in slant range, A_σ the reference area on ground and A_γ the reference area perpendicular to the looking direction. The extents of these areas are defined by means of the range resolution δ_r, azimuth resolution δ_a, ground range resolution δ_g and projected ground range resolution δ_p (Redrawn from Small (2011), from Fig. 2).

The radiometric normalisation methods above fail to include the illuminated area of the radar beam and to model the one-to-many and many-to-one relationship between the slant and ground range geometry appropriately, as they just rely on θ. The novelty of methods from Small (2011) tries to overcome these issues and gives preference to an estimate of the illuminated area instead of applying an incidence angle normalisation. At first, the proposed algorithm starts to integrate the local illuminated area by traversing a DEM. This area is estimated in a plane perpendicular to the slant range, thus yielding a reference area for retrieving a better estimate of γ^0. Its extent is defined by two triangular terrain facets, which include the neighbouring terrain heights at a given grid point, projected into this plane. Afterwards, each area grid point in the DEM geometry (easting E and northing N) is mapped to a related grid point in radar geometry (range r

and azimuth a). Overlapping area grid points are summed up, as it is the case in layover and foreshorting regions:

$$A_\gamma(r,a) \leftarrow A_\gamma(r,a) + A_\gamma(r,a)_{(E,N)} \tag{5.4}$$

Shadow regions are ignored and masked during the whole procedure. To smoothen the distribution of the area grid in radar geometry, bilinear resampling is applied. Finally, γ^0_{rtf} can be calculated in radar geometry as given below:

$$\gamma^0_{rtf}(r,a) = K_\gamma \frac{\beta^0(r,a)}{\hat{A}_\gamma(r,a)} \tag{5.5}$$

where K_γ is a calibration factor and

$$\hat{A}_\gamma(r,a) = \frac{A_\gamma(r,a)}{A_\beta} \tag{5.6}$$

an area factor estimate.

5.1.2 Piecewise Linear Percentile Slope (PLPS)

Backscatter normalisation with respect to the incidence angle θ is another way to overcome the influence of terrain, and even land cover to a certain extent (cf. Sec. 2.4). A trustful linkage of backscatter and in-situ measurements at different sites is hindered by the dependency of backscatter on incidence angles. Two ways of solving this problem are at hand: A simplified physical model is able to describe this relation, or backscatter normalisation is performed with respect to a certain reference angle θ_{ref}. For this study, the second option is chosen to be investigated further, since the physical-based models presented in Section 2.3 can't be applied to single frequency data at VV and VH polarisation. Moreover, as Section 2.4 already conveyed, incidence angle normalisation techniques for high-resolution backscatter data are still an open question in research, which makes it most interesting to examine the potential of new methods within the frame this study.

Eq. 2.2 seems to be a simple approach, but is characterised by a loss of generality due to the order of the cosine being sensible to land cover, which will be even worse for high-resolution data. Moreover, simply performing a linear regression to compute the slope of Sentinel-1 backscatter data such as for ASAR, where a lot of measurements at different incidence angles have been collected over the years, is also not thought to perform reliable enough for Sentinel-1 backscatter data. It is often the case, that data is only available from two orbits and therefore a slope estimation is ill-posed. Another issue is the separation of both orbits along θ. A large separation is preferred, since a larger range of θ is covered and extrapolation becomes less of an issue. To further minimise the necessity of extrapolation, $\theta_{ref} = 40\,^\circ$ seems to be an appropriate choice for the reference angle as the

mean value of θ tends to be around 40 °. Orbits are close to 40 ° in flat regions and 40 ° is approximately in the center of distinctively separated orbits in steep terrain.

The idea of the herein presented methodology is to discretise the backscatter distribution per orbit, instead of relying only on one single slope estimate for all orbits. Percentiles are thought to be the best choice for sampling the distribution, since they offer to derive a slope being dependent on the given backscatter distribution at a given θ and are less influenced by outliers. However, a linear regression between equal percentiles and their related θ does not work for a complex behaviour of backscatter with θ, i.e. a non-linear behaviour. This issue can be solved by going one step further in discretisation and connect each pair of neighbouring percentiles. Following the points in Figure 5.2, the steps of this procedure are:

1. First, the 5^{th}, 10^{th}, 25^{th}, 50^{th}, 75^{th}, 90^{th} and 95^{th} percentiles of backscatter are calculated for each orbit over the whole time period. For θ, the mean value is used instead of the percentiles.

2. To account for the case where a point (or the reference angle) in the θ-σ^0 space is not between two orbits, extrapolation is done. Hence, so called "virtual" orbits are constructed by using the slope of the closest pair of the 50^{th} percentiles (median). This is done according to a given minimum and maximum θ and the percentiles of the adjacent orbits are extrapolated, once for the lower and once for the upper "virtual" orbit.

3. Next, the backscatter values at θ_{ref} are determined for each percentile with respect to the closest orbits of a lower and higher θ.

4. Having the distribution and the reference backscatter values, normalisation can be initiated. For each θ-σ^0 pair, the same procedure as in (3) is repeated. Again, backscatter values are computed in between the neighbouring percentiles, but this time with respect to θ.

5. From the set of these synthetic backscatter values, the closest and adjacent two (σ^0_{upper} and σ^0_{lower}) are directly related to the actual measurement σ^0 as expressed in the following formula:
$$\mathrm{m}_{\text{norm}} = \frac{\sigma^0 - \sigma^0_{\text{lower}}}{\sigma^0_{\text{upper}} - \sigma^0_{\text{lower}}} \tag{5.7}$$

6. Eq. 5.7 defines the normalisation factor m_{norm}, which is used in the final step, the actual normalisation of σ^0:
$$\sigma^0_{\text{norm}} = \mathrm{m}_{\text{norm}} \cdot (\sigma^0_{\text{upper, ref}} - \sigma^0_{\text{lower, ref}}) + \sigma^0_{\text{lower, ref}} \tag{5.8}$$
$\sigma^0_{\text{upper, ref}}$ and $\sigma^0_{\text{lower, ref}}$ are the respective adjacent, synthetic backscatter values computed for θ_{ref} in step (3). These are directly known from step (5), where the indices of the neighbouring percentiles were calculated and stored.

Backscatter values above the 95th or below the 5th percentile are normalised with respect to the first and second closest synthetic backscatter value and are not declared as outliers, because they could be caused by special and, for some pixels, rare events (e.g. very low backscatter due to wet snow). Additionally, extrapolation is only allowed to a certain extent. As one can imagine, an estimate of a slope becomes poorer the closer all orbits are and the less all orbits cover the whole range of θ (cf. App. B). Therefore, pixels where the difference between θ and the closest orbit is larger than the difference between the lowest and highest orbit, are masked and ignored during the normalisation procedure. Figure 5.6 (d) illustrates the applicability of the PLPS backscatter normalisation method when being compared to the original backscatter data in Figure 5.6 (a).

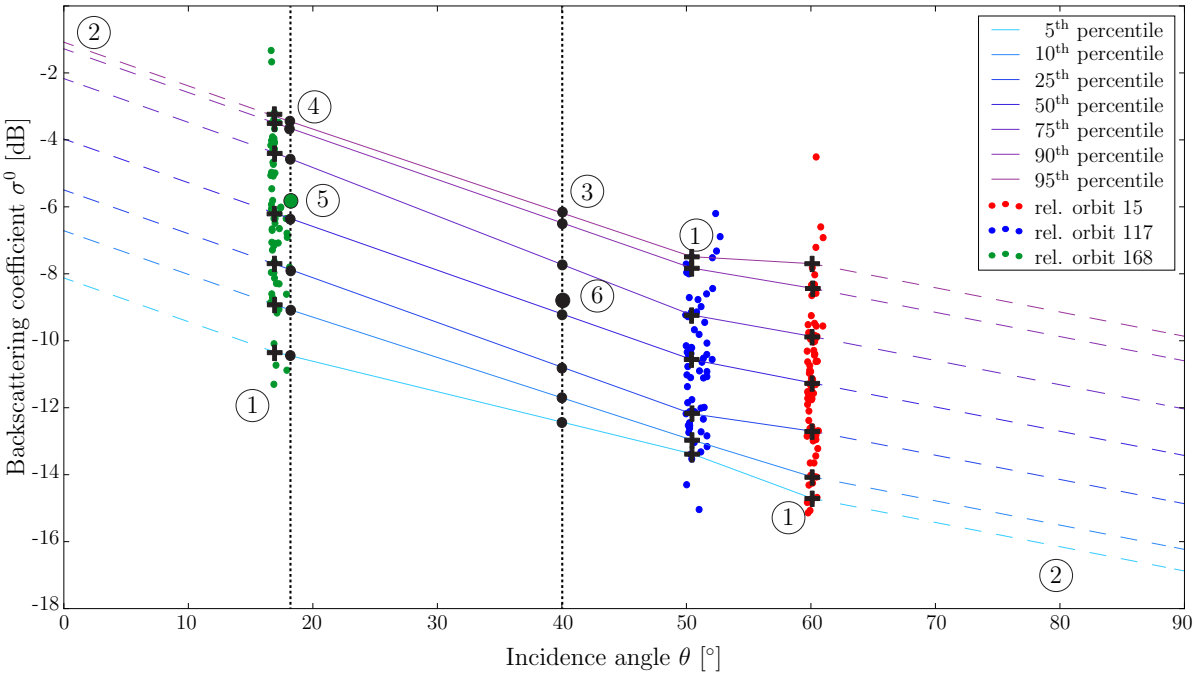

Figure 5.2: Overview of the necessary steps needed for normalising backscatter with the PLPS method. Measurements are shown in yellow, blue and red (relative S-1 orbit numbers 15, 117 and 168). For each orbit, the 5th, 10th, 25th, 50th, 75th, 90th and 95th percentile (✚) are computed and connected to form a line covering the whole range of incidence angles. The slope of the 50th percentile defines extrapolated lines, which are depicted as dashed lines. Vertical cuts intersect the lines at the reference incidence angle and at the measurement (•) to retrieve representative backscatter values to normalise backscatter in a final step.

5.1.3 Synthetic Reference Image Selection for Change Detection

The herein presented reference image selection is inspired by Nagler and Rott (2000) and Nagler, Rott, et al. (2016) to separate the backscatter of a snow pack from surface backscatter. In addition, the selection is explicitly assisted by continuously measured weather data as introduced in Section 3.2.3. Past studies relied on a selection of one image, which is reasonable for a smaller test site. However, as this thesis aims to compare backscatter measurements with snow profile data on a larger scale, a selection of a reference backscatter value is thought to be most reliable at pixel level. To detect the most appropriate backscatter values in a time series, meteorological data has to be interpolated at each pixel.

The interpolation of the given weather data has to be adapted according to the spatial behaviour of the climate variable, i.e. the daily maximum temperature and accumulated precipitation. In mountainous regions, changes of the former are highly correlated with height (cf. Fig. C.1 in Appendix), whereas the latter is mainly driven by a variation of the horizontal position. Hence, instead of taking advantage of a simple linear relation, as it is the case for height and maximum temperatures, interpolation of precipitation has to be handled differently. A well-known method allowing a 2D interpolation of such type of data is Inverse Distance Weighting (IDW) (Shepard, 1968). It is based on a weighted average of n (precipitation) measurements p_i and the weights are defined with respect to the euclidean distance (d_i) between the point of interest (POI) and the location of the measurement.

$$p_{\mathrm{POI}} = \frac{\sum_{i=0}^{n} \frac{1}{d_i} p_i}{\sum_{i=0}^{n} \frac{1}{d_i}} \tag{5.9}$$

In Eq. 5.9 p_i (for Station i) is a weighted average similar to IWD and instead of focusing on a single measurement at a given time, measurements are averaged over past times. The spatial distance is replaced by the temporal difference of the current and past timestamp:

$$p_i = \frac{\sum_{j=t-k}^{t} \frac{1}{t-j+1} p_{i,j}}{\sum_{j=t-k}^{t} \frac{1}{t-j+1}} \tag{5.10}$$

where t is the current timestamp and k the amount of temporal neighbours in the past. Eq. 5.10 should yield a value, which represents averaged, past precipitation conditions, to enable a description of the longer lasting influence of soil moisture or a snow pack infiltrated by rainfall.

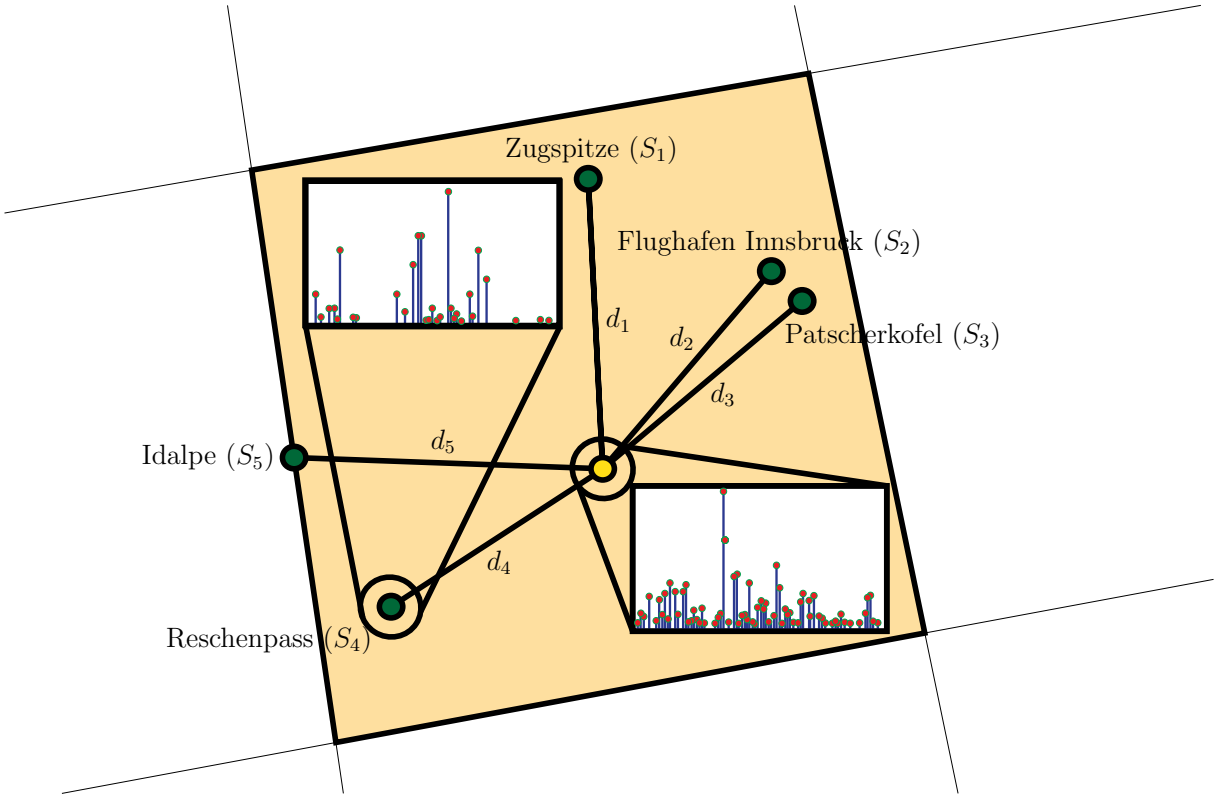

Figure 5.3: Sketch of the IDW method to interpolate precipitation data at a location of interest (yellow dot). Data from five stations (*"Zugspitze"* (S_1), *"Flughafen Innsbruck"* (S_2), *"Patscherkofel"* (S_3), *"Reschenpass"* (S_4) and *"Idalpe"* (S_5)) are taken into account. Two precipitation time series are compared, one acquired at station *"Reschenpass"* and one interpolated by using all data.

Figure 5.3 illustrates this interpolation procedure for the chosen Equi7 Grid tile and the five meteorological measurement stations. Missing data can be overcome, since only one measurement per timestamp is needed, as a minimum.

A selection of a reference backscatter image should then be accomplished with the aid of the interpolated meteorological data for three different use cases (words written in italic represent an abbreviation for a synthetic reference image selection method):

- minimum temperatures per pixel → *coldest*
- minimum precipitation per pixel and minimum temperatures overall → *driest*
- maximum temperatures per pixel and minimum precipitation overall → *hottest*

The coupling of both weather parameters for the last two points is not fully done on a pixel basis to avoid undesired, disturbing patterns. Additionally, randomness and speckle

in the backscatter data could be reduced by averaging the top synthetic reference images for each of the settings above. Of course, this should be only done for those images, which seem to be visually appropriate for being taken into account as a reference image, i.e. no areas with low backscatter values due to snowmelt are present in mountainous terrain.

5.2 Method Benchmarking

5.2.1 Backscatter Representation

So far, two ways to normalise high-resolution backscatter with respect to θ have been presented. Either a linear regression can be performed to tilt each σ^0 according to the estimated slope or normalisation is based on the PLPS method. As no "true" reference data is available, both methods demand a comparison. Figure 5.4 shows an orbit-wise distribution of σ^0 for one pixel along with a linear (a) and a PLPS model (b). It is very rare that a pixel is covered by four orbits, which is only achieved for small regions at the edge of the Equi7 Grid tile of interest, and is therefore very important to judge the applicability of both methods. Figure 5.4 (a) conveys that a linear regression approach works well, but Figure 5.4 (b) clearly surpasses (a) in terms of the backscatter distribution at 40°. This is mainly due to the adjusted arrangement of the normalised backscatter by means of the percentiles of neighbouring orbits.

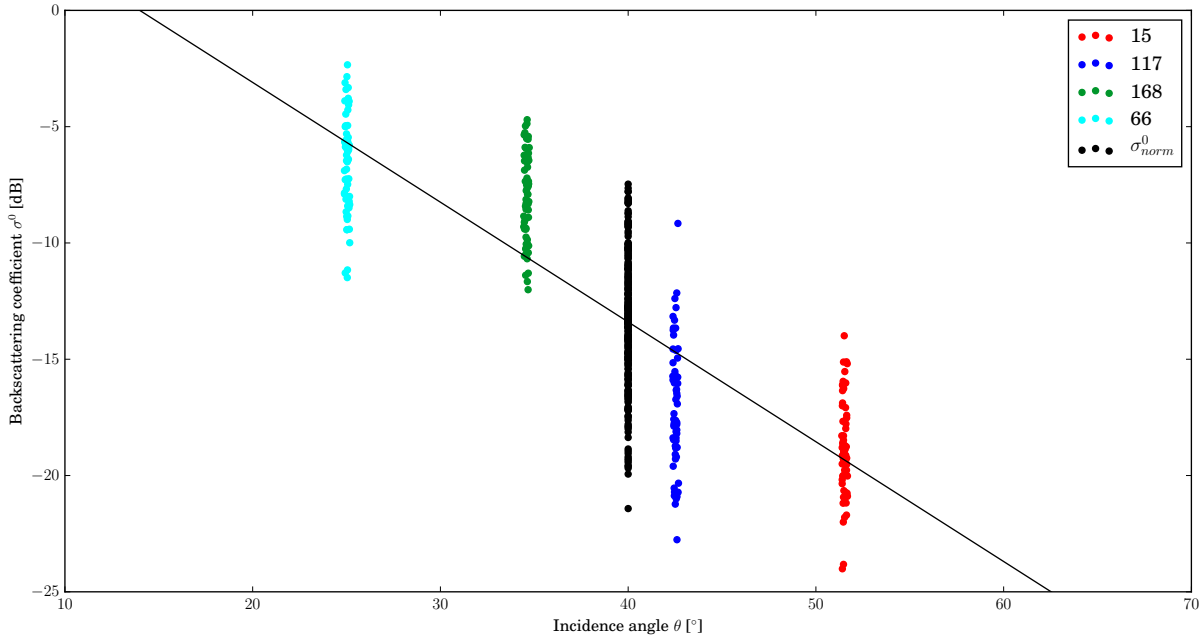

(a) Backscatter normalisation with linear regression (black line).

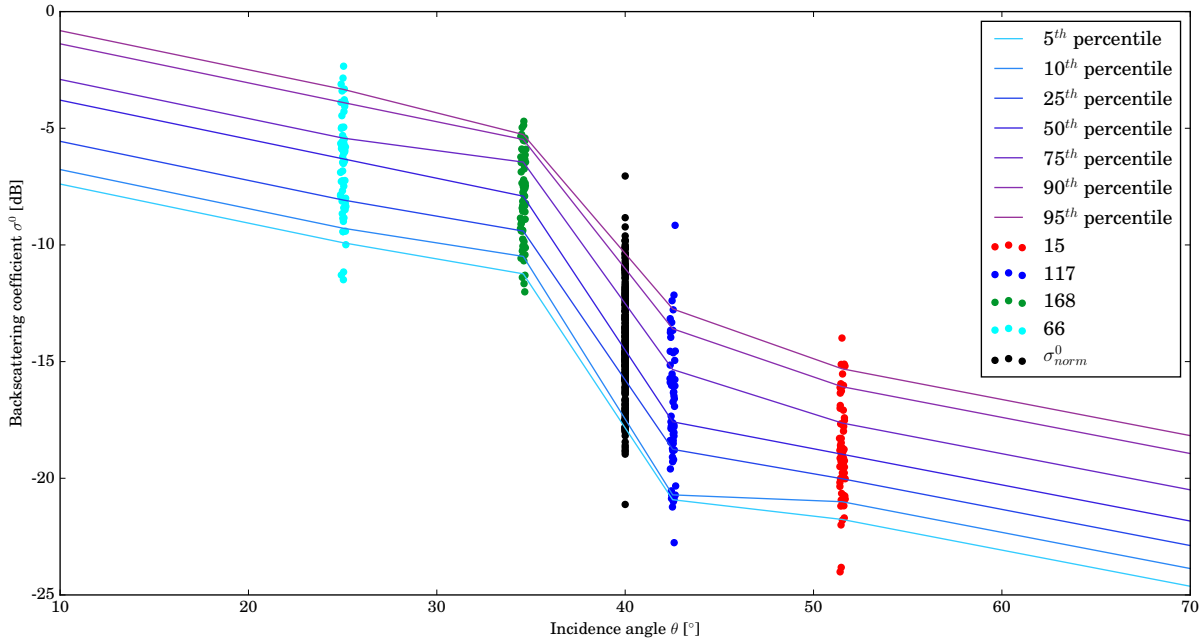

(b) Backscatter normalisation with PLPS (percentile colour gradient from turquoise to purple).

Figure 5.4: Comparison of σ^0_{norm} for two backscatter normalisation methods, LR (a) and PLPS (b). All parameters are estimated for the whole time series of σ^0 for one pixel (x=4803458 m, y=1587908 m in Equi7 Grid coordinates).

From now on, normalised backscatter will be denoted as σ^{40}_{PLPS} for the PLPS method and σ^{40}_{LR} for the LR method. Both normalised backscatter representations are compared to σ^0 backscatter as time series in Figure 5.5. σ^0 is clearly affected by the viewing geometry resulting in a strong variation of backscatter for each measurement. The proposed normalisation methods appear to correct this influence well, thus reducing the variance, but still preserving essential information about the seasonal cycle of backscatter. As already underlined by Figure 5.4, σ^{40}_{PLPS} has a lower variance than σ^{40}_{LR}.

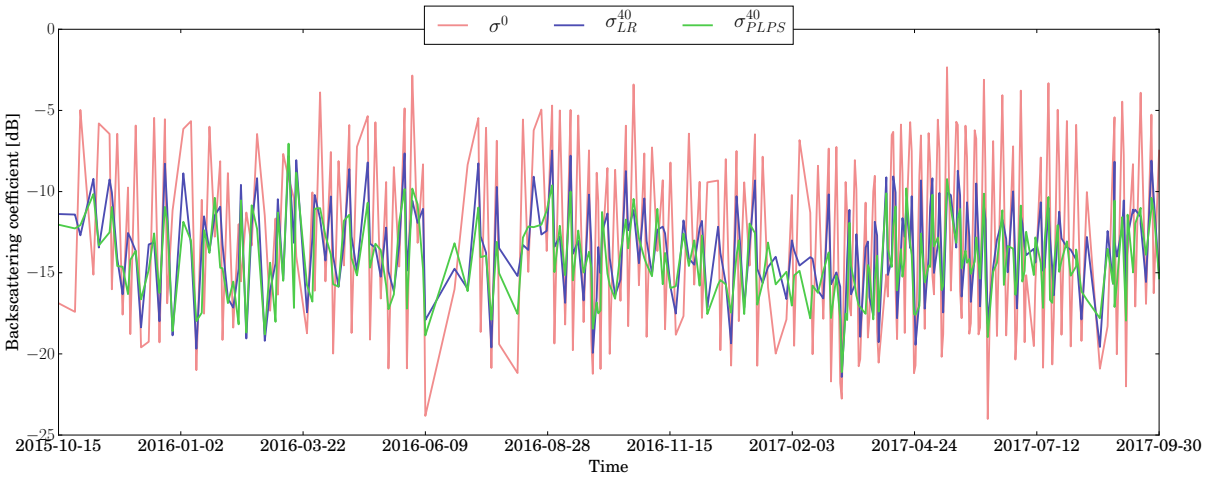

Figure 5.5: Comparison of σ^0 to both normalised backscatter representations, σ^{40}_{PLPS} and σ^{40}_{LR} (VV polarisation). The depicted time series refers to one pixel and ranges from October 15$^{\text{th}}$, 2015 to September 30$^{\text{th}}$, 2015 (x=4803458 m, y=1587908 m in Equi7 Grid coordinates).

The comparison in Figure 5.6 suggests that all methods are able to correct for terrain. Steep, bright areas affected by layover and foreshortening are clearly visible in Figure 5.6 (a), whereas, the effect of varying terrain has diminished in Figures 5.6 (b), (c) and (d). Moreover, lower backscatter values, primarily caused by snowmelt, become visually more obvious. As the results imply that all methods perform equally well, an inter-comparison for reviewing the differences in more detail is proceeded later on. It has to be noted, that the radiometric terrain flattening algorithm in Small (2011) is the only method, which corrects problematic regions in a rigorous (model-driven) way. Therefore, it intuitively seems to be the backscatter representation to favour, however, at an expense of a higher computation time and the disadvantage of another necessary step to normalise data with respect to the remaining incidence angle behaviour.

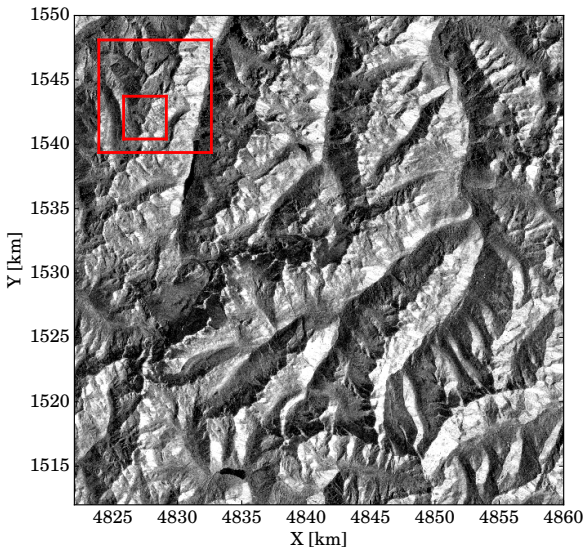

(a) σ^0 backscatter image

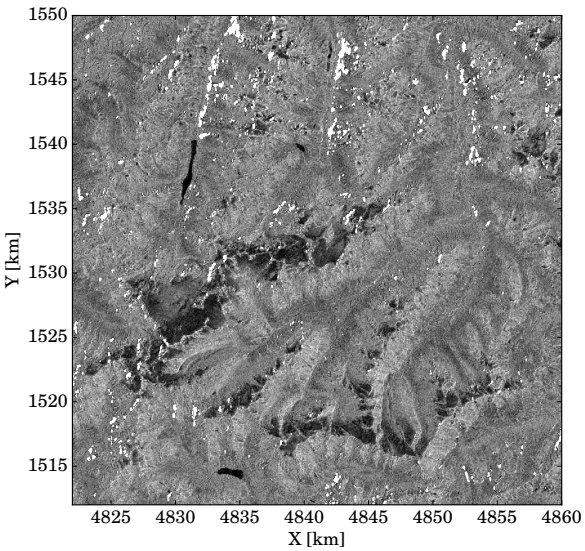

(b) γ^0_{rtf} backscatter image

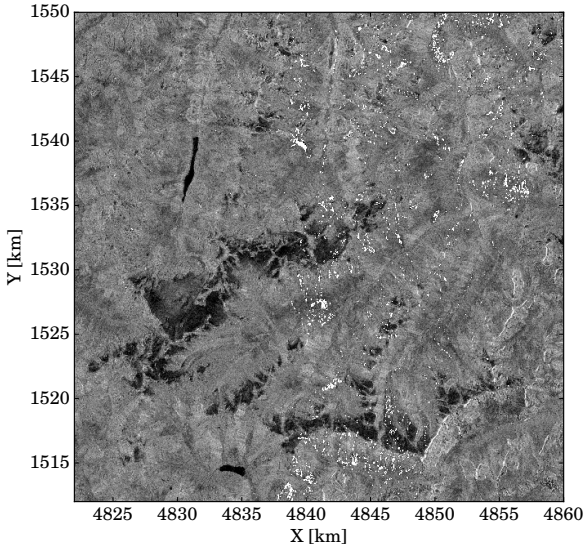

(c) σ^{40}_{LR} backscatter image

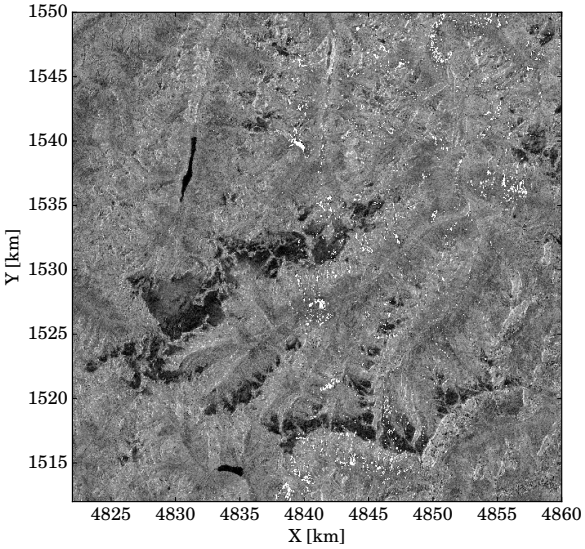

(d) σ^{40}_{PLPS} backscatter image

Figure 5.6: Comparison of σ^0, γ^0_{rtf}, σ^{40}_{LR} and σ^{40}_{PLPS} in VV polarisation over mountainous terrain for an acquisition on June 27$^{\text{th}}$, 2017. γ^0_{rtf} masks areas characterised by radar shadow, whereas σ^{40}_{LR} and σ^{40}_{PLPS} exclude pixels with an unfavourable orbit distribution. The spatial extent of the depicted region is shown in (a). The red outer box represents the boundaries of the Equi7 tile *"E048N015T1"* and the red inner box depicts the extent shown in the figures above.

Finally, a spatial comparison of the difference between σ^{40}_{PLPS} and σ^{0}_{LR} (b), γ^{0}_{rtf} and σ^{40}_{LR} (c) and γ^{0}_{rtf} and σ^{40}_{PLPS} (d) is displayed in Figure 5.7. Residuals in Figure 5.7 (b) clearly outline the terrain in Figure 5.7 (a), which means that σ^{40}_{PLPS} is sensitive regarding the arrangement of the orbits. This was revealed by a similar analysis as depicted in Figure 5.4. On slopes facing the sensor, the distribution is much more favourable, as some orbits are close to 40°. Figure 5.7 (d) confirms this, since residuals are close to zero for south-east looking slopes. On the other hand, slopes looking in the opposite direction have orbits resulting in low and high incidence angles. As an example, two of three orbits are in the lower range of θ, but their backscatter distribution is still separated distinctively due to higher backscatter at lower incidence angles. This causes σ^{40}_{PLPS} to significantly differ from σ^{40}_{LR}.

Figure 5.7 (c) conveys a clear impression in terms of limiting the terrain influence, whereas this is not the case for Figure 5.7 (d). Large residuals are present at areas affected by layover, which is taken care of by the radiometric terrain flattening method. In summary, σ^{40}_{LR} is ought to be preferred in general, but σ^{40}_{PLPS} is superior as long as the spreading of the orbits along θ is adequate.

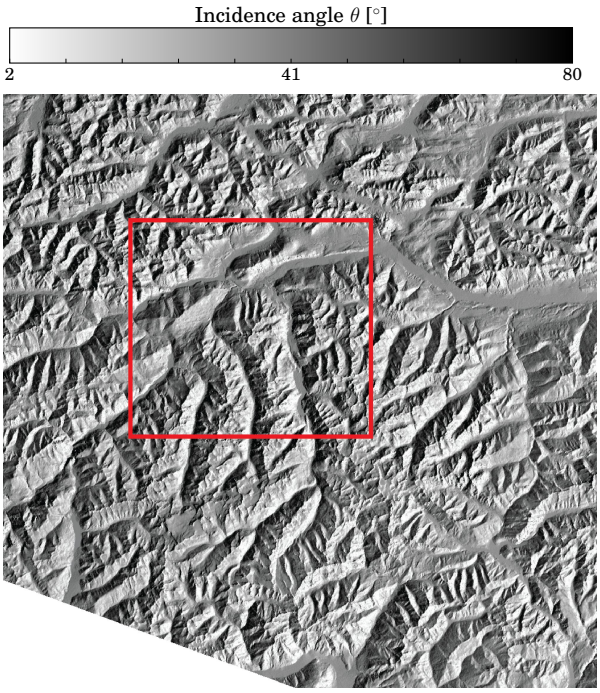

(a) PLIA image and residual subregion for (b), (c), (d) in red

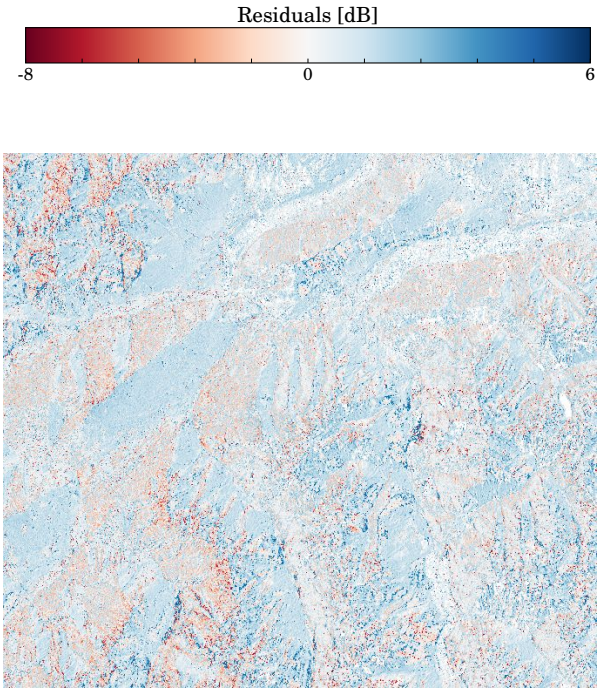

(b) Residuals of σ^{40}_{PLPS} and σ^{40}_{LR}

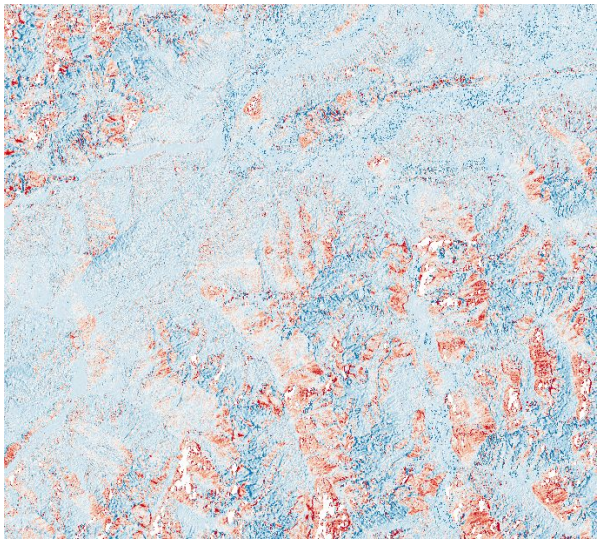

(c) Residuals of γ^{0}_{rtf} and σ^{40}_{LR}

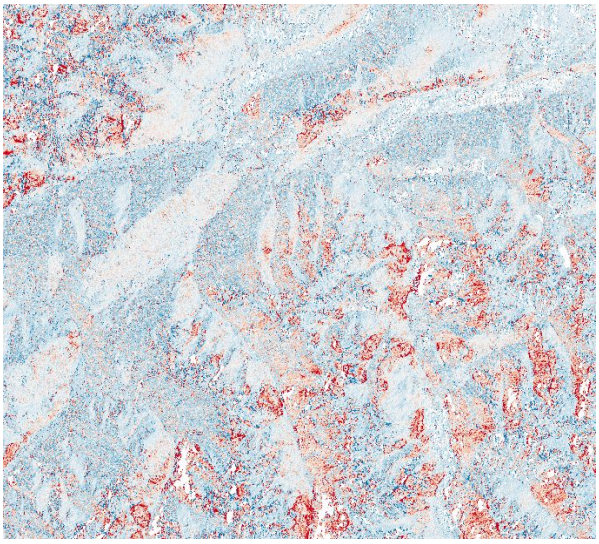

(d) Residuals of γ^{0}_{rtf} and σ^{40}_{PLPS}

Figure 5.7: Comparison of all residuals after difference formation σ^{40}_{LR}, σ^{40}_{PLPS} and γ^{0}_{rtf} with each other. The depicted residuals result after shifting the distribution with respect to the mean. The images in VV polarisation show an acquisition on May 27$^{\text{th}}$, 2016 for a subregion marked in (a).

5.2.2 Feasibility of Reference Image Synthesis

The synthetic reference image generation is based on linear interpolation of the temperature data and on spatiotemporal IWD interpolation of the precipitation data. The performance of both methods is validated by setting simulated and measured data at a meteorological measurement site in relation with each other over time (i.e. by ignoring the station of interest during interpolation). The following tables list statistical measures such as the RMSE, pearson correlation and spearman correlation for interpolating temperature (Tab. 5.1) and precipitation (Tab. 5.2).

Table 5.1: Maximum temperature statistics (in °C) from July 1st, 2015 to September 30th, 2017

Station	RMSE	Pearson R	Spearman R
Flughafen Innsbruck	5.9	0.84	0.84
Patscherkofel	1.7	0.98	0.98
Zugspitze	2.7	0.96	0.95
Reschenpass	3.5	0.92	0.92
Idalpe	2.0	0.99	0.99

Table 5.2: Precipitation statistics (in mm) from July 1st, 2015 to September 30th, 2017

Station	RMSE	Pearson R	Spearman R
Flughafen Innsbruck	7.3	0.81	0.87
Patscherkofel	4.7	0.79	0.82
Zugspitze	7.8	0.53	0.72
Reschenpass	4.5	0.66	0.58
Idalpe	3.6	0.76	0.82

As the interpolation of temperature data follows the behaviour of temperature (usually) decreasing with altitude, the chosen model is sufficient and good agreement is given in Tab. 5.1. Station *"Flughafen Innsbruck"*, which is located in *"Inntal"*, performs worst in Tab. 5.1, since its temperature changes may be triggered by other variables than just height. Station *"Zugspitze"* is the only station north of the *"Inntal"* valley, thus different weather phenomena compared to the southern part of the Alps could take place. This is confirmed by a weak correlation and a high RMSE in Tab. 5.2. Moreover, the significant gap between Pearson and Spearman correlation in Tab. 5.2 points out that there are remaining non-linear systematics in the data, which can not be modelled correctly with the IDW method. In terms for both variables, *"Idalpe"* can be simulated best. This analysis should only expound the possibilities of both methods, but regarding the selection of the synthetic reference image only relative changes in the time series are relevant, whereas absolute values are not important.

For the aforementioned use cases in Section 5.1.3, the primary choices for the synthetic reference image selections are shown in Figure 5.8. Further, Figure 5.8 (a) assists the visualisation of minimum temperature in Figure 5.8 (b) (*coldest* synthetic reference image) with temporal information. Three selections took place, one for the upper part, one for most of the lower part and one for the highest regions. Unfortunately, the full coverage is not given on January 18th, 2017, when the coldest conditions were prevalent. Figure 5.8 (c) and (d) use a combination of both temperature and precipitation data. Figure 5.8 (c) is the result of the IDW method followed by choosing the minimum interpolated precipitation values in the time series at overall minimum temperature (*dryest* synthetic reference image). Station *"Zugspitze"* appears to have measured precipitation more often, which is not restricted to be zero regarding minimum values, as temporal averaging is performed in addition (cf. Subsec. 5.1.3). Figure 5.8 (d) is constructed in a similar way, but this time maximum temperature and overall minimum precipitation are chosen as criteria to approximate a snow-free reference image selection (*hottest* synthetic reference image). The resulting impact of each synthetic reference image on change detection is not clear at this point, but will be finally discussed in Chapter 6.

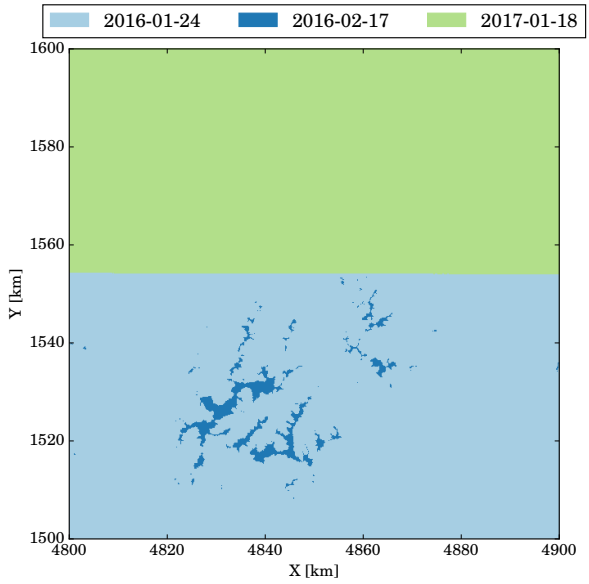

(a) Selection time stamps of backscatter images for case (b).

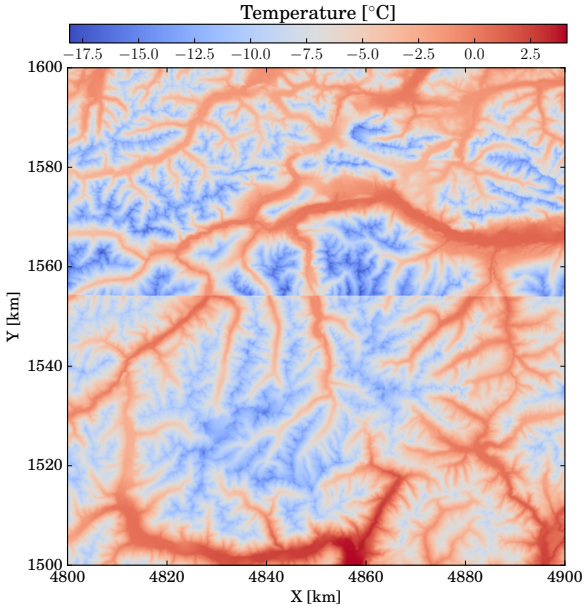

(b) Temperature conditions for the *coldest* synthetic reference image.

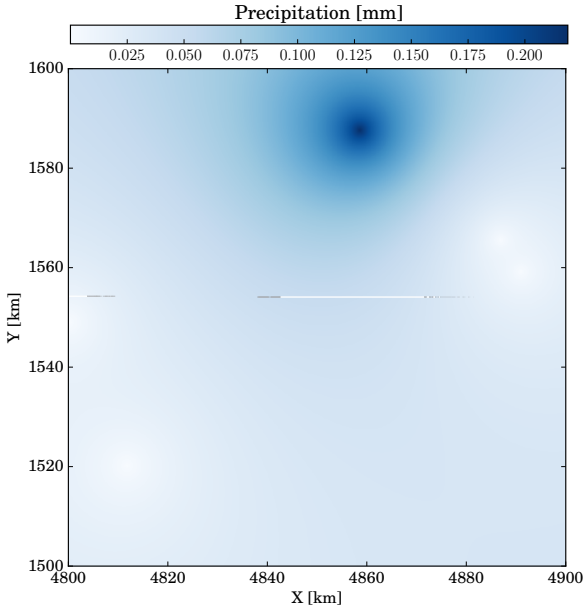

(c) Precipitation conditions for the *dryest* synthetic reference image.

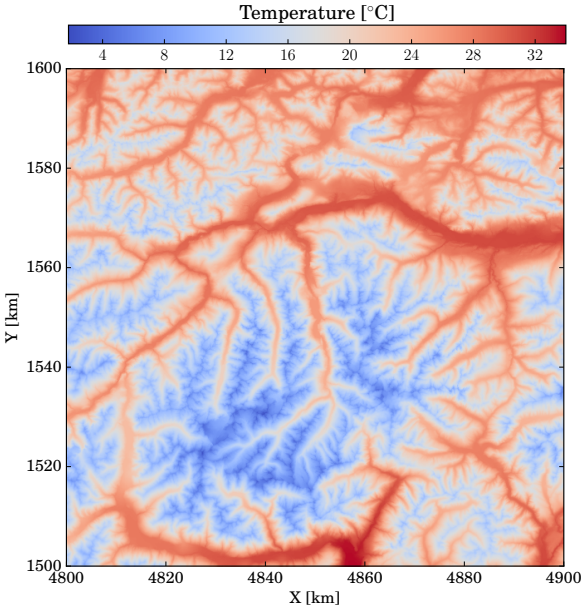

(d) Temperature conditions for the *hottest* synthetic reference image.

Figure 5.8: Comparison of the interpolated weather data for all three different synthetic reference image selection methods (relative S-1 orbit number 117). Coordinates are given in the Equi7 Grid system.

Chapter 6

Results and Discussion

The previous chapters covered theoretical and empirical relationships between snow parameters and backscatter (Ch. 4) and demonstrated new approaches to represent backscatter (Ch. 5). Hitherto, relationships between various backscatter and snow parameter representations are still unclear, but shall be investigated in this chapter. Not only σ^0, γ^0_{rtf}, σ^{40}_{PLPS} and σ^{40}_{LR} will be investigated (Sec. 6.1), also change detection (Sec. 6.4) and the cross-polarisation ratio (Sec. 6.3) are of great interest (cf. Sec. 2.3). Remaining obscurities shall be eliminated with the aid of a time series analysis, which compares snow parameter and C-band SAR backscatter variations over time (Sec. 6.5). As a temporal criteria, snow pack measurements being closest in time to the satellite acquisition, were selected for all further investigations.

6.1 Correlations of C-Band SAR Backscatter and Snow Parameters

First, overall statistics can be calculated by relating the aforementioned backscatter variables σ^0, γ^0_{rtf}, σ^{40}_{PLPS} and σ^{40}_{LR} for each polarisation, VV and VH, to a representative parameter of the snow pack. Snow profile parameters given for each snow pack layer, e.g. grain size or snow wetness, have to be aggregated by using for instance the mean or maximum value. This has led to a selection of the following snow parameters:

- air temperature (AT)
- number of layers (LA)
- snow height/depth (SD)
- maximum grain size ($\widehat{GS}$)
- maximum snow wetness ($\widehat{SW}$)
- maximum snow hardness ($\widehat{SH}$)
- mean grain size ($\overline{GS}$)
- mean snow hardness ($\overline{SH}$)
- mean snow wetness ($\overline{SW}$)

Unfortunately, due to a lack of data availability, reducing the significance of any correlation, snow temperature data was excluded.

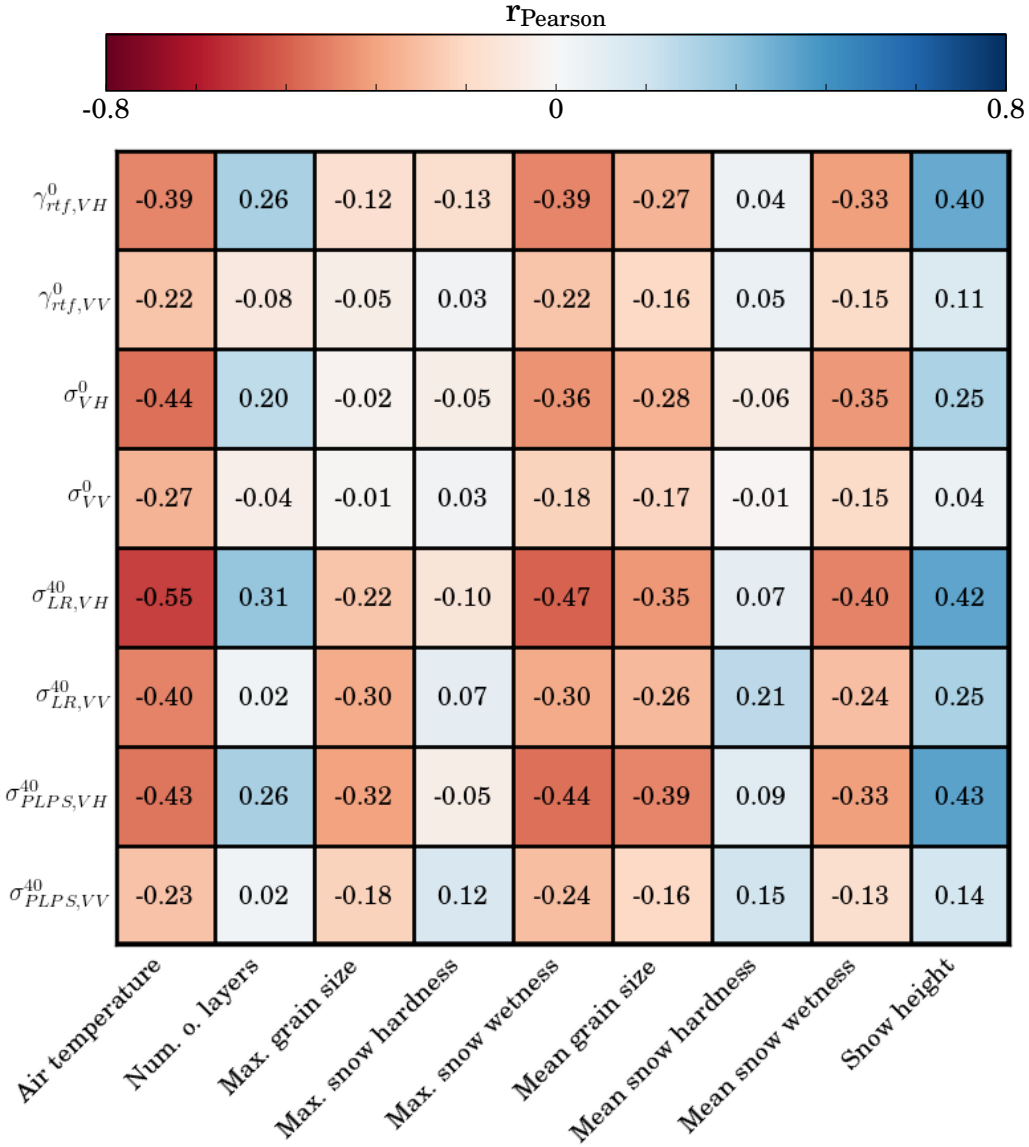

Figure 6.1: Pearson's correlation coefficient $r_{Pearson}$ resulting from relating backscatter data to snow parameter data. Visual guidance is given through a colourisation of $r_{Pearson}$, where negative correlation is coloured as red and positive as blue.

Figure 6.1 illustrates the overall Pearson's correlation coefficients $r_{Pearson}$ as a matrix. This metric is a measure of a linear relationship between two variables x and y (Hall, 2015):

$$r_{Pearson} = \frac{C_{xy}}{\sigma_x \sigma_y} \tag{6.1}$$

where σ_x is the standard deviation of x, σ_y is the standard deviation of y and C_{xy} is the covariance between x and y.

By comparing the backscatter representations with each other, one can conclude that normalised backscatter leads to superior results, with σ^{40}_{LR} ahead. This follows the expectations of normalised backscatter being not only less dependent on terrain variations (that were corrected for in γ^0_{rtf}), but also on the land cover type. As an example, volume backscatter becomes more important at higher incidence angles when dense vegetation is present, which is directly considered by means of linear regression, since the slope tends to be close to zero (Sabel et al., 2010).

Moreover, VH polarisation has a higher correlation for all snow parameters, which underlines the fact of multiple scattering and perhaps also the greater sensitivity with respect to fluid retention in a snow pack (cf. Appendix D). Snow parameters such as air temperature, maximum snow wetness, mean grain size and mean snow wetness are characterised by a larger negative correlation, whereas snow height and the number of layers are positively correlated with backscatter.

However, one has to keep in mind, that all snow parameters influence the backscatter dynamics in a coupled way. This could be the case for snow parameters with a negative $r_{Pearson}$, all ought to be dependent on snow wetness ($r_{Pearson} = -0.47$). Thus, as shown in Section 3.3, larger grains occur when the snow pack contains wet snow or is governed by past melt-freeze cycles ($r_{Pearson} = -0.39$ for $\sigma^{40}_{PLPS,VH}$). The same is true for air temperature with a maximum correlation of -0.55: the warmer, the higher the probability of the presence of wet snow. A positive correlation with snow depth ($r_{Pearson} = 0.43$) and the number of layers ($r_{Pearson} = 0.31$) is meaningful (more volume scattering), but is not necessarily the only cause of the depicted correlations in Figure 6.1. It could be the case that these positive correlations are affected by the site and the land cover itself, i.e. the general level of the surface backscatter.

Snow hardness is not correlated at all, since all correlations are around 0.1. This is possibly resulting from the ambiguity in the subjective measurement method itself. There seems to be a linear relation with snow density at hand (cf. Fig. 3.10), however, there are larger deviations for lower snow hardness values. This implies a decorrelation of snow hardness with respect to snow density and backscatter. At low values (dry snow) the deviation is larger, at high values snow wetness will probably dominate C-band SAR backscatter.

Additionally, correlations were also reviewed in terms of filtered snow parameter data, e.g. excluding snow packs classified as wet (i.e. having a focus on dry snow parameters), using only snow packs covering rocky surfaces (as done in Sec. 4.1.2) or departing both winters to have results per winter. However, each filtering entailed the disadvantage of having too few data points to make a significant statement about correlations present.

6.2 Impact of Spatial Behaviour on C-Band Backscatter and Snow Parameter Correlations

Figure 6.1 includes backscatter values retrieved from a 10 m × 10 m pixel covering the location of the snow pack measurement. However, this single value retrieval can be unreliable due to the influence of speckle and the snow profile measurement procedure, which impacts on the snow pack structure. Therefore, it is also interesting to examine the behaviour of correlation over space, i.e. by taking a certain neighbourhood around the measurement site into account. An average of all backscatter values in the linear domain can be used to aggregate the data. This is done in Figure 6.2 for $\sigma^{40}_{LR,VH}$, as it shows the highest correlations in Figure 6.1. Neighbours are defined as the amount of pixels in one dimension being next to the measurement location, thus 1 means an average over 9 pixels, 2 an average over 25 pixels, 3 an average over 49 pixels, and so on. Different snow parameters yield different correlation curves, but most of them seem to agree well on the spatial dependency. Important snow pack parameters like grain size or snow wetness have a slight peak for 2 or 3 neighbours. In metric units, averaging is performed over a 50 m × 50 m and 70 m × 70 m region, respectively. This increase in correlation may be either due to a reduction of speckle or the simplified snow parameter itself is acting on a different catchment area and should be considered when correlating backscatter with snow parameters.

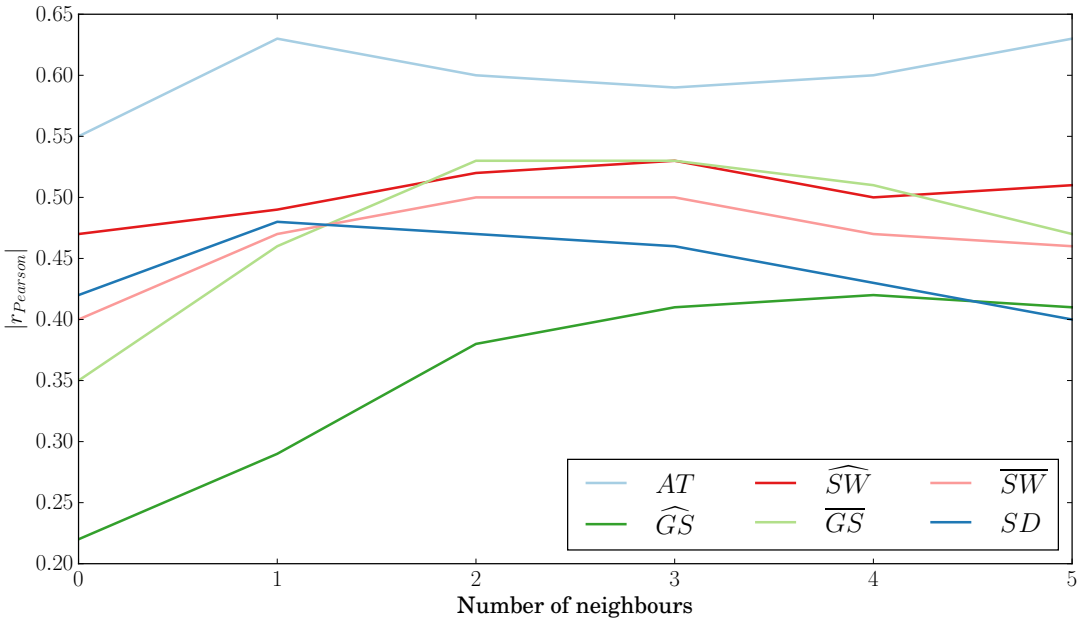

Figure 6.2: $r_{Pearson}$ in dependency on the neighbourhood (in pixel units) taken into account for averaging. Different curves are plotted for a subset of snow parameters.

6.3 Correlations between Cross-Polarisation Ratios and Snow Parameters

Relationships between C-Band backscatter and snow parameters can be also investigated by considering the polarimetric properties of backscatter in terms of the cross-polarisation ratio. Effects like terrain variations should cancel out, but a dependency on incidence angles persists, except when properly corrected by backscatter normalisation. $\overline{\sigma}^{40}_{PLPS}$ has a very weak correlation, whereas, interestingly, $\overline{\sigma}^{40}_{LR}$ performs well (cross-polarised backscatter is denoted as CR). Compared to Figure 6.1, correlations with respect to snow wetness are still present ($r_{Pearson} = -0.41$), but not as prevalent as before. In this evaluation, mean grain size is dominant with a negative correlation of -0.49. However, this is not in agreement with theoretic considerations. As grain sizes increase, volume scattering should become more important and therefore, due to multiple scattering, VH backscatter should increase too. Consequently, the ratio between VH and VV should increase with increasing grain sizes (i.e. a positive correlation is expected). A correlation seems to be present, even if it is negative, and will be studied in more detail in Sec. 6.5 with the aid of time series analysis. The slight positive correlation of snow height and the number of layers agrees with theory in terms of volume scattering, but its significance does not allow to draw any conclusions.

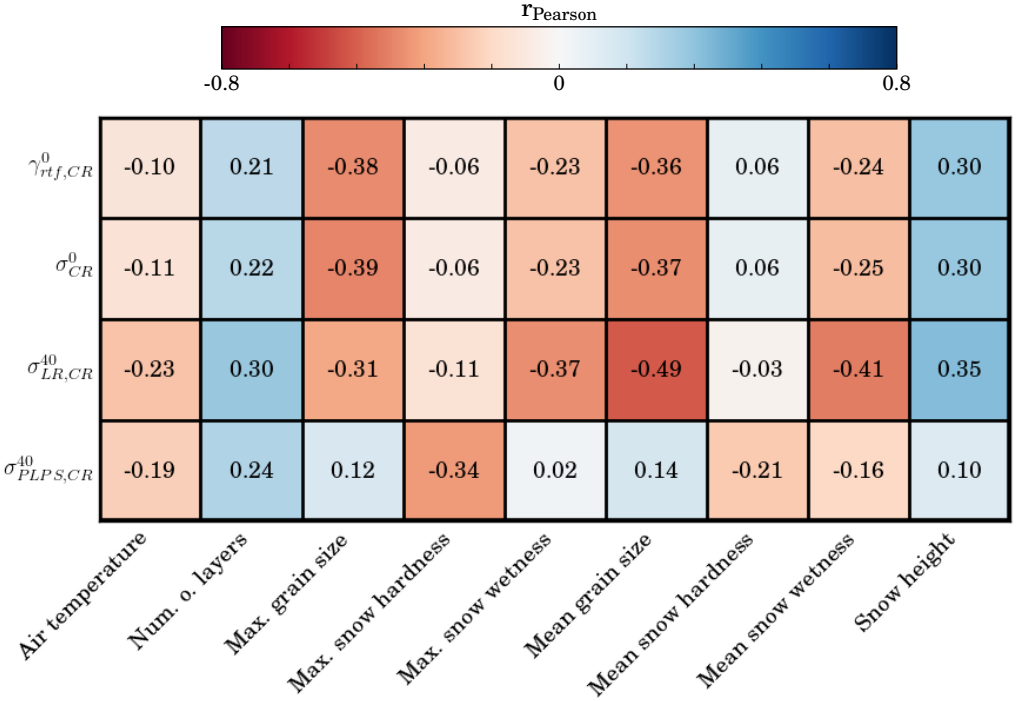

Figure 6.3: Correlations of cross-polarised backscatter data and various snow parameters expressed as $r_{Pearson}$ (three neighbours included).

6.4 Correlations between Backscatter Changes and Snow Parameters

Another approach to relate a backscatter value of a snow covered pixel to a reference backscatter value is known as change detection. This relation is expressed as a difference between the former and latter backscatter value (backscattering difference) and is denoted with $\tilde{\cdot}$ for a certain backscatter representation. Three different ways to define a reference image based on meteorological data have been presented in Section 5.1.3. In this section, their feasibility for the change detection method will be investigated. Similarly as for the previous sections, correlations are shown in a matrix (Fig. 6.4), where all plots contain $r_{Pearson}$ within a neighbourhood of three pixels.

As would be expected based on the earlier results, correlations increased significantly by ~ 0.2 (as shown in Figure 6.4 (a)) when taking three neighbours into account instead of none (Fig. 6.1). Figure 6.4 (c) shows the use of the *dryest* synthetic reference image and visually conveys the worst performance with highest correlations around -0.5. Attention is drawn to the fact that the usage of this criteria likely selects backscatter values not being available under the coldest conditions possible, since the pixel-wise focus is on minimum precipitation.

Compared to Figure 6.4 (a), correlations with air temperature diminish ($|r_{Pearson}| < 0.3$), but snow parameters such as maximum snow wetness ($r_{Pearson} = -0.64$), mean snow wetness ($r_{Pearson} = -0.6$) or mean grain size ($r_{Pearson} = -0.54$) become more concise. Snow height has a high positive $r_{Pearson}$ of 0.67 in Figure 6.4 (d), which can be explained to some extent by recognising that the therein used reference image is likely the only snow-free image. Thus, the backscattering difference may yield a larger sensitivity towards snow height, but this is more thought of being a spurious correlation. Maximum snow wetness has a larger negative correlation of around -0.64 and even lower being present in all figures. In addition, the difference formation causes terrain and surface variations to become less of an issue. Hence, all backscatter representations with respect to maximum snow wetness lead to a correlation in the same order of magnitude, being most concisely visible in Figure 6.4 (b). Because of this, the simpler construction of the synthetic reference image and the best negative correlation, the *coldest* synthetic reference image in VH polarisation is thought to be the most appropriate one to detect wet snow.

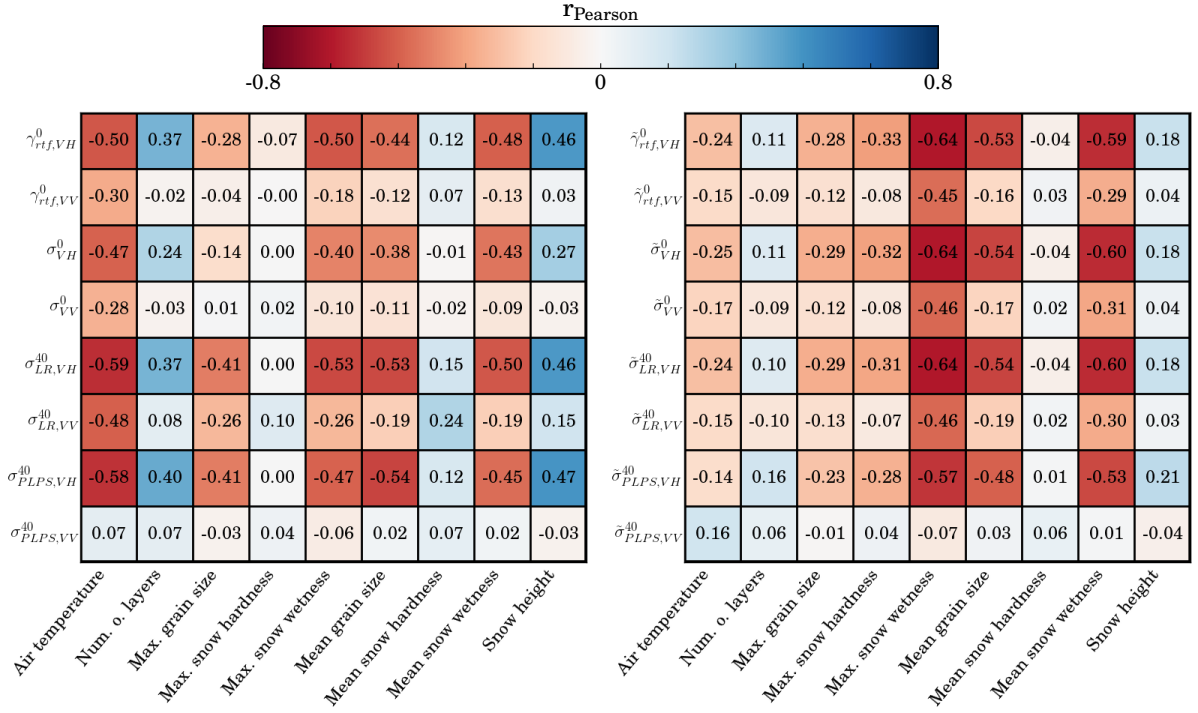

(a) $r_{Pearson}$ as in Fig. 6.1, but considering three neighbours instead of none.

(b) $r_{Pearson}$ for backscattering differences using the *coldest* reference image.

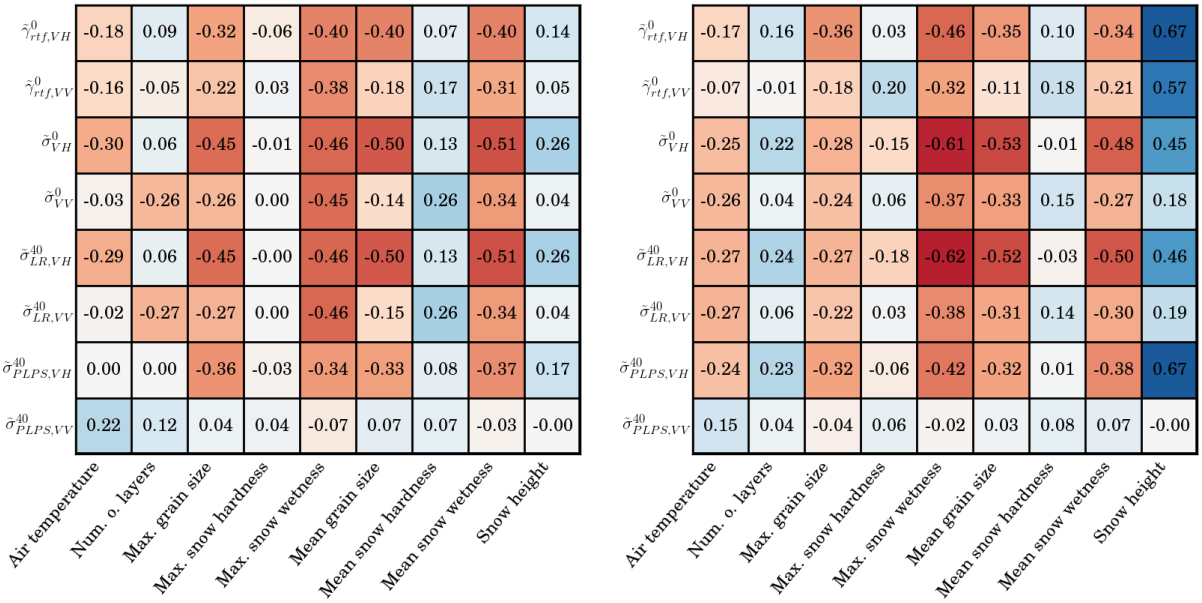

(c) $r_{Pearson}$ for backscattering differences using the *dryest* synthetic reference image.

(d) $r_{Pearson}$ for backscattering differences using the *hottest* synthetic reference image.

Figure 6.4: Correlation matrices containing $r_{Pearson}$ for each backscattering difference and snow parameter combination, except (a), which focuses on backscattering coefficients. All $r_{Pearson}$ are based on three neighbours. For each method, only the best result fulfilling the specific criteria was taken as a synthetic reference image.

This last insight can further be used to map these backscattering differences along with the other gathered findings. Figure 6.5 provides a view of backscattering differences $\tilde{\sigma}^0_{VH}$, the most simple representation of backscatter. Values above zero were masked.

Just depicting differences below zero without any spatial filtering results in a noisy image (Fig. 6.5 (c)). Results improve as one applies spatial filtering (Fig. 6.5 (b), two neighbours) and both, spatial and temporal averaging (Fig. 6.5 (a), two neighbours, two best reference image results). Figure 6.5 (d), showing $\tilde{\sigma}^0_{VH}$ based on the *hottest* synthetic reference image, also conveys a nice impression but tends to be noisier in none snow covered areas. Maps indicating wet snow were also created with an averaging based on three neighbours, as it showed good statistics before, but it turned out to be too coarse and too much information is lost. Figure 6.5 (a) shows the distinctiveness of $\tilde{\sigma}^0_{VH}$ at most, thus this configuration is stated to be the most promising for mapping wet snow.

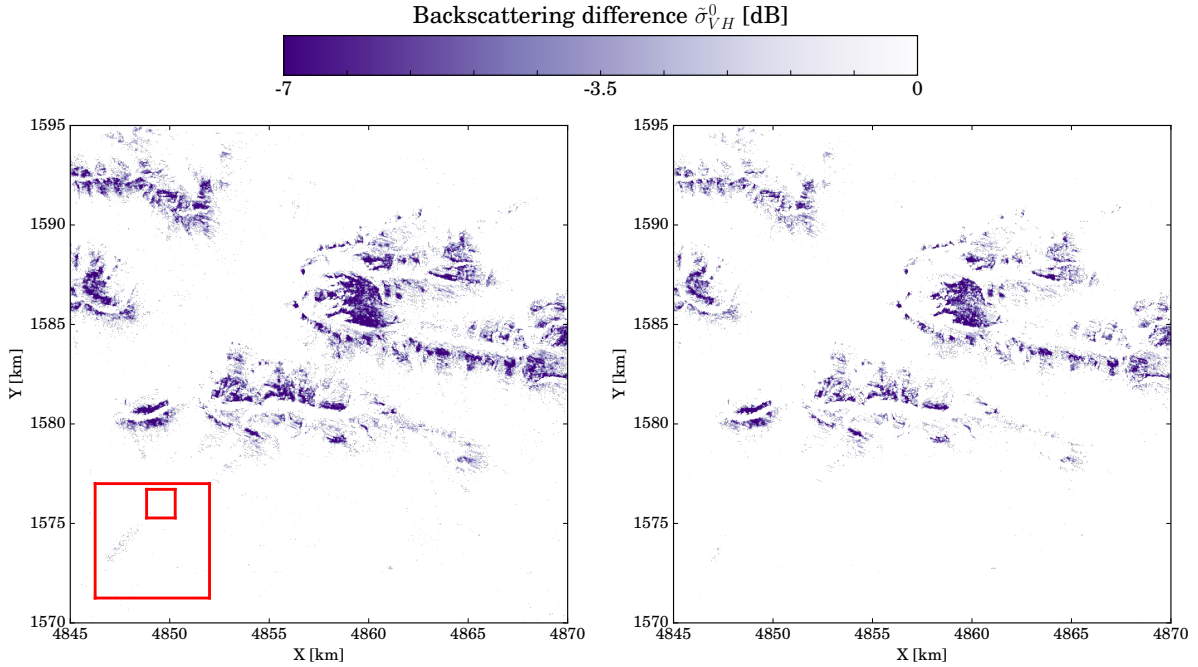

(a) *Coldest* synthetic reference image (two neighbours in time and space).

(b) *Coldest* synthetic reference image (two neighbours).

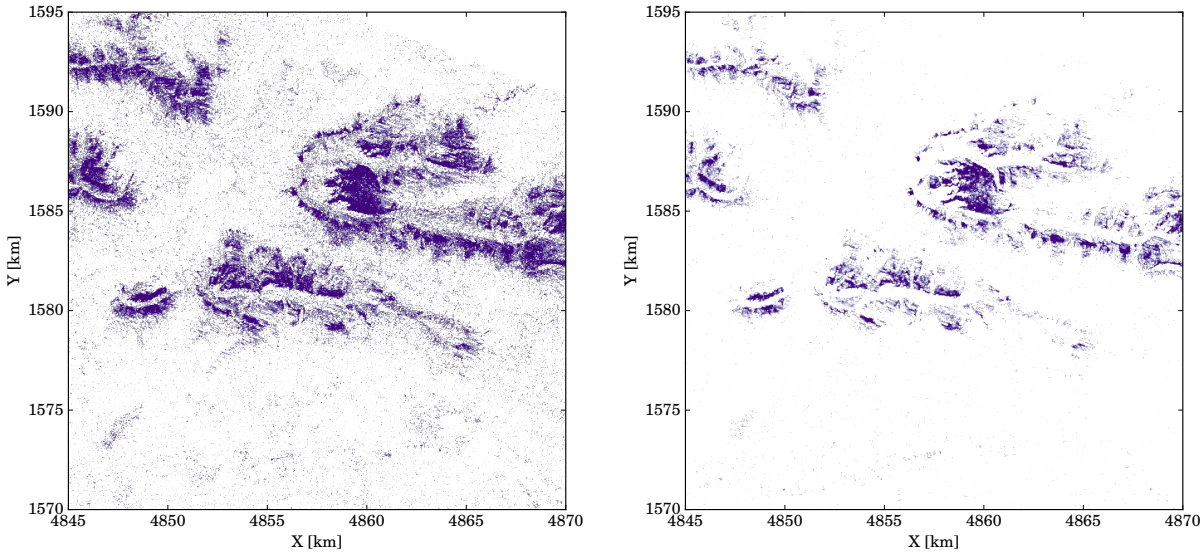

(c) *Coldest* synthetic reference image.

(d) *Hottest* synthetic reference image (two neighbours).

Figure 6.5: Backscattering differences for $\tilde{\sigma}^0_{VH}$, different reference images and filtering methods covering the region around the *"Zugspitze"*. All $\tilde{\sigma}^0_{VH}$ values above zero are masked. The spatial extent of the depicted region is shown in (a). The red outer box represents the boundaries of the Equi7 tile *"E048N015T1"* and the red inner box depicts the extent shown in the figures above.

6.5 Snow Parameter and C-Band SAR Backscatter Time Series Comparison

Further insights can be gained by undertaking a time series analysis of snow and C-band SAR backscatter parameters over time as shown in Figure 6.6. Having a closer look at the top time series, less influence by terrain is evident for the normalised backscatter versions, which line up very well, and for γ^0_{rtf}. Although, there is a profound negative correlation, air temperature could influence the snow pack on a different temporal scale than for instance snow wetness (cf. Fig. 6.6 (bottom)).

Snow height and mean grain size are compared to all cross-polarisation ratios in Figure 6.6 (center). Here, two snow parameters are chosen for comparison, because both are necessary to explain their impact on polarised backscatter (cf. Sec. 6.3). After difference formation the effect of terrain seems to be largely eliminated for all backscatter curves, whereas a slight impact of land cover seems to persist for unnormalised products, since there is a clear gap between both representations, i.e. normalised and not normalised. However, this gap could be also a sign of not being able to fully account for the incidence angle dependency when applying both normalisation methods. With the aid of maximum snow wetness in Figure 6.6 (bottom) it can be seen that major drops (around the March 27$^{\text{th}}$, 2017 and April 30$^{\text{th}}$, 2017) of the cross-polarisation ratio are caused by wet snow. VH polarisation is more affected by wet snow than VV, therefore leading to a decrease in the cross-polarisation ratio (cf. Fig. D.1). As already stated, the negative correlation of grain sizes with backscatter disagrees with theory and could be due to snow height, snow wetness and grain size interactions. Starting in January 2017, snow height increases up to 1 m, which tends to also lead to an increase of the cross-polarisation ratio. The first drop of the ratio at the beginning of February 2017 could be caused by snowmelt. Even if the snow pack was classified as dry, the backscattering difference curves support this statement. Afterwards, a steady phase of snow heights and grain sizes is present, but yet the aging of the snow pack could be responsible for the slight, continuous increase in the ratio. Subsequently, both aforementioned snow melt events and the time series concludes with a recognisable rise of the cross-polarisation ratio. It is close to zero (in dB), meaning VH is nearly as large as VV backscatter, which is likely to be caused by snow heights above 2 m or single layers of large grains retaining the influence of the snowmelt period before.

Finally, Figure 6.6 (bottom) relates maximum snow wetness to backscattering differences, where satellite and snow profile measurements correspond very well except on January 20$^{\text{th}}$, 2017. A snow pack was classified as wet, not being obviously detected by the backscattering difference (error of omission). In the case of backscattering differences, $\tilde{\sigma}^{40}_{PLPS,VH}$ includes one outlier shortly before March 27$^{\text{th}}$, 2017 and does not align well with the other backscatter curves.

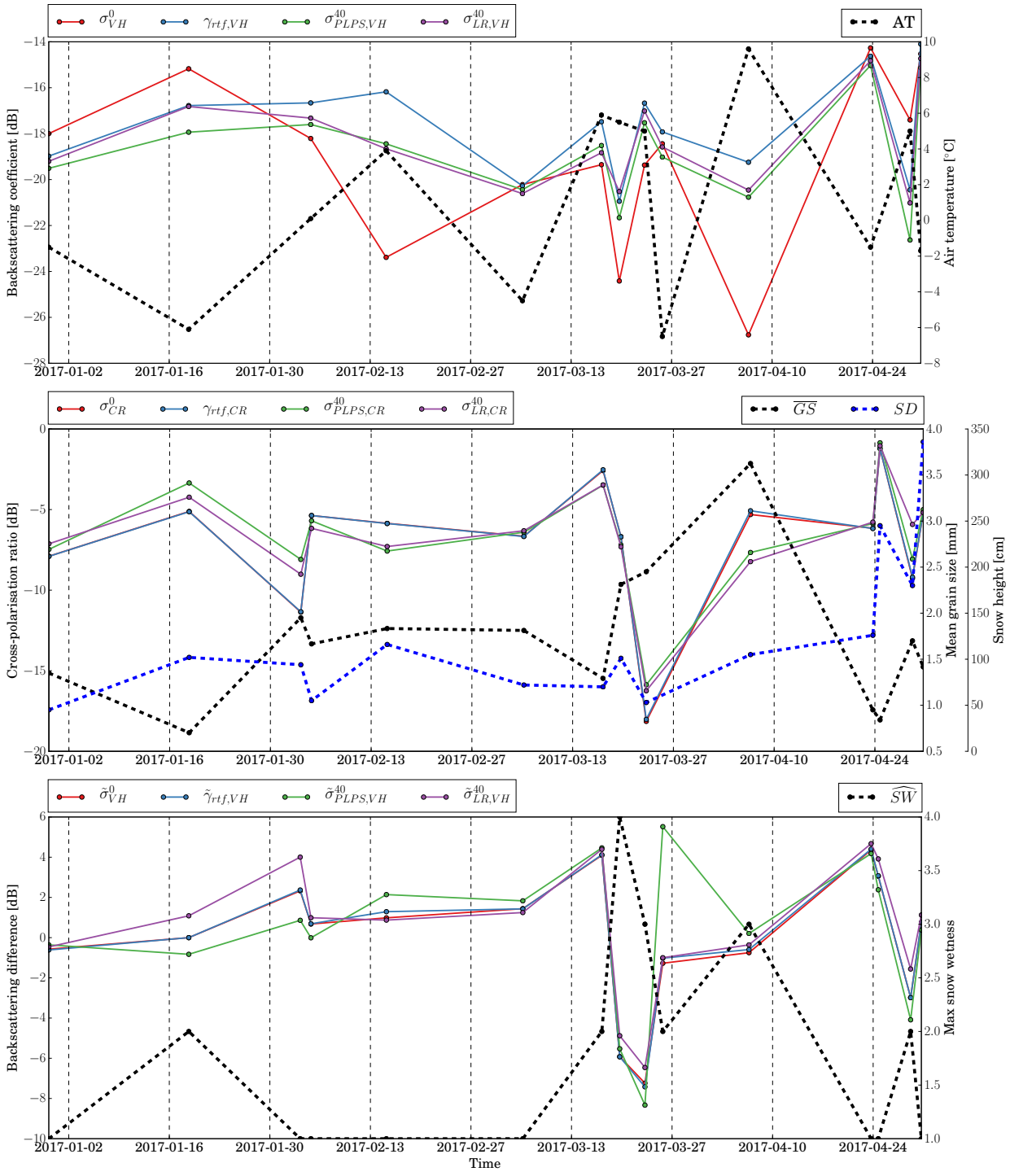

Figure 6.6: Time series for all backscattering coefficients at VH polarisation (top), cross-polarisation ratios (center) and backscattering differences at VH polarisation by using the "coldest" synthetic reference image (bottom) (including three neighbours). Following the same order, AT, SD together with $\overline{GS}$, and $\widehat{SW}$ are plotted in relation to the backscatter curves.

6.6 Comparison to Optical Imagery

The discussed enhancements for mapping snow parameters can further be used to relate these results to an optical image enabling a detection of similar and dissimilar parts, respectively. Optical imagery serving as a reference was offered by the Operational Land Imager (OLI) sensor onboard of Landsat 8. Figure 6.7 (a) depicts backscattering differences of $\tilde{\gamma}^0_{rtf,VH}$ with respect to the *hottest* synthetic reference image. The S-1 acquisition took place on January 10$^{\text{th}}$, 2017, thus backscatter was sensed in a period of very low temperatures (cf. Sec. 3.1.2). Two phenomena are evident, when having a closer look at $\tilde{\gamma}^0_{rtf,VH}$: First, low $\tilde{\gamma}^0_{rtf,VH}$ values in the valleys could be a sign of wet snow or could be linked to the absence of vegetation in the backscatter image on January 10$^{\text{th}}$, 2017. Second, positive $\tilde{\gamma}^0_{rtf,VH}$ values seem to be likely caused by the presence of snow above the timber line. In these mountainous areas, vegetation becomes less of an issue. It has to be noted, that the temporal separation between the RGB composite and the backscatter image is not optimal, since snowfall could have happened in between the acquisitions.

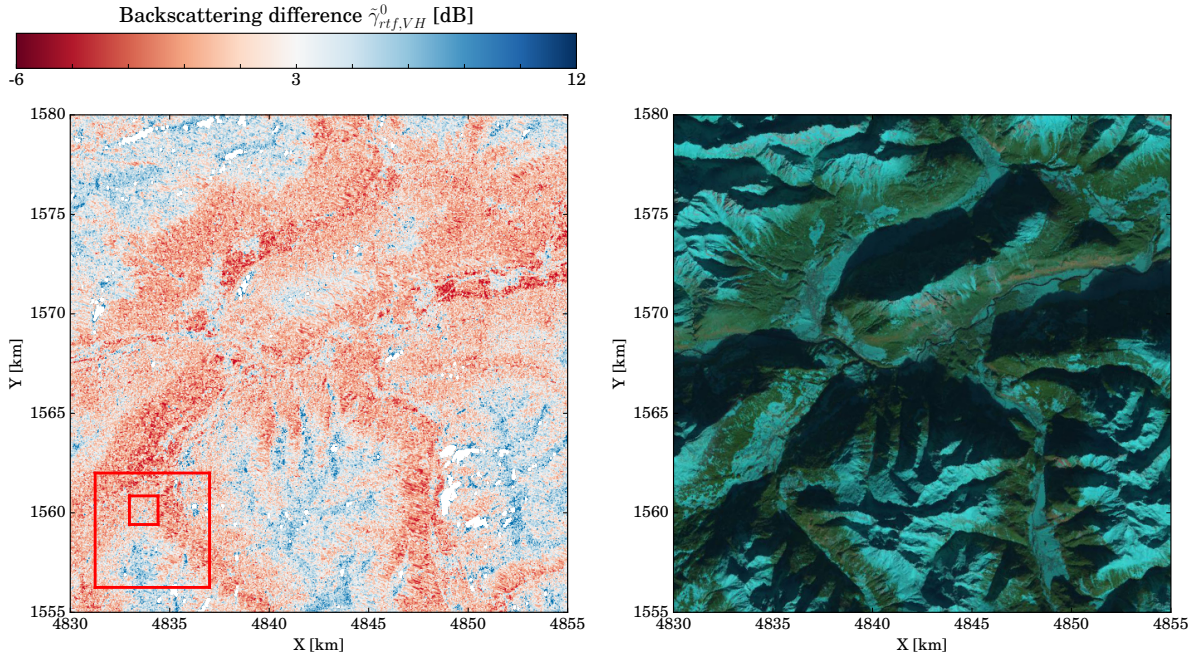

(a) Filtered (two neighbours) backscattering difference $\tilde{\gamma}^0_{rtf,VH}$ derived from the *hottest* reference images (January 10$^{\text{th}}$, 2017).

(b) Landsat 8 image (January 25$^{\text{th}}$, 2017).

Figure 6.7: Comparison of $\tilde{\gamma}^0_{rtf,VH}$ with a Landsat 8 OLI false colour image[1]. The RGB composite consists of the SWIR-band (R), NIR-band (G) and Red-band (B). The spatial extent of the depicted region is shown in (a). The red outer box represents the boundaries of the Equi7 tile *"E048N015T1"* and the red inner box depicts the extent shown in the figures above.

In Figure 6.8 (a), backscattering differences are shown in the same way as in Figure 6.5 (a). This map is an indication or estimate of wet snow, given by the backscattering difference. The area covered by the map shows the major glaciers *"Gepatschferner"* and *"Hintereisferner"*, and parts of the *"Kaunertal"*, *"Pitztal"* and *"Ötztal"* valley. The snow-covered areas in Figure 6.8 (c) show a good agreement with snow melt areas, whereas backscattering differences vary significantly within such an area. A few isolated snow fields can be also detected with some misclassified pixels containing a lower $\tilde{\sigma}^0_{VH}$ as a trade-off. Furthermore, the backscattering difference image offers a very nice delineation of glacier snouts and the separation of south- and north-facing slopes.

Figure 6.8 (b) depicts cross-polarisation ratios for normalised backscatter $\sigma^{40}_{LR,CR}$. In comparison to Figure 6.8 (d), the highest elevated areas are visible as positive $\sigma^{40}_{LR,CR}$ values (neglecting the large temporal separation of both acquisitions) probably being caused by multiple scattering inside the snow pack. The dark red areas on south-facing slopes could indicate the presence of liquid water inside the snow pack, since the difference between VH and VV increases for wet snow (cf. Appendix D).

Both maps (Fig. 6.7 (b) and Fig. 6.8 (a)) indicate the feasibility of mapping dry snow (and wet snow). However, by just taking the cross-polarisation ratios or backscattering differences without any guidance of a physical model into account, it is not possible to quantitatively derive a dry snow parameter, e.g. snow height or grain size.

[1]data source: U.S. Geological Survey, accessed on November 20^{th}, 2018
[2]data source: U.S. Geological Survey, accessed on November 20^{th}, 2018

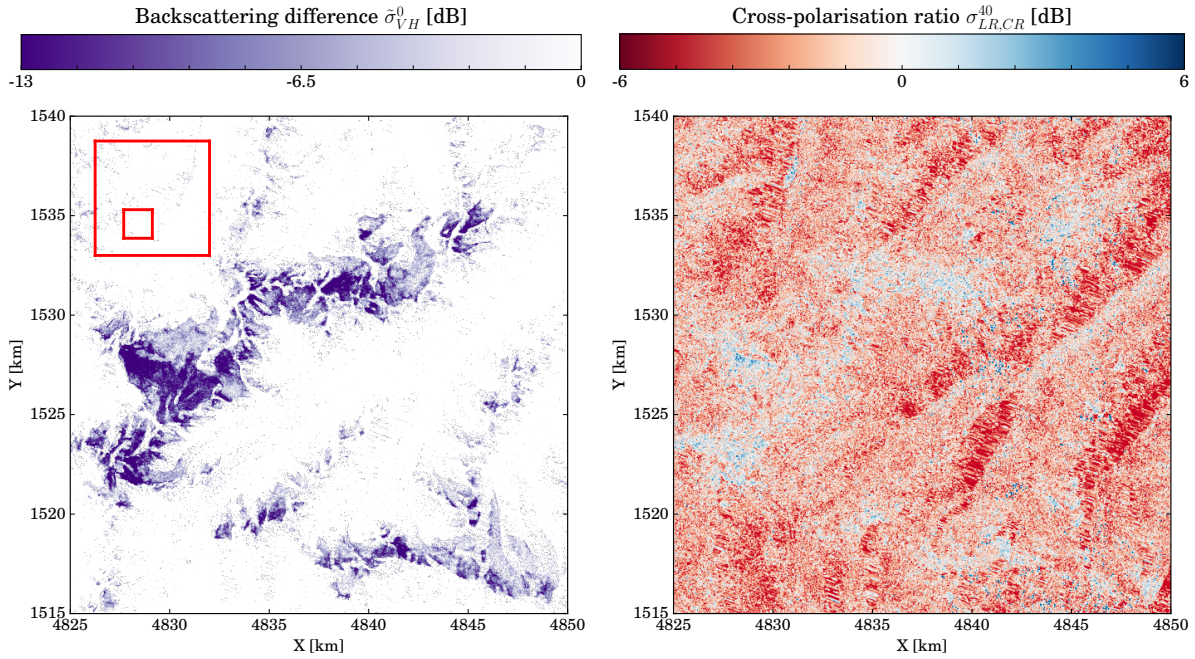

(a) Filtered (two neighbours) backscattering difference $\tilde{\sigma}^0_{VH}$ derived from the merged, *cold-est* reference images (June 18$^{\text{th}}$, 2017).

(b) Filtered (two neighbours) cross-polarisation ratio $\sigma^{40}_{LR,CR}$ (January 10$^{\text{th}}$, 2017).

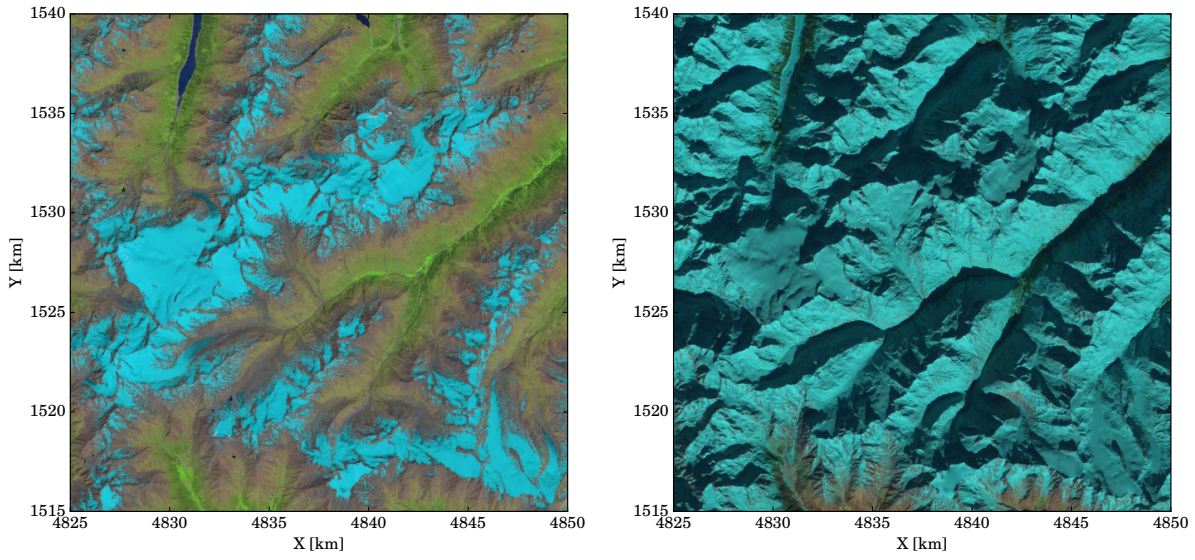

(c) Landsat 8 image (June 18$^{\text{th}}$, 2017).

(d) Landsat 8 image (January 25$^{\text{th}}$, 2017).

Figure 6.8: Comparison of $\tilde{\sigma}^0_{VH}$ and $\sigma^{40}_{LR,CR}$ with Landsat 8 OLI false colour images[2]. The RGB composite consists of the SWIR-band (R), NIR-band (G) and Red-band (B). The area covers glaciers and the highest peaks in the chosen region of interest (e.g. *"Wildspitze"*). The spatial extent of the depicted region is shown in (a). The red outer box represents the boundaries of the Equi7 tile *"E048N015T1"* and the red inner box depicts the extent shown in the figures above.

Chapter 7

Summary and Conclusion

In this thesis, a study was performed to identify interdependencies between various snow parameters and C-band SAR backscatter observations from Sentinel-1. To achieve this aim, backscatter was modified by means of radiometric normalisation, incidence angle normalisation, change detection or cross-polarisation ratios. Insights gained from correlating these backscatter representations with snow measurements should then indicate the feasibility of monitoring alpine snow conditions with C-band SAR.

All datasets were acquired for two winter seasons, 2015/2016 and 2016/2017, within the geographic scope of the North and South Tyrolean Alps. In-situ snow profile data was only available as graphics and had to be digitised semi-automatically. An investigation of relationships between different snow parameters revealed the impact of snow metamorphism and temperature on grain sizes and grain types. Moreover, it was found that moist or wet snow is mainly located in the lower and upper part of the snow pack and that the largest grains occur when depth hoar is present.

A sensitivity analysis employing theoretical models has shown what influence from snow pack characteristics on backscatter can be expected at C-band. Here, this was done in a simplistic way, only using a first-order RT model and not including any higher-order scattering effects. The herein presented model neglects important parts such as coherent scattering in a dense media, snow stratification and even surface scattering at the air-snow interface. This means, the scatter plots in Figure 4.3 likely underestimate the possible range of values for volume backscatter. Moreover, other studies have drawn attention to the difficulty of properly defining a stickiness value for a given snow profile. When increasing the snow stickiness, the possible range of volume backscatter values can range from 0 dB to 5 dB, however, at an expense of a lower model accuracy as the scattering coefficient κ_s increases too. The necessity to take coherent scattering due to larger grains and snow heights into account, was justified by Figure 6.6 (center). Nevertheless, within the set of the chosen fixed parameters and all snow profile measurements, grain size is correlated to C-band backscatter at most in theory.

Among all snow parameters, snow hardness has the least correlation of around 0.1 on average, possibly due to the way it was measured. Snow height and the number of layers correlate positively with backscatter, which is plausible, but unrealistic to be the sole cause for backscatter variations at a scale of 5-10 dB ($r_{Pearson} = 0.67$). Yet, the time series analysis of cross-polarisation ratios and the comparison with optical imagery seem to support the influence of snow depth and grain size. Most correlation plots imply that snow wetness is the most promising snow parameter in terms of negative linear behaviour with backscatter ($r_{Pearson} = -0.64$). This is emphasised by the time series relating maximum snow wetness to backscattering differences (cf. Fig. 6.6). Correlations with grain sizes seem to perform nearly as good as snow wetness, but a negative correlation of the observed order contradicts theoretical considerations ($r_{Pearson} = -0.53$). Again, time series and also snow parameter analysis shed light on this, namely that larger grains occur more often if the snow layer is wet (or after multiple melt-freeze cycles). An exterior parameter impacting on the snow pack is air temperature having a negative correlation ($r_{Pearson} = -0.59$) with backscatter, since snow wetness is mainly driven by a change in temperature. All snow parameters experienced a larger correlation with VH than with VV polarised backscatter, underlining the fact that VH polarised backscatter is influenced by multiple scattering, thus containing more information about the penetrated volume. However, one has to be aware of not trying to retrieve information from VH polarised backscatter when close to the noise level.

σ^0 backscatter was transformed to a normalised version at $\theta_{ref} = 40\,^\circ$ by using linear regression and a novel methodology, the Piecewise Linear Percentile Slope (PLPS) normalisation. This method makes use of the orbit-wise backscatter distribution for scaling the distribution at θ_{ref} in relation to its neighbouring orbits. According to an intercomparison, terrain effects seem to be corrected more adequately if linear regression is applied, as it ought to be more robust concerning critical backscatter distributions at high and low incidence angles. Yet, the PLPS method is superior if more orbits covering a broad range of incidence angles are involved. In areas where only two orbits are available and both are close together in terms of θ, both methods will fail (cf. Fig. B.2 in Appendix). γ^0_{rtf} revealed striking impressions for a different way to represent backscatter and correct it in areas affected by layover with a rigorous approach. Still, the incidence angle dependency regarding specific land cover types is not solved, thus diminishing the comparability of snow parameter measurements at different sites. This was justified by most correlation results, where normalised products have shown to better match snow parameters over time, especially σ^{40}_{LR}.

Additional advancements for selecting a reliable reference image for change detection were introduced on a pixel-level, with the aid of meteorological data. Three criteria were suggested, namely minimum temperature per pixel (*coldest* synthetic reference image),

minimum precipiation per pixel and overall minimum temperature (*dryest* synthetic reference image), and maximum temperature per pixel and overall minimum precipitation (*hottest* synthetic reference image). The first one was found to be the best in terms of wet snow mapping, shortly followed by the third one, which also revealed promising results for mapping dry snow. Spatial and temporal (low-pass) filtering using two or three neighbours in time and space, i.e. selecting more than one synthetic reference image and averaging over 25 or 49 pixels, limits disturbing effects (e.g. speckle) to a certain extent and also leads to a meaningful enhancement of image and perhaps parameter retrieval quality.

To conlude, results suggest there are interdependencies between snow parameters and C-band SAR backscatter, even if the (linear) correlation is not that high. C-band SAR backscatter from snow covered areas offers mainly information about water deposits and wet snow inside a snow pack. Therefore, compared to other snow parameters, maximum snow wetness has a superior, profound correlation with backscattering differences, which agrees with other studies (e.g., Nagler and Rott (2000), Nagler, Rott, et al. (2016), and Magagi and Bernier (2003)). The less significant correlation with mean snow wetness implies that one layer being only weakly moist or moist can already be detected with C-band SAR. With a focus on wet snow mapping by using change detection, σ^0 seems to be sufficient, with the benefit of less computational effort than for instance γ^0_{rtf}. The difference formation entails the advantage of eliminating the need to select a specific backscatter representation, because effects varying with location, i.e. land cover and terrain, cancel out. An incidence angle mask as proposed in Nagler and Rott (2000) is necessary for σ^0, whereas γ^0_{rtf} corrects or masks areas affected by layover or shadow. Consequently, if one has the capacities to apply radiometric terrain flattening on SAR data, γ^0_{rtf} should be the preferred way of wet snow mapping.

Even in the absence of liquid water inside a snow pack, C-band SAR backscatter can provide insights to delineate the extent of dry snow. This becomes evident when using change detection by means of the *hottest* reference image (cf. Fig. 6.8 (b)). However, it is not possible to distinguish the parameters acting on backscatter (e.g. surface, snow height, grain size) by only taking C-band SAR backscatter data without any auxiliary data or physical models into account (e.g., Shi and Dozier, 2000a; Shi and Dozier, 2000b).

Chapter 8

Outlook

Naturally, this work opens up further research questions and possibilities as set out below.

Azimuthal effects (e.g. due to ascending and descending orbits) have been neglected within the frame of this thesis, but cause recognisable variations in backscatter, in particular having an impact on backscatter normalisation. The PLPS backscatter normalisation method has shown promising results in areas covered by four orbits and is worth to be analysed in terms of other applications, for instance soil moisture retrieval in agricultural areas. However, without having any further backscatter data to supply a reliable normalisation, the aforementioned problems regarding the constellation of the orbits will remain.

In-situ data quality is still to be questioned, as some snow parameters, e.g. snow hardness and snow wetness, may be biased depending on the surveyor. Results might be tuned, if snow density and snow liquid water content are measured instead. This would also offer the opportunity to investigate essential snow parameters like SWE. An optimal measurement setup would include frequent acquisitions at the same sites, without destroying the structure of the snow pack. Whilst demanding to undertake in practice, gathering more data points by expanding the region of interest in space and time could also help to underline the significance of certain correlations or shed light onto relations between different snow parameters and remote sensing data.

Map quality could be further enhanced by not only merging the top two synthetic reference image results, but taking more images into account to see if speckle in the reference image becomes less of an issue. If one wants to focus on areas of lower elevation too, the coldest synthetic reference image will be the wrong choice, whereas the one at hottest conditions seems to be more appropriate. Yet, one has to deal with the influence of vegetation in agricultural areas, e.g. preferring an image sensed in autumn after harvest.

Finally, the approach to map wet snow presented herein makes use of all backscattering differences below zero and replaces the necessity to define an arbitrary threshold with spatial and temporal filtering. Such a threshold, commonly being chosen as $-2\,\mathrm{dB}$ or $-3\,\mathrm{dB}$ has been discussed in many works (Nagler and Rott, 2000; Nagler, Rott, et al., 2016; Longepe et al., 2009; Navacchi, 2016). Moreover, the presented maps most likely indicating the dry snow extent need to be revised in terms of finding an appropriate criteria or threshold for separating snow covered from snow-free areas. As a final statement, it would be interesting to use such maps by means of climate change analysis. Four years of Sentinel-1 data in cooperation with an increasing amount of snow profile measurements could for instance assist snow cover, run-off or even glacier retreat analysis.

Bibliography

SAR and/or C-Band Radar

Baghdadi, Nicolas et al. (2017). "Calibration of the water cloud model at C-Band for winter crop fields and grasslands". In: *Remote Sensing* 9.9, p. 969.

Baghdadi, N et al. (2001). "Evaluation of C-band SAR data for wetlands mapping". In: *International Journal of Remote Sensing* 22.1, pp. 71–88.

Bauer-Marschallinger, Bernhard, Vahid Freeman, et al. (2018). "Toward Global Soil Moisture Monitoring With Sentinel-1: Harnessing Assets and Overcoming Obstacles". In: *IEEE Transactions on Geoscience and Remote Sensing* 99, pp. 1–20.

De Zan, Francesco and AM Monti Guarnieri (2006). "TOPSAR: Terrain observation by progressive scans". In: *IEEE Transactions on Geoscience and Remote Sensing* 44.9, pp. 2352–2360.

European Space Agency (2018). *Sentinel-1 User Guides*. URL: https://sentinel.esa.int/web/sentinel/user-guides/sentinel-1-sar/ (visited on 08/11/2018).

Frey, Othmar et al. (2013). "DEM-based SAR pixel-area estimation for enhanced geocoding refinement and radiometric normalization". In: *IEEE Geoscience and Remote Sensing Letters* 10.1, pp. 48–52.

Moen, M-AN et al. (2015). "Assessing polarimetric SAR sea-ice classifications using consecutive day images". In: *Annals of Glaciology* 56.69, pp. 285–294.

Naeimi, Vahid, Stefano Elefante, et al. (2016). "Geophysical parameters retrieval from sentinel-1 SAR data: a case study for high performance computing at EODC". In: *Proceedings of the 24th High Performance Computing Symposium*. Society for Computer Simulation International, p. 10.

Najoui, Zhour et al. (2018). "A Statistical Approach to Preprocess and Enhance C-Band SAR Images in Order to Detect Automatically Marine Oil Slicks". In: *IEEE Transactions on Geoscience and Remote Sensing* 56.5, pp. 2554–2564.

Park, Jeong-Won et al. (2018). "Efficient thermal noise removal for Sentinel-1 TOPSAR cross-polarization channel". In: *IEEE Transactions on Geoscience and Remote Sensing* 56.3, pp. 1555–1565.

Sabel, Daniel et al. (2010). "A global backscatter model for C-band SAR". In: *Proceedings of the ESA Living Planet Symposium, Bergen, Norway*. Vol. 28.

Shimada, Masanobu (2005). "Long-term stability of L-band normalized radar cross section of Amazon rainforest using the JERS-1 SAR". In: *Canadian Journal of Remote Sensing* 31.1, pp. 132–137.

Small, David (2011). "Flattening gamma: Radiometric terrain correction for SAR imagery". In: *IEEE Transactions on Geoscience and Remote Sensing* 49.8, pp. 3081–3093.

Twele, André et al. (2016). "Sentinel-1-based flood mapping: a fully automated processing chain". In: *International Journal of Remote Sensing* 37.13, pp. 2990–3004.

Wiley, Carl A (1985). "Synthetic aperture radars". In: *IEEE Transactions on Aerospace and Electronic Systems* 3, pp. 440–443.

Snow Pack Characteristics

Giddings, John Calvin and E LaChapelle (1962). "The formation rate of depth hoar". In: *Journal of Geophysical Research* 67.6, pp. 2377–2383.

Jamieson, Bruce (2006). "Formation of refrozen snowpack layers and their role in slab avalanche release". In: *Reviews of Geophysics* 44.2.

Singh, P et al. (1997). "Hydrological response of snowpack under rain-on-snow events: a field study". In: *Journal of Hydrology* 202.1-4, pp. 1–20.

Sommerfeld, RA and E LaChapelle (1970). "The classification of snow metamorphism". In: *Journal of Glaciology* 9.55, pp. 3–18.

Snow Parameter Retrieval

Arslan, Ali Nadir et al. (1999). "An empirical model for retrieving water equivalent of dry snow from C-band SAR data". In: *Geoscience and Remote Sensing Symposium, 1999. IGARSS'99 Proceedings. IEEE 1999 International*. Vol. 3. IEEE, pp. 1789–1791.

Bernier, M and J-P Fortin (1998). "The potential of times series of C-band SAR data to monitor dry and shallow snow cover". In: *IEEE Transactions on Geoscience and Remote Sensing* 36.1, pp. 226–243.

De Lannoy, Gabriëlle et al. (2018). "Snow Estimation Under a Vegetation Gradient using Satellite Remote Sensing Data and Land Surface Modeling During Snowex 2017". In: *IGARSS 2018-2018 IEEE International Geoscience and Remote Sensing Symposium*. IEEE, pp. 6294–6297.

Koskinen, Jarkko T, Jouni T Pulliainen, and Martti T Hallikainen (1997). "The use of ERS-1 SAR data in snow melt monitoring". In: *IEEE Transactions on geoscience and remote sensing* 35.3, pp. 601–610.

Longepe, Nicolas et al. (2009). "Snowpack characterization in mountainous regions using C-band SAR data and a meteorological model". In: *IEEE Transactions on Geoscience and Remote Sensing* 47.2, pp. 406–418.

Magagi, R and M Bernier (2003). "Optimal conditions for wet snow detection using RADARSAT SAR data". In: *Remote Sensing of Environment* 84.2, pp. 221–233.

Nagler, Thomas and Helmut Rott (2000). "Retrieval of wet snow by means of multitemporal SAR data". In: *IEEE Transactions on Geoscience and Remote Sensing* 38.2, pp. 754–765.

Nagler, Thomas, Helmut Rott, et al. (2016). "Advancements for snowmelt monitoring by means of sentinel-1 SAR". In: *Remote Sensing* 8.4, p. 348.

Navacchi, Claudio (2016). "Snowmelt Monitoring with Sentinel-1". Bachelor's Thesis. TU Wien.

Shi, Jiancheng and Jeff Dozier (1995). "Inferring snow wetness using C-band data from SIR-C's polarimetric synthetic aperture radar". In: *IEEE transactions on geoscience and remote sensing* 33.4, pp. 905–914.

— (2000a). "Estimation of snow water equivalence using SIR-C/X-SAR. I. Inferring snow density and subsurface properties". In: *IEEE Transactions on Geoscience and Remote Sensing* 38.6, pp. 2465–2474.

— (2000b). "Estimation of snow water equivalence using SIR-C/X-SAR. II. Inferring snow depth and particle size". In: *IEEE Transactions on Geoscience and Remote sensing* 38.6, pp. 2475–2488.

Shi, Jiancheng, Jeff Dozier, and Helmut Rott (1993). "Deriving snow liquid water content using C-band polarimetric SAR". In: *Geoscience and Remote Sensing Symposium, 1993. IGARSS'93. Better Understanding of Earth Environment., International*. IEEE, pp. 1038–1041.

— (1994). "Snow mapping in alpine regions with synthetic aperture radar". In: *IEEE Transactions on Geoscience and Remote Sensing* 32.1, pp. 152–158.

Radiative Transfer Theory

Du, Jinyang, Jiancheng Shi, and Helmut Rott (2010). "Comparison between a multi-scattering and multi-layer snow scattering model and its parameterized snow backscattering model". In: *Remote Sensing of Environment* 114.5, pp. 1089–1098.

Fung, A and Hyo Eom (1981). "A theory of wave scattering from an inhomogeneous layer with an irregular interface". In: *IEEE Transactions on Antennas and Propagation* 29.6, pp. 899–910.

Picard, Ghislain, Ludovic Brucker, et al. (2012). "Simulation of the microwave emission of multi-layered snowpacks using the dense media radiative transfer theory: the DMRT-ML model". In: *Geosci. Model Dev. Discuss* 5, pp. 3647–3694.

Picard, Ghislain, Melody Sandells, and Henning Löwe (2018). "SMRT: an active–passive microwave radiative transfer model for snow with multiple microstructure and

scattering formulations (v1.0)". In: *Geoscientific Model Development* 11.7, pp. 2763–2788.
Quast, Raphael and Wolfgang Wagner (2016). "Analytical solution for first-order scattering in bistatic radiative transfer interaction problems of layered media". In: *Applied optics* 55.20, pp. 5379–5386.
Rybicki, George B and Alan P Lightman (2008). *Radiative processes in astrophysics*. John Wiley & Sons.
Shih, S-E et al. (1997). "Modeling of millimeter wave backscatter of time-varying snowcover". In: *Progress In Electromagnetics Research* 16, pp. 305–330.
Smith, William L (1970). "Iterative solution of the radiative transfer equation for the temperature and absorbing gas profile of an atmosphere". In: *Applied Optics* 9.9, pp. 1993–1999.
Tsang, Leung, KH Ding, and B Wen (1992). "Dense media radiative transfer theory for dense discrete random media with particles of multiple sizes and permittivities". In: *Progress in Electromagnetic Research* 6.5, pp. 181–225.
Tsang, Leung and Jin Au Kong (2004). *Scattering of electromagnetic waves: advanced topics*. Vol. 26. John Wiley & Sons.
Tsang, Leung, Jin Au Kong, et al. (2004). *Scattering of electromagnetic waves: numerical simulations*. Vol. 25. John Wiley & Sons.

Miscellaneous

Bauer-Marschallinger, Bernhard, Daniel Sabel, and Wolfgang Wagner (2014). "Optimisation of global grids for high-resolution remote sensing data". In: *Computers & Geosciences* 72, pp. 84–93.
Canadian Space Agency (2018). *RADARSAT Constellation Mission*. URL: http://www.asc-csa.gc.ca/eng/satellites/radarsat/default.asp (visited on 11/24/2018).
Elizavetin, Igor (2018). *Radiometric artifacts on SAR images*. URL: http://www.racurs.ru/download/conf/Italy2010/Presentations/Elizavetin.pdf (visited on 12/12/2018).
ESA (2018). *Sentinel-1: Facts and Figures*. URL: https://www.esa.int/Our_Activities/Observing_the_Earth/Copernicus/Sentinel-1/Facts_and_figures (visited on 12/01/2018).
European Commission (2017). *Copernicus: Europe's eyes on Earth*. URL: http://copernicus.eu/sites/default/files/documents/Brochure/Copernicus_brochure_EN_web_Oct2017.pdf (visited on 08/11/2018).
Hall, G (2015). *Pearson's correlation coefficient*. URL: http://www.hep.ph.ic.ac.uk/~hallg/UG_2015/Pearsons.pdf (visited on 12/01/2018).

ITU (2018). *Radio Regulations*. URL: https://www.itu.int/en/publications/ITU-R/pages/publications.aspx?parent=R-REG-RR-2016&media=electronic (visited on 12/01/2018).

LAWIS Tirol (2016). *User–Manual SnoProfiler*. https://www.lawis.at/manuals/LAWIS_SnoProfiler_EN.pdf.

Lievens, Hans et al. (2011). "Effective roughness modelling as a tool for soil moisture retrieval from C-and L-band SAR". In: *Hydrology and Earth System Sciences* 15.1, pp. 151–162.

Moreira, Alberto et al. (2013). "A tutorial on synthetic aperture radar". In: *IEEE Geoscience and remote sensing magazine* 1.1, pp. 6–43.

Naeimi, Vahid, Klaus Scipal, et al. (2009). "An improved soil moisture retrieval algorithm for ERS and METOP scatterometer observations". In: *IEEE Transactions on Geoscience and Remote Sensing* 47.7, pp. 1999–2013.

Oh, Yisok, Kamal Sarabandi, and Fawwaz T Ulaby (1992). "An empirical model and an inversion technique for radar scattering from bare soil surfaces". In: *IEEE transactions on Geoscience and Remote Sensing* 30.2, pp. 370–381.

Shepard, Donald (1968). "A two-dimensional interpolation function for irregularly-spaced data". In: *Proceedings of the 1968 23rd ACM national conference*. ACM, pp. 517–524.

Wagner, Wolfgang, Guido Lemoine, et al. (1999). "A study of vegetation cover effects on ERS scatterometer data". In: *IEEE Transactions on Geoscience and Remote Sensing* 37.2, pp. 938–948.

Wagner, Wolfgang and Raphael Quast (2015). *Microwave Remote Sensing*.

Wikipedia (2018). *Tirol (Bundesland)*. URL: https://de.wikipedia.org/wiki/Tirol_(Bundesland) (visited on 08/20/2018).

Appendices

A DMRT Parameters

This section is devoted to the physical and mathematical formulation of radiative transfer parameters needed to describe the propagation of an electromagnetic wave within a dense medium, e.g. a snow pack. First, it is necessary to define the dielectric properties of the snow pack. The dielectric constant of dry snow ϵ_{ice}, wet snow $\epsilon_{\text{wet ice}}$ and water ϵ_{water} can be written as follows (cf. Picard, Brucker, et al., 2012; Tsang, Kong, et al., 2004):

$$\epsilon_{\text{ice}} = 3.1884 + 0.00091(T - 273) + i(\frac{\alpha}{\beta} + \beta\nu) \tag{A.1}$$

where

$$\alpha = (0.00504 + 0.0062\Upsilon)e^{-22.1\Upsilon}$$

$$\beta = \frac{0.0207}{T}\frac{e^{\frac{335}{T}}}{(e^{\frac{335}{T}} - 1)^2} + 1.16 \cdot 10^{-11}\nu^2 + e^{-9.963+0.0372(T-273.16)}$$

and

$$\Upsilon = \frac{300}{T} - 1$$

T has to be in °C. For wet snow, a simplified relation is described as a mixing of the dielectric constant of ice ϵ_{ice} and water ϵ_{water}:

$$\epsilon_{\text{wet ice}} = \frac{C_+ + 2C_-}{C_+ - C_-}\epsilon_{\text{water}} \tag{A.2}$$

where

$$C_+ = \epsilon_{\text{ice}} + \epsilon_{\text{water}}$$

$$C_- = (\epsilon_{\text{ice}} - \epsilon_{\text{water}})\chi$$

In this case, χ is the liquid water content. ϵ_{water} is given by:

$$\epsilon_{\text{water}} = \epsilon_2 + \frac{\epsilon_1 - \epsilon_2}{1 - i\frac{\nu}{\nu_2}} + \frac{\epsilon_0 - \epsilon_1}{1 - i\frac{\nu}{\nu_1}} \tag{A.3}$$

where

$$\epsilon_0 = 77.6 + 103.3\Upsilon$$

$$\epsilon_1 = 0.0671\epsilon_0$$

$$\epsilon_2 = 3.52 + 7.52\Upsilon$$

$$\nu_1 = 20.2 - 146.4\Upsilon - 316\Upsilon^2$$

$$\nu_2 = 39.8\nu_1$$

Next, the scattering properties of a medium are defined based on a mono-disperse QCA-CP approximation and are described via the effective dielectric constant E_{eff}, which adds the relative scattering contribution of the particles to the dielectric constant of the background ϵ_b. This additional term includes the snow fractional volume f_{vol}, the radius of the particles a_p and stickiness parameter ζ, thus correcting for additional scattering effects. To achieve this, the effective dielectric constant without scattering E_{eff0} must be known:

$$E_{\text{eff0}}^2 + E_{\text{eff0}}\left(\frac{\epsilon_s - \epsilon_b}{3}(1 - f_{\text{vol}}) - \epsilon_b\right) - \epsilon_b\frac{\epsilon_s - 1}{3}(1 - f_{\text{vol}}) = 0 \tag{A.4}$$

where ϵ_s is the dielectric constant of the particles. After solving this quadratic equation and taking the positive root of E_{eff0}, one can use it in the formulation below:

$$\begin{aligned} E_{\text{eff}} =& \epsilon_b + (E_{\text{eff0}} - \epsilon_b)\left(1 + i\frac{2}{9}(k_0 a_p)^3\sqrt{E_{\text{eff0}}}(\epsilon_s - \epsilon_b) + \right. \\ & \left. \frac{\epsilon_s - \epsilon_b}{3E_{\text{eff0}}}(1 - f_{\text{vol}})\frac{(1 - f_{\text{vol}})^4}{(1 + 2f_{\text{vol}} - tf_{\text{vol}}(1 - f_{\text{vol}}))^2}\right) \end{aligned} \tag{A.5}$$

where k_0 is the wavenumber at the given frequency f and t can be computed using f_{vol} and ζ:

$$\frac{f_{\text{vol}}}{12}t^2 - \left(\zeta + \frac{f_{\text{vol}}}{1 - f_{\text{vol}}}\right)t + \frac{1 + \frac{f_{\text{vol}}}{2}}{(1 - f_{\text{vol}})^2} \tag{A.6}$$

This time, the appropriate solution for t can be found by taking the conditions stated in Tsang, Kong, et al. (2004, p. 427) into account.

The extinction coefficient κ_e and the scattering coefficient κ_s can then be written as a composite of all previous parameters:

$$\kappa_e = 2k_0\text{imag}\left(\sqrt{E_{\text{eff}}}\right) \tag{A.7}$$

$$\kappa_s = \frac{4}{9}k_0^4 a_p^3 f_{\text{vol}}\left|\frac{\epsilon_s - \epsilon_b}{1 + \frac{\epsilon_s - \epsilon_b}{3E_{\text{eff}}}(1 - f_{\text{vol}})}\right|^2 \frac{(1 - f_{\text{vol}})^4}{(1 + 2f_{\text{vol}} - tf_{\text{vol}}(1 - f_{\text{vol}}))^2} \tag{A.8}$$

Finally, the the optical depth τ and the single-scattering albedo ω describe volume scattering in a compact way and are as follows:

$$\omega = \frac{\kappa_s}{\kappa_e} \tag{A.9}$$

$$\tau = \kappa_e d \tag{A.10}$$

with d being the height of the snow layer.

B PLPS Examples

Two additional examples visualising σ^{40}_{PLPS} and σ^0 are given in Figure B.1 and B.2. Fig. B.1 shows backscatter from a glacier clearly reflecting the influence of wet snow as it was stated in Appendix D, i.e. a larger difference at smaller incidence angles and vice versa. Consequently, the distribution of σ^0 for each orbit is spread into two very distinct parts for this pixel, because a glacier is covered by snow nearly the whole year. This makes it even more important to consider the full arrangement of backscatter discretised by percentiles. An unsuitable example of a backscatter distribution can be found in Figure B.2. Both available orbits are close together, which prohibits a reliable estimation of the slope, no matter whether the linear regression or the PLPS method is chosen. Thus, normalisation becomes problematic the further both orbits are separated from the reference angle.

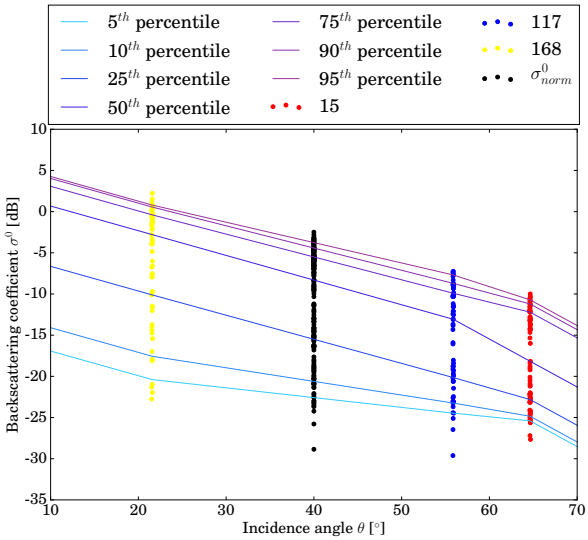

Figure B.1: Distribution of σ^0 and σ^0_{norm} for a pixel located at a glacier (*"Rettenbachferner"*). Strong snowmelt is clearly visible as low backscatter values, i.e. the 5th and 10th percentile.

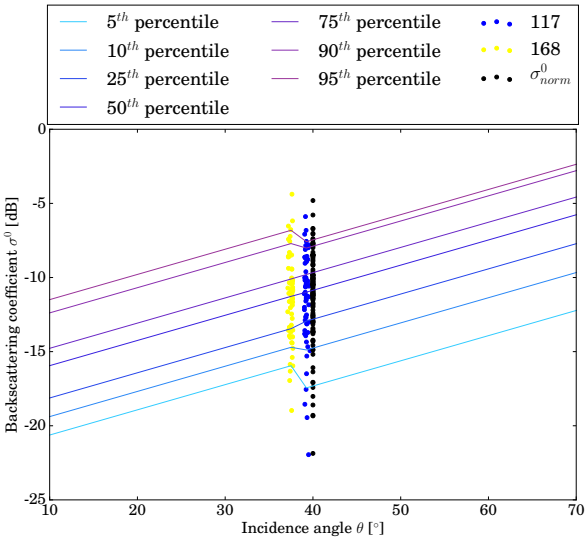

Figure B.2: Unfavourable conditions for normalising backscatter at a pixel located in the *"Inntal"* valley: only two orbits are available and they are very close to each other.

C Temperature Interpolation

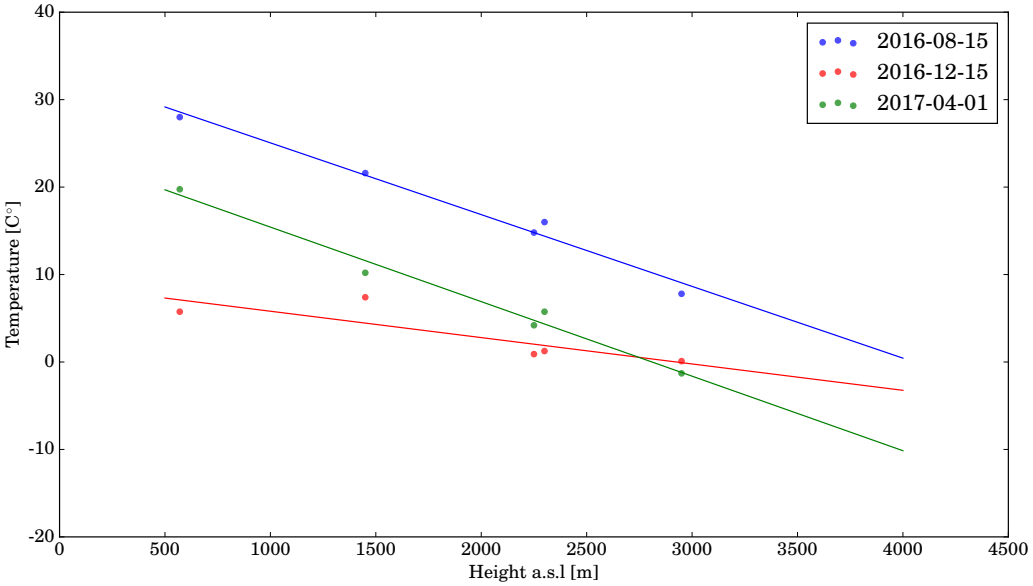

Figure C.1: Relation between the height a.s.l. of the stations and their measured temperature values on December 15$^{\text{th}}$, 2016 (red), April 1$^{\text{st}}$, 2017 (green) and August 15$^{\text{th}}$, 2016 (blue).

D C-Band SAR Backscatter Sensitivity to Wet Snow

Wet snow was completely neglected in the sensitivity analysis (Ch. 4), since it can be hardly described with common radiative transfer models. Yet, one can use the defined land cover points of rocky areas (cf. 4.1) to compare measurement from two different scenes, one observed during mid-winter and one during the snowmelt season. Figure D.1 includes a comparison of σ^0 and γ^0_{rtf} for both dates (June 6^{th}, 2017 and May 24^{th}, 2017) and with VV (a) and VH (b) polarisation, respectively. To overcome the noisy behaviour of the data and a misrepresentation of the chosen points, a simple cosine model was fit to the data assisting a visual interpretation.

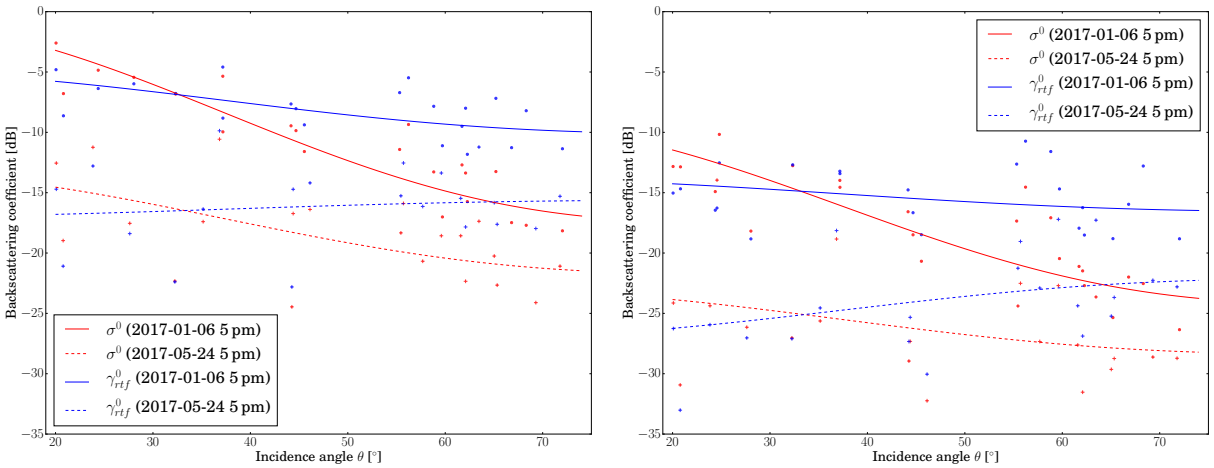

(a) VV polarisation

(b) VH polarisation

Figure D.1: Comparison of σ^0 and γ^0_{rtf} backscatter curves fitted to backscatter measurements at selected locations belonging to rocky areas. In each plot, measurements from two different dates, June 6^{th}, 2017 and May 24^{th}, 2017, are set into relation.

It can be seen that γ^0_{rtf} is less dependent on θ than σ^0, which underlines the purpose of radiometric terrain flattening, namely to correct for the impact of terrain on backscatter. The lower backscatter level due to wet snow is evident for the observations in May and the gap between dry snow and wet snow backscatter is smaller at higher incidence angles as volume scattering becomes more important. It is not possible to give preference to a certain backscatter representation for change detection, both are still dependent on θ when computing a difference between the backscatter curves in May and January. The γ^0_{rtf} curves in May, where backscatter is lower at small incidence angles, shows an unusual behaviour. This could either originate from the class-representative point selection meaning that some points are snow-free and others not, or because of the terrain flattening method itself. The former argument is also justified by the larger deviation of measured backscatter with respect to the fitted backscatter curves in May. Comparing

Figure D.1 (a) and (b) shows that all curves are shifted by around -10 dB, whereas VH polarised backscatter experiences a stronger shift. VH backscatter in May is close to or even beneath the noise floor of Sentinel-1 (-24 dB to -30 dB). This is also emphasised in Nagler, Rott, et al. (2016).